

# Characterization of Nonclassical Properties of Quantum States Generated in an Optical Parametric Amplifier

Dissertation  
zur Erlangung des akademischen Grades  
*doctor rerum naturalium (Dr. rer. nat.)*  
der Mathematisch-Naturwissenschaftlichen Fakultät  
der Universität Rostock

vorgelegt von: Melanie Schünemann, geb. Mraz am 03. April 1988 in Parchim  
Betreuer: Prof. Dr. Boris Hage

Rostock den 23. August 2017

Gutachter: Prof. Dr. Boris Hage

Universität Rostock  
Institut für Physik  
Arbeitsgruppe Experimentelle Quantenoptik  
Albert-Einstein-Str. 23-24  
18059 Rostock  
Deutschland

Prof. Dr. Ping Koy Lam

Australian National University  
Department of Quantum Science  
Quantum Optics Group  
Science Road Building 38a  
Canberra ACT 0200  
Australia

Tag der Verteidigung: 28. März 2018

# Selbständigkeitserklärung

Ich versichere hiermit an Eides statt, dass ich die vorliegende Arbeit selbständig angefertigt und ohne fremde Hilfe verfasst habe, keine außer den von mir angegebenen Hilfsmitteln und Quellen dazu verwendet habe und die den benutzten Werken inhaltlich und wörtlich entnommenen Stellen als solche kenntlich gemacht habe.

Rostock, 23. August 2017



## Acknowledgements

First of all, I am deeply grateful to Jun.-Prof. Dr. Boris Hage for giving me the opportunity to be the first PhD student in his group. Thank you for taking a so far completely theoretical physicist into your group and teaching me so much about experiments in quantum optics and thank you for teaching me to do things right.

Many experimentalists are sometimes lost without a good theoretician at their side and vice versa. I want to thank Prof. Dr. Werner Vogel for taking me into his group for my Bachelor and Master projects and the close cooperation during my PhD project.

Furthermore, I want to thank Prof. Dr. Ping Koy Lam to let me be a tiny part of a huge project. During my three month in your group in Canberra I have learned a lot about technical issues arising in a quantum optics lab. The experiences in your lab enhanced my projects in Rostock quite a lot.

I want to thank Jiri Janousek for teaching me a lot experimental tricks, Alexandre Bierussel to be my office and lab buddy and Giovanni Guccione for giving us a room in your house and all the pleasant lunch breaks and Kniffel matches.

In our group in Rostock, there were just the three of us: Semjon Köhnke, Oskar Schlettwein and myself. It was not always easy to share a lab, the soldering room or the office, but in the end we had a lot of fun and learned a lot from each other and no one plans better barbecues than we do! Thank you for these great years!

Thanks to the workshop guys in Rostock. You always made the impossible happen and without you our experiments wouldn't be possible.

During the past almost five years, I had the great opportunity to supervise various Bachelor and Master projects. Thanks to Wolfram Stamm, Hannes Sobottka, Dieter Schick, Christian Reiher, Steve Jäger and Milan Gödecke. Even though I supervised your projects, I have learned a lot from you! It was my pleasure to work with you.

I want to thank Karsten Sperlich, Elizabeth Agudelo Ospina, Martin Bohmann, Stefan Gerke and Benjamin Kühn for sharing the office with me for over three years and sharing hundreds of coffees and their knowledge with me. Special thanks to Karsten for giving me an easier start in experiments and Stefan and Benjamin for never tiring to answer my

stupid questions and reading this whole thesis for typos and displaced commas.

Furthermore, I want to thank Dr. Jan Sperling for teaching me everything I know about theoretical quantum optics. Thank you for your patience and that you never stopped being my mentor, even during my PhD project.

In the past years of studying physics, first Bachelor and Master and then PhD, I was supported by many people who did not share the same passion for quantum optics. I want to thank the people who started as my fellow students and then became friends. Thanks to Neeke Rothe, Karl Westphal and Heiner Asmus for the first three tough years. Thanks to Stephan Graunke, Maria Dietl, Rico Schnierer, Jens Söder, Chris Lappe, Tobias Zentel, Per-Arno Plötz and Florian Schöne for your friendship and support and the pleasant mensa times. Thanks to the rest of my friends for helping me, clear my mind of difficulties and giving me new energy to follow my ambitions.

I want to thank my family for their love and support. Thank you for your interest in my work and many pleasant times beside of it.

Finally, I want to thank my amazing husband. You listen to all my achievements and troubles, even so half of the time you do not know what I am actually talking about. Thank you for understanding my Matlab problems and sometimes solving them. Thank you for traveling with me to Australia and leaving everything behind for that time. Thank you for always being there and being the love of my life.

## Abstract

The nonclassical properties of quantum states raise a lot of attention, due to their various possible applications in future quantum technologies. A state is nonclassical, if its Glauber-Sudarshan  $P$ -function shows negativities and therefore cannot be interpreted as a classical probability density. This thesis concerns the generation of quantum states and the characterization of their nonclassical properties. Therefore, an experimental technique to generate quantum states, to be specific squeezed vacuum and coherently displaced squeezed states, is presented. In order to characterize nonclassical states, a new experimental technique, the homodyne cross correlation measurement, was realized, showing a so far unknown insight into the quantumness of a squeezed state. Also, an experimentally accessible witnessing approach for the degree of nonclassicality, in terms of superpositions of coherent states, is presented for arbitrary quantum states.

## Zusammenfassung

Die nichtklassischen Eigenschaften von Quantenzuständen erregen viel Aufmerksamkeit, durch ihre zahlreichen möglichen Anwendungen in zukünftigen Quantentechnologien. Ein Zustand ist nichtklassisch, wenn die zugehörige Glauber-Sudarshan  $P$ -Funktion Negativitäten aufzeigt und somit nicht mehr als klassische Wahrscheinlichkeitsdichte interpretiert werden kann. Diese Arbeit beschäftigt sich mit der Erzeugung von Quantenzuständen und der Charakterisierung ihrer nichtklassischen Eigenschaften. In diesem Rahmen wird eine experimentelle Technik zur Erzeugung von Quantenzuständen, genauer gesagt gequetschten Vakuumzuständen und kohärent verschobenen gequetschten Zuständen, vorgestellt. Für die Charakterisierung von nichtklassischen Zuständen wurde eine neue experimentelle Technik, die homodyne Kreuzkorrelationsmessung, wurde realisiert. Sie gibt einen bisher unbekannten Einblick in die Quantennatur von gequetschten Zuständen. Außerdem wird ein experimentell zugänglicher Nachweis für den Nichtklassizitätsgrad, im Sinne von Überlagerungen von kohärenten Zuständen, für beliebige Quantenzustände präsentiert.



# Contents

<b>1. Introduction</b>	<b>1</b>
<b>2. Theoretical Methods</b>	<b>3</b>
2.1. Quadrature amplitudes and Heisenberg uncertainty principle . . . . .	3
2.2. Quantum States . . . . .	4
2.2.1. Number or Fock States . . . . .	5
2.2.2. Coherent States . . . . .	5
2.2.3. Quadrature Squeezed State . . . . .	7
2.3. Phase space functions . . . . .	9
2.3.1. Husimi $Q$ -function . . . . .	10
2.3.2. Wigner function . . . . .	11
2.3.3. Glauber-Sudarshan $P$ -function . . . . .	11
2.3.4. Nonclassicality and phase space functions . . . . .	12
2.3.5. Regularized Glauber-Sudarshan $P$ -function . . . . .	13
2.4. Optical Parametric Amplifier (OPA) . . . . .	15
<b>3. Experimental tools and techniques</b>	<b>23</b>
3.1. Laser System . . . . .	24
3.2. Mode Cleaner Cavity (MC) . . . . .	24
3.3. Electro-Optic Modulator (EOM) . . . . .	27
3.4. Pound-Drever-Hall (PDH) Technique . . . . .	29
3.5. Optical Parametric Amplifier (OPA) . . . . .	32
3.6. Photo Diodes . . . . .	34
3.7. Balanced Homodyne Detection (BHD) and Quantum State Tomography . .	36
3.8. Continuous Sampling . . . . .	38
<b>4. Anomalous quantum correlations of squeezed light</b>	<b>41</b>
4.1. Theoretical description . . . . .	42
4.2. Experimental setup . . . . .	45

4.3. Results . . . . .	47
4.4. Summary and conclusions . . . . .	52
<b>5. Witnessing the degree of nonclassicality</b>	<b>53</b>
5.1. Introduction . . . . .	53
5.1.1. General definition . . . . .	54
5.1.2. Witnessing approach . . . . .	55
5.1.3. Optimization . . . . .	57
5.2. Previous results . . . . .	59
5.2.1. General numerical implementation . . . . .	60
5.2.2. Optimal witness for pure states . . . . .	62
5.2.3. Infinite superposition states . . . . .	63
5.3. Multimode Nonclassicality . . . . .	65
5.4. Witnessing using pattern functions . . . . .	66
5.4.1. Pattern functions in coherent state basis . . . . .	67
5.4.2. Application to simulated data . . . . .	69
5.4.3. $\rho_{\alpha'\alpha}$ in the witnessing approach . . . . .	72
5.5. Summary and outlook . . . . .	84
<b>6. Further work</b>	<b>85</b>
6.1. Building a Mode Cleaner . . . . .	85
6.2. Unified Nonclassicality Criteria . . . . .	87
<b>7. Summary and Outlook</b>	<b>93</b>
<b>A. Relation between transmitted power and measured voltage</b>	<b>95</b>
<b>B. Characteristics of the PDs</b>	<b>97</b>
<b>C. More possible visualizations of the density matrices <math>\rho_{\alpha,\alpha'}</math></b>	<b>99</b>
<b>D. General simulation approach</b>	<b>101</b>
D.1. Simulation of the quantum state . . . . .	101
D.2. Generation of test states . . . . .	102
<b>Bibliography</b>	<b>107</b>
<b>List of Publications</b>	<b>121</b>





# Chapter 1.

## Introduction

*"In fact, the mere act of opening the box will determine the state of the cat, although in this case there were three determinate states the cat could be in: these being Alive, Dead, and Bloody Furious."*

— Terry Pratchett, *Lords and Ladies*

The discussion about quantum physics already started at the beginning of the 20th century. The physicists of that time, tired to comprehend the nonclassical properties arising due to quantum superpositions. When Erwin Schrödinger used his famous gedankenexperiment about a cat that is dead and alive at the same time, see [Sch35], he was aiming to give a simple example, that proves how absurd the existing view of quantum physics is. He was, however, not alone with this opinion. Other famous physicists of that time, like Einstein, Podolsky and Rosen, see [EPR35] also presented gedankenexperiments, paradoxes or discussions, why the nonclassical and nonintuitive properties in quantum physics arises due to the fact that quantum physics is not a complete theory in the sense of local realism. Almost three decades later, John Bell presented his famous inequality, see [Bel64], which only holds for local and real theories. Quantum physical expectation values directly violate this inequality and therefore this inequality provides a direct prove, that quantum physics cannot be completed by the use of local hidden variables, as proposed by Einstein, Podolsky and Rosen, to fulfill the criteria of local realism. Nowadays, Schrödingers gedankenexperiment is known far beyond the physics community, like in literature, e.g. the above citation of Terry Pratchett in *Lords and Ladies*, that distribute this gedankenexperiment and its consequences into the world.

Using quantum physics we can perform various experiments, showing nonclassical behavior as predicted by the gedankenexperiments in the 1930s, and even violate Bells inequality experimentally [FC72, ADR82, HBD15, GVW15]. Of course, it would be inappropriate to show these effects using cats. Instead single atoms, ions and photons are a suitable test bed for these nonclassical effects, introducing the field of quantum optics, see e.g. [SHY85, RD88, Rei89, Win98, BHD96, VF95, CR00, FT02, KM76, KDM77, SHY85, Wer89, HHH96, Per96]. In the field of quantum optics, we can perform experiments that show different nonclassical effects like squeezing (see e.g. [SHY85, VMDS16]) and entanglement (see e.g. [RD88, Rei89, Bow98, AMJ12]) and even apply them to different applications of these effects in gravitational wave detection, see [GDD13], quantum teleportation, see e.g. [BPM97], and quantum key distribution, see e.g. [BBB92, PZY07]. However, in this thesis we consider the nonclassical aspects of light, i.e. the generation and characterization of nonclassical light, to be more specific we are concerning squeezed light. Hence, we will restrict the consideration to this, and not go into detail with entanglement or concern atoms and ions.

Within the framework of the thesis a new laboratory was started from scratch, as only the optical table and the laser existed in the beginning. We set up two optical parametric amplifiers as sources for squeezed light and characterized these generated states with well known, balanced homodyne detection, and new experimental detection schemes, always in close cooperation with the *Theoretical Quantum Optics Group* of Prof. Dr. Werner Vogel. The achieved theoretical and experimental results are summarized in this thesis.

In this thesis, we first introduce in Chap. 2 the theoretical methods, which are necessary to understand the results of this thesis. Then, we introduce the experimental techniques that were constructed and used throughout the experiments performed for this thesis in Chap. 3. Afterwards, we present the two main results of the thesis, concerning the anomalous quantum correlations of squeezed light [3], see Chap. 4, and the quantification of nonclassicality [4], see Chap. 5. As not all the work, that is done during a PhD time can be discussed in detail in such a thesis, we will also address shortly some of these further projects in Chap. 6.

## Chapter 2.

### Theoretical Methods

This chapter gives an overview of the theoretical basics used throughout this thesis. The following explanations are taken from [BR08, VW06, WM08, DFE04, Sch01, Boy08, Leo97, Whi97, Lam98, Jan07] if not denoted otherwise.

#### 2.1. Quadrature amplitudes and Heisenberg uncertainty principle

One can find a solution to the vacuum Maxwell equations as the free propagating electromagnetic field in dependence of position  $\mathbf{r}$  and time  $t$  to

$$\mathbf{E}(\mathbf{r}, t) = i \sum_k \left( \frac{\hbar \omega_k}{2\epsilon_0} \right)^{1/2} \left[ a_k \mathbf{u}_k(\mathbf{r}) e^{-i\omega_k t} - a_k^* \bar{\mathbf{u}}_k(\mathbf{r}) e^{i\omega_k t} \right], \quad (2.1)$$

where  $\mathbf{E}$ ,  $\mathbf{u}_k(\mathbf{r})$  and  $\mathbf{r}$  are vectors. Here  $\mathbf{u}_k(\mathbf{r})$  are mode functions containing information of the spatial phase and polarization. The values  $a_k$  and  $a_k^*$  are the complex Fourier amplitudes which are, dimensionless and complex numbers in the classical electromagnetic field theory. Since we are working in the quantum domain of light, we have to quantize the electromagnetic field in order to study the quantum behavior. This is achieved by replacing the complex numbers  $a_k$  and  $a_k^*$  by the mutually adjoint operators  $\hat{a}_k$  and  $\hat{a}_k^\dagger$ , being the bosonic annihilation and creation operator. They fulfill the bosonic commutation relations

$$[\hat{a}_k, \hat{a}_{k'}] = [\hat{a}_k^\dagger, \hat{a}_{k'}^\dagger] = 0 \quad \text{and} \quad [\hat{a}_k, \hat{a}_{k'}^\dagger] = \delta_{k,k'}. \quad (2.2)$$

In order to keep our notation clear and not overwhelmed by indexes, we consider only a single field mode in the following. Hence, we drop the frequency dependent index  $k$ .

However, as the annihilation and creation operators are not Hermitian, they correspond to no measurable physical quantity. However the orthogonal quadratures, which are defined as

$$\hat{X}^+ = \hat{a} + \hat{a}^\dagger \quad (2.3)$$

$$\hat{X}^- = -i(\hat{a} - \hat{a}^\dagger), \quad (2.4)$$

where  $\hat{X}^+$  is the amplitude quadrature and  $\hat{X}^-$  is the phase quadrature. They fulfill the commutation relation

$$[\hat{X}^+, \hat{X}^-] = 2i. \quad (2.5)$$

The product of the variances of these operators,  $\langle(\Delta\hat{X}^+)^2\rangle \cdot \langle(\Delta\hat{X}^-)^2\rangle$ , for an arbitrary quantum state is bounded by one, i.e.

$$\langle(\Delta\hat{X}^+)^2\rangle \cdot \langle(\Delta\hat{X}^-)^2\rangle \geq 1, \quad (2.6)$$

according to the Heisenberg uncertainty principle. In the case of  $\langle(\Delta\hat{X}^+)^2\rangle \cdot \langle(\Delta\hat{X}^-)^2\rangle = 1$  the state is a minimum uncertainty state. The two quadratures  $\hat{X}^+$  and  $\hat{X}^-$  span a complex space, the phase space. In classical physics, each point in the phase space is associated with a probability to find the field in a specific electromagnetic field amplitude. In quantum physics, however, Heisenberg's uncertainty principle prevents us from such an interpretation. Nevertheless, in quantum physics, phase space functions are a possible state representation that is useful for the description of electromagnetic fields. These phase space functions, see Sec. 2.3.4, can be visualize in a phase space diagram, which is a graphical representation of the state in phase space.

## 2.2. Quantum States

The following section gives an overview over the quantum states that are of major importance throughout this thesis.

### 2.2.1. Number or Fock States

Number or Fock states are well known as the energy eigenstates of the harmonic oscillator. However, these states do not show an oscillatory behavior which is classically expected. This oscillatory behavior is realized by the coherent states, see Sec. 2.2.2.

The Fock states are the eigenstates to the number operator  $\hat{n} = \hat{a}^\dagger \hat{a}$

$$\hat{n} |n\rangle = n |n\rangle \quad (2.7)$$

with  $n = 0, 1, \dots$ , and are an orthonormal set of basis states  $\langle n|m\rangle = \delta_{n,m}$ . The Fock state to the minimal eigenvalue  $n = 0$  is the vacuum state  $|0\rangle$  which is the quantum mechanical ground state and hence has the lowest possible energy  $1/2 \hbar\omega$ . This state has a quadrature expectation value of zero, but nonzero quadrature variance,  $\langle(\Delta\hat{X}^+)^2\rangle$  and  $\langle(\Delta\hat{X}^-)^2\rangle$ , given by the Heisenberg uncertainty principle.

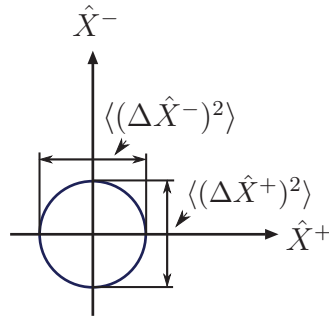


Figure 2.1.: Representation of the vacuum state in phase space.

In Fig. 2.1 a typical representation of a quantum state, in this special case the vacuum state, in a phase space diagram is shown. Here we usually display only a circle in phase space, being a contour line of an arbitrary probability distribution, see Sec. 2.3.4, where the product of the variances  $\langle(\Delta\hat{X}^+)^2\rangle \cdot \langle(\Delta\hat{X}^-)^2\rangle$  is one.

### 2.2.2. Coherent States

The coherent state is generated by displacing the vacuum state, cf. Fig. 2.2

$$\hat{D}(\alpha) |0\rangle = |\alpha\rangle, \quad (2.8)$$

for  $\alpha \in \mathbb{C}$ , with the displacement operator

$$\hat{D}(\alpha) = e^{\alpha \hat{a}^\dagger} e^{-\alpha^* \hat{a}} e^{-|\alpha|^2/2}. \quad (2.9)$$

Hence the coherent state

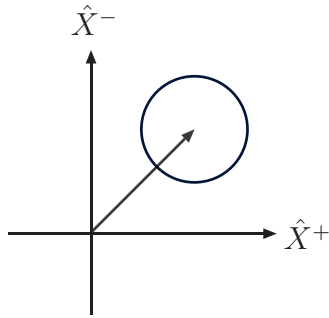


Figure 2.2.: Representation of the coherent state in phase space.

$$|\alpha\rangle = e^{-|\alpha|^2/2} \sum_{n=0}^{\infty} \frac{\alpha^n}{\sqrt{n!}} |n\rangle, \quad (2.10)$$

$$\text{with } \langle\alpha|\alpha\rangle = 1 \text{ and } \langle\alpha'|\alpha\rangle = e^{-|\alpha|^2/2 - |\alpha'|^2/2 + \alpha'^* \alpha}$$

is also a minimum uncertainty state and is defined as an infinite number of superpositions of Fock states where  $\alpha$  is the complex coherent amplitude [Gla63]. Furthermore, this state is the quantum state of the quantum harmonic oscillator. As this state resembles the behavior of the classical harmonic oscillator most closely, it can provide a border between quantum and classical states [Gla63]. The coherent state is the eigenstate to the annihilation operator  $\hat{a}$

$$\hat{a} |\alpha\rangle = \alpha |\alpha\rangle. \quad (2.11)$$

As the photon number operator  $\hat{n}$  is given by  $\hat{a}^\dagger \hat{a}$  and  $\hat{a}$ , the mean photon number is given by  $|\alpha|^2$ . These states are a powerful tool in quantum physics, as they can be used in the description of laser beams. In the limit of a strong laser beam, the coherent amplitude  $\alpha$  is large, so is the photon number, hence the laser beam can be treated classically as the uncertainty in comparison to the coherent amplitude is small.

However, one can also find quantum states defined as superpositions of coherent states like the even ( $|\alpha_+\rangle$ ) and odd ( $|\alpha_-\rangle$ ) coherent states [DMN95], which are superpositions

of two coherent states

$$|\alpha_+\rangle = N_+ (|\alpha\rangle + |-\alpha\rangle) = N_+ \sum_{n=0}^{\infty} \frac{\alpha^{2n}}{\sqrt{(2n)!}} |2n\rangle \quad (2.12)$$

$$|\alpha_-\rangle = N_- (|\alpha\rangle - |-\alpha\rangle) = N_- \sum_{n=0}^{\infty} \frac{\alpha^{2n+1}}{\sqrt{(2n+1)!}} |2n+1\rangle, \quad (2.13)$$

with the normalization factors

$$N_+ = \frac{e^{|\alpha|^2/2}}{2\sqrt{\cosh(|\alpha|^2)}} \quad (2.14)$$

and

$$N_- = \frac{e^{|\alpha|^2/2}}{2\sqrt{\sinh(|\alpha|^2)}} \quad (2.15)$$

and the compass state [AP04]

$$|\alpha_R\rangle = N_R \sum_{k=0}^{R-1} |\alpha e^{2\pi i k/R}\rangle, \quad (2.16)$$

where  $R \in \mathbb{N}$  denotes the number of superpositions of coherent states, and  $N_R$  provides the correct normalization.

### 2.2.3. Quadrature Squeezed State

A quadrature squeezed state is generated from a vacuum or a coherent state by applying the unitary squeezing operator

$$\hat{S}(\xi) = \exp \left[ \frac{1}{2} (\xi^* \hat{a}^2 - \xi \hat{a}^{\dagger 2}) \right], \quad (2.17)$$

where  $\xi = r e^{i\phi_\xi}$  is the complex squeezing parameter with the real valued squeezing strength  $r$  and the squeezing direction in phase space  $\phi_\xi$ . If applied to the vacuum state this results in

$$\hat{S}(\xi) |0\rangle = |\xi, 0\rangle = \frac{1}{\sqrt{\mu}} \exp\left(-\frac{\nu}{2\mu} \hat{a}^{\dagger 2}\right) |0\rangle \quad (2.18)$$

which is the squeezed vacuum state with  $\mu = \cosh(|\xi|)$  and  $\nu = e^{i\phi_\xi} \sinh(|\xi|)$ , cf. Fig. 2.3. Note that the notation  $|\xi, 0\rangle$  here, does not refer to two modes, it just emphasizes that we squeezed a vacuum state. If applied to the coherent state we end up with

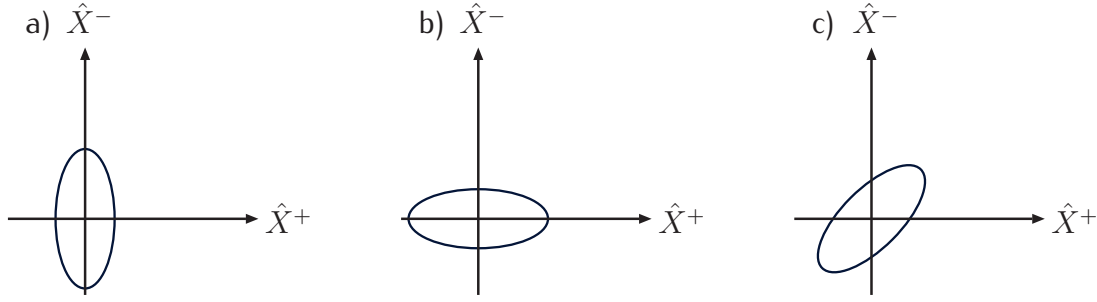


**Figure 2.3.:** Representation of the squeezed vacuum state in phase space. Here a) is an amplitude squeezed vacuum state, b) is a phase squeezed vacuum state and c) is a squeezed vacuum state at  $\phi_\xi = 45^\circ$ .

$$|\xi, \alpha\rangle = \hat{S}(\xi)\hat{D}(\alpha)|0\rangle = \frac{1}{\sqrt{\mu}} \exp\left(-\frac{\nu}{2\mu}(\hat{a}^\dagger - \alpha'^*)^2\right) |\alpha'\rangle \quad (2.19)$$

which is the coherently displaced squeezed state and  $\alpha' = \mu\alpha - \nu\alpha^*$ , cf. Fig. 2.4. This can be understood as first displacing the vacuum state and then squeezing the resulting coherent state. However, we arrive at the same result by first squeezing the vacuum and then displacing it

$$|\xi, \alpha\rangle = \hat{D}'(\alpha)\hat{S}(\xi)|0\rangle = \frac{1}{\sqrt{\mu}} \exp\left(-\frac{\nu}{2\mu}(\hat{a}^\dagger - \alpha'^*)^2\right) |\alpha'\rangle, \quad (2.20)$$

where  $\hat{D}'(\alpha) = \hat{S}(\xi)\hat{D}(\alpha)\hat{S}^\dagger(\xi)$  is the transformed displacement operator.

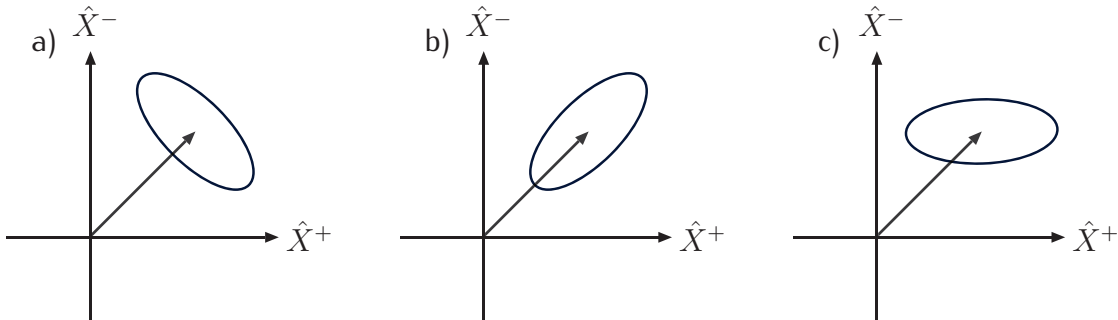


**Figure 2.4.:** Representation of the coherently displaced squeezed state in phase space. Here a) is a coherently displaced amplitude squeezed state, b) is a coherently displaced phase squeezed state and c) is a coherently displaced squeezed state at  $\phi_\xi = 45^\circ$ .

Squeezed states are minimum uncertainty states, but unlike in the case of the vacuum state or the coherent state their distribution in phase space is not symmetric, i.e., is no longer a circle but rather an ellipse. This means, the variance in one quadrature is reduced below the vacuum level and simultaneously enhanced in the other, resulting in an ellipse. The exact orientation of this ellipse in phase space is, for the mere definition of squeezing, arbitrary. However, even though the distribution in phase space is no longer a circle, the product of the variances is still limited by the Heisenberg uncertainty principle.

The reduction of the variance below the vacuum level in one quadrature opens up a wide range of applications. For example, in the GEO600 experiment in Hannover [GDD13] squeezed states were implemented in the interferometer to enhance the sensitivity of the gravitational wave detector. The success here inspired the LIGO experiments to follow the example of GEO600 and implement squeezed states in their interferometers [At13]. Furthermore squeezed states are also used in biological measurements [TJD13], spectroscopy [PCK92] and just recently the development of protocols for quantum information protocols picked up pace [BL05, FSB98, MFP08].

## 2.3. Phase space functions

Phase space functions are a handy tool in order to fully characterize quantum states. In order to introduce phase space functions, let's start with an arbitrary Hermitian operator  $\hat{O} = \hat{f}(\hat{a}, \hat{a}^\dagger)$ , which we want to characterize using phase space functions. The measurable physical observable of this operator  $\hat{O}$  is its eigenvalue  $O$ . However, in measurements we are faced with uncertainties and hence we perform multiple measurements and end up with a statistical average called the expectation value of  $\hat{O}$ . This expectation value can be written as

$$\langle \hat{O} \rangle = \langle \hat{f}(\hat{a}, \hat{a}^\dagger) \rangle = \int d^2\alpha P(\alpha; s) f(\alpha; s) \quad (2.21)$$

where

$$P(\alpha; s) = \langle \hat{\delta}(\hat{a} - \alpha; s) \rangle \quad (2.22)$$

is the parameterized phase space function and  $f(\alpha; s)$  is a complex function depending on the operator ordering. The  $s$ -parameterized  $\delta$ -function is given as

$$\hat{\delta}(\hat{a} - \alpha; s) = \frac{2}{\pi(1-s)} : \exp \left[ \frac{-2\hat{n}(\alpha)}{1-s} \right] :, \quad (2.23)$$

where the displaced number operator

$$\hat{n}(\alpha) = \hat{D}(\alpha) \hat{n} \hat{D}^\dagger(\alpha) \quad (2.24)$$

contains the already introduced displacement operator  $\hat{D}(\alpha)$  (2.9).

Encoded in the  $s$ -parameter is the operator ordering that decides which specific phase space function we are looking at. For  $s=-1, 0, 1$  the operator ordering is anti-normal, all creation operators are right to the annihilation operators, symmetric and normal, all creation operators are left to the annihilation operators, respectively. Following from these different operator orderings are three different phase space functions: the Husimi  $Q$ -function (for anti-normal ordering), the Wigner function (for symmetric ordering), and the Glauber-Sudarshan  $P$ -function (for normal ordering).

### 2.3.1. Husimi $Q$ -function

The Husimi  $Q$ -function, or short  $Q$ -function, is the result of the  $s$ -parameterized phase space function (2.22) for  $s=-1$ , which means that the  $\hat{\delta}$  operator is in anti-normal order. This results in the very general form of the  $Q$ -function

$$Q(\alpha) = \langle \ddagger \hat{\delta}(\alpha - \hat{a}) \ddagger \rangle \quad (2.25)$$

$$= \frac{1}{\pi} \langle \alpha | \hat{\rho} | \alpha \rangle \quad (2.26)$$

where  $\hat{\rho} = \sum_{\psi} P_{\psi} |\psi\rangle \langle \psi|$  is the density operator of an arbitrary quantum state  $|\psi\rangle$  with the weights  $P_{\psi}$ , which can be interpreted as the probability of finding the quantum state in  $|\psi\rangle$  and  $\langle \ddagger \ddagger \rangle$  denoting the anti-normal ordering. As  $P_{\psi}$  resembles a probability density it holds

$$P_{\psi} \geq 0 \quad \text{and} \quad \sum_{\psi} P_{\psi} = 1. \quad (2.27)$$

For a pure state,  $|\phi\rangle$  the density operator is given by  $\hat{\rho} = |\phi\rangle\langle\phi|$ . The  $Q$ -function is always positive and bound between  $0 \leq Q(\alpha) \leq \frac{1}{\pi}$ . It can be interpreted as the quantum mechanical expectation value of the density operator  $\hat{\rho}$  in a coherent state. However, it cannot be interpreted, in the sense of classical theory, as a probability distribution of the complex amplitude  $\alpha$ , although it has all the properties of a probability distribution. Still it allows the calculation of a quantum mechanical expectation value in a very convenient way [HUS40, Kan65].

### 2.3.2. Wigner function

Another well established phase space function is the Wigner function, cf. [Wig32]. This function is the result of symmetrically ordered operators in the  $s$ -parameterized phase space function, i.e.  $s=0$ . It reads as

$$W(\alpha) = \langle \hat{\delta}(\alpha - \hat{a}) \rangle \quad (2.28)$$

$$= \frac{2}{\pi} \langle (-1)^{\hat{n}(\alpha)} \rangle \quad (2.29)$$

and is bound between  $-\frac{2}{\pi} \leq W(\alpha) \leq \frac{2}{\pi}$ . In contrast to the  $Q$ -function, the Wigner function may attain negative values.

### 2.3.3. Glauber-Sudarshan $P$ -function

This leaves us with the last phase space function, following the normal operator order, i.e.  $s=1$ , the so called Glauber-Sudarshan  $P$ -function, or short  $P$ -function. It is defined as

$$P(\alpha) = \langle : \hat{\delta}(\hat{a} - \alpha) : \rangle, \quad (2.30)$$

where  $\langle : \rangle$  denotes the normal ordering. This function, like the Wigner function, can attain negative values and is therefore no probability distribution. Furthermore, this function has an additional nasty feature as it is not necessarily a well behaved function. However, the  $P$ -function is, due to the normal ordering of the operators, of a special importance in photo detection. This is due to the fact, that the expectation values appearing in the photo detection contain normally ordered moments and correlations [Gla63, Sud63].

### 2.3.4. Nonclassicality and phase space functions

So far we were talking about quantum states, or nonclassical states, in general, but how can we distinguish between classical and nonclassical states? A state is nonclassical, if its  $P$ -function cannot be interpreted as a classical probability density. Hence, we cannot express the state as a classical mixture of coherent states [Gla63, Sud63]. Why we choose this phase space function, even though it is not necessarily a well behaved function?

Each of the three presented  $s$ -parameterized phase space functions has a specific benefit, but they also come at a specific cost, see Fig. 2.5. As mentioned above,

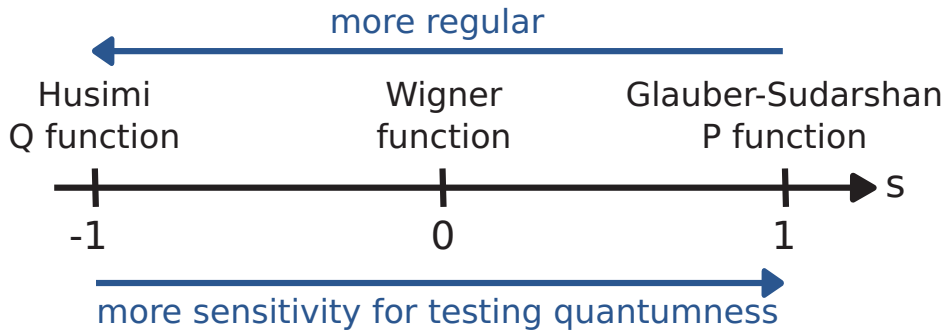


**Figure 2.5.:** Comparison of the three presented phase space functions in terms of the sensitivity for quantumness tests versus the regularity [AO16]. (Taken from private communication with Elizabeth Agudelo Ospina)

a highly singular function, as the  $P$ -function, cannot be addressed in an experiment. However, it is worth the effort as the  $P$ -function is the only phase space function that can prove the nonclassicality, in terms of superpositions of coherent states, of an investigated state for sure. In comparison, the  $Q$ -function is regular and therefore can be obtained straightforward from the experimental data. The drawback of the  $Q$ -function is however, just looking at this function gives us no information about the nonclassical behavior as it is per definition non-negative everywhere. The Wigner function is for some quantum states sensitive for nonclassicality, but not for every quantum state. Hence, if we find negativities in the Wigner function we know for sure that the state is nonclassical, but if the Wigner function is nonnegative, we cannot make any statement whether the state is nonclassical or not. However, the reconstruction of the Wigner function can be done in a very straightforward way via the inverse Radon-transformation of experimental data. Conclusively, only the  $P$ -function is capable of a secure test for nonclassicality and

with the regularization of the  $P$ -function, we can also cancel out the problems in the reconstruction.

### 2.3.5. Regularized Glauber-Sudarshan $P$ -function

The fact that the  $P$ -function is not always well behaved is a huge disadvantage, as, e.g., the squeezed states, which are of major importance in quantum optics, have a highly singular  $P$ -function, because it contains an infinite number of derivatives of the delta distribution. Hence, in general, it cannot be accessed in an experiment, i.e., sampled out of experimentally measured homodyne data, see. Sec. 3.7. There is however a very sensible way to circumvent this issue, by using the characteristic function  $\Phi(\beta)$ , being the Fourier transform of the  $P$ -function, of the quantum state and applying of a filter function  $\Omega_W(\beta)$  on  $\Phi(\beta)$ , which is introduced in [KV10, KVHS11]. This filter function smooth out this singular behavior into a measurable function, i.e., a function that can be sampled out of homodyne data. As this filtering removes this singular behavior, the resulting function is called the regularized Glauber-Sudarshan  $P$ -function, or short the regularized  $P$ -function. Here the filter function itself is not applied to the  $P$ -function, but rather to its Fourier transform, the characteristic function  $\Phi(\beta)$

$$\Phi(\beta) = \langle : \exp(\beta \hat{a}^\dagger - \beta^* \hat{a}) : \rangle. \quad (2.31)$$

The application of the filter results in the filtered characteristic function  $\Phi_\Omega(\beta)$

$$\Phi_\Omega(\beta) = \Phi(\beta) \Omega_W(\beta). \quad (2.32)$$

To fulfill the purpose of regularizing the  $P$ -function, the filter function must meet certain conditions in order to not change the physical properties of the investigated state, taken from [KVHS11].

1.  $\Omega_W(\beta)$  must be integrable for an arbitrary quantum state  $\Phi(\beta)$  resulting in a Fourier transform that is a regular function
2.  $\Phi_\Omega(\beta)$  has a non-negative Fourier transform to ensure that all negativities in the regularized  $P$ -function are due to the nonclassical features of the quantum state
3. For a filter width  $W \rightarrow \infty$  the filtered characteristic function should converge to the unfiltered characteristic function

4.  $\Omega_W(\beta) \neq 0 \forall \beta$  so that no information of the quantum state is lost

Note that requirement 4. is indeed not necessary for the filtering, and therefore not always used and what is more, that the filter function can also be applied to the  $P$ -function, c.f. [ASV13] and [1].

If these conditions are fulfilled we can sample the regularized  $P$ -function out of experimental measured homodyne data. In particular, the regularized  $P$ -function of an experimentally generated and measured squeezed state is shown in Fig. 2.6, see [1].

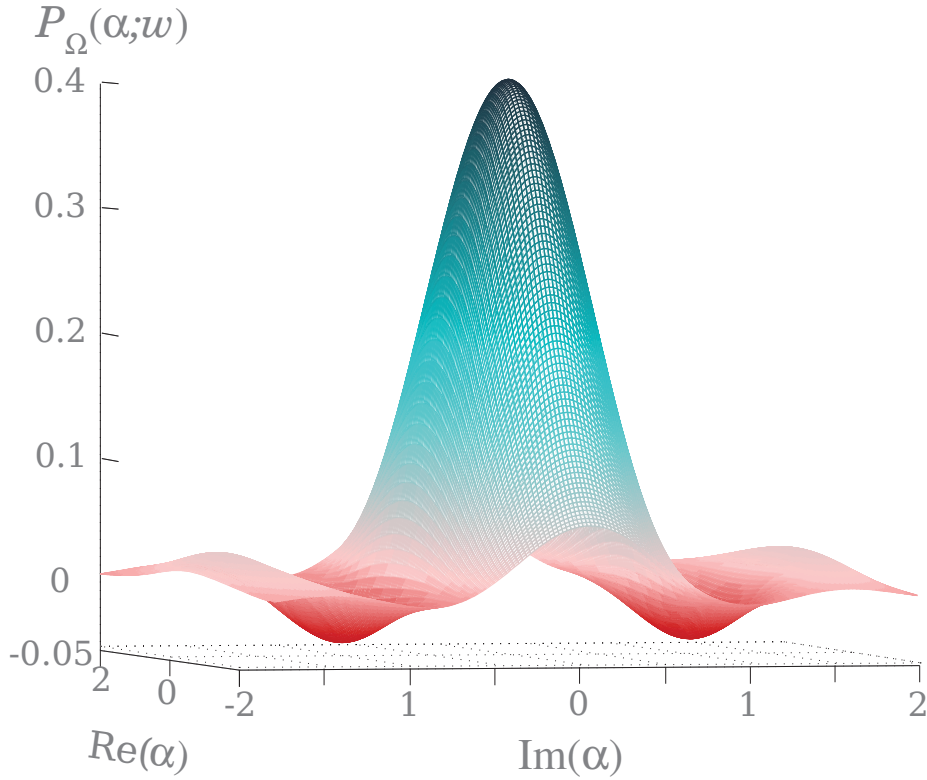


**Figure 2.6.:** Regularized  $P$ -function of an experimentally detected squeezed state, using the continuous sampling approach, see Sec. 3.8, displaying clear negativities.

Hence, by using the regularized  $P$ -function, we can distinguish between classical and nonclassical states using homodyne data. Note that, in Sec. 4 we will present an alternate approach to prove the nonclassicality of a state by introducing a new measurement scheme, the homodyne cross correlation measurement.

## 2.4. Optical Parametric Amplifier (OPA)

Throughout all experiments performed during this thesis, we were dealing with squeezed states, either with squeezed vacuum states or with coherently displaced squeezed states. To be more precise, we generate the squeezed states in an optical parametric amplifier (OPA). The description of an OPA is parted in two different sections. First a theoretical description is given in Sec. 2.4 and later the experimental realization is discussed in Sec. 3.5.

To produce a squeezed state of light it is necessary to attenuate one quadrature while at the same time amplifying the other. Hence a phase sensitive amplifier is needed as a phase insensitive amplifier would introduce excess noise which would prevent a noise reduction under the vacuum limit. An OPA is such a desired phase sensitive amplifier.

In general an OPA is set up out of a  $\chi^{(2)}$  nonlinear crystal inside a cavity, where the cavity is used to enhance the nonlinear effect due to multiple round trips of the light through the crystal.

As we are dealing with an optical cavity into which we couple a light field, we are dealing with an open system that interacts with the environment. Hence for a full description of the nonlinear effects inside the OPA we formulate in the following the input-output formalism using the quantum Langevin equation and the Heisenberg approach for our specific cavity.

### Theory of OPA

The here presented derivations follow the derivations in [Bow98, Whi97, Jan07].

In general any cavity can be modeled using the quantum Langevin equation. To derive this equation for a specific system one has to start with the Heisenberg equation of motion. For a closed system this equation reads

$$\dot{\hat{a}} = \frac{1}{i\hbar} [\hat{a}, \hat{H}_{\text{int}}], \quad (2.33)$$

where  $\hat{a}$  is the mode of interest and  $\hat{H}_{\text{int}}$  is the reversible system Hamiltonian. Closed systems do not interact with the environment. As we are dealing with an open system,

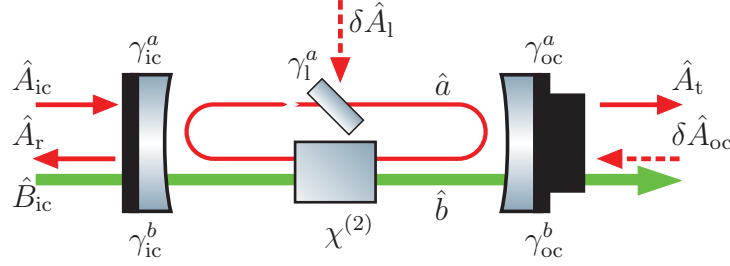


**Figure 2.7.:** Input and output fields of an OPA cavity [Göd16]. The operators  $\hat{A}_j$  and  $\hat{a}$  belong to the fundamental field, whereas the operators  $\hat{B}_j$  and  $\hat{b}$  belong to the second harmonic field and  $\gamma_j^{a/b}$  is the cavity decay rate for the fundamental and second harmonic field respectively. The field denoted with  $j = ic$  is the field, that is coupled into the cavity,  $j = r$  denotes the reflected field and  $j = t$  denotes the transmitted field. The losses are modeled via a beam splitter inside the cavity introducing vacuum noise as loss,  $j = l$ , and vacuum noise that couples into the cavity via the out-coupling mirror,  $j = oc$ .

the Heisenberg equation of motion must be expanded according to [GC85]

$$\dot{\hat{a}} = \frac{1}{i\hbar} [\hat{a}, \hat{H}_{\text{int}}] - [\hat{a}, \hat{a}^\dagger] \left( \gamma \hat{a} - \sqrt{2\gamma} \delta \hat{a}_{\text{env}} \right) + \left( \gamma \hat{a}^\dagger - \sqrt{2\gamma} \delta \hat{a}_{\text{env}}^\dagger \right) [\hat{a}, \hat{a}], \quad (2.34)$$

with  $\hat{a}$  being the system operator coupled to the cavity,  $\delta \hat{a}_{\text{env}}$  describing the environment and  $\gamma$  the damping constant/cavity decay rate.

The OPA needed to produce squeezing is shown in Fig. 2.7 containing all fields that are necessary in the squeezing process. It consists of the  $\chi^{(2)}$  nonlinear crystal and the two mirrors. One for coupling the fields into the cavity (IC) and one for coupling them out again (OC). The additional beam splitter inside the cavity models the losses (l).

The nonlinear process used in this form to generate squeezing is the degenerate parametric amplification. Note that there are more nonlinear processes, which are not used in the experiments performed in this thesis. For more detailed information about the other processes see [Boy08], as here we will concentrate on the degenerate parametric amplification. In this process one high frequency photon ( $\omega_b$ ) is annihilated and two photons with the same lower frequency ( $\omega_a$ ) are generated ( $2\omega_a = \omega_b$ ). The two corresponding fields are called the second harmonic  $\hat{b}$  at frequency  $\omega_b$  and the fundamental  $\hat{a}$  at the frequency  $\omega_a$  in analogy to the reverse process, the second harmonic generation. With the quantum Langevin equation we derive the time dependent intra cavity fields, which are in this case  $\hat{a}$  and  $\hat{b}$ . To find the full description of the cavity, we have to take into account all fields that can couple into the cavity, travel inside the cavity and

leave the cavity again. The fields that are coupled into the cavity are the strong second harmonic or pump field  $\hat{B}_{ic}$  and the weak seed beam at the fundamental frequency  $\hat{A}_{ic}$ , which is necessary in the locking loop, see Sec. 3.4. Additionally to these fields, vacuum fluctuations enter the cavity via the out-coupling mirror as  $\delta\hat{A}_{oc}$  and also losses inside the cavity add a contribution with vacuum fluctuations as  $\delta\hat{A}_l$ . The reflected field  $\hat{A}_r$  is used in the locking loop and the transmitted field  $\hat{A}_t$  is the one we are using in order to calculate the spectra of the generated squeezed field.

The reversible system Hamiltonian for the generation of squeezing reads as

$$\hat{H}_{\text{sys}} = \hbar\omega_a\hat{a}^\dagger\hat{a} + \hbar\omega_b\hat{b}^\dagger\hat{b} + \frac{i\hbar\epsilon}{2} \left( \hat{a}^{\dagger 2}\hat{b} - \hat{a}^2\hat{b}^\dagger \right), \quad (2.35)$$

where the first two terms refer to the energies of the fundamental field with the creation and annihilation operators  $\hat{a}^\dagger$  and  $\hat{a}$  at  $\omega_a$  and the second harmonic or pump field with the creation and annihilation operators  $\hat{b}^\dagger$  and  $\hat{b}$  at  $\omega_b$  respectively. The third term contains the interaction between the two fields, where  $\epsilon$  is the nonlinear interaction strength, containing information about the crystal nonlinearity, the interaction length, the phase matching and the beam focusing. It can be understood as either two photons of the fundamental field being created out of one pump photon or two photons of the fundamental field being destroyed in order to create a pump photon.

Inserting the Hamiltonian in Eq. (2.35) into the Langevin equation (2.34) and assuming that the fundamental field is resonant in the OPA cavity results in the two equations of motion for the fundamental and pump field

$$\dot{\hat{a}} = -\gamma_a\hat{a} + \epsilon\hat{b}\hat{a}^\dagger + \sqrt{2\gamma_a}\delta\hat{A}_{\text{env}} \quad (2.36)$$

$$\dot{\hat{b}} = -\gamma_b\hat{b} - \frac{\epsilon}{2}\hat{a}^2 + \sqrt{2\gamma_b}\delta\hat{B}_{\text{env}}, \quad (2.37)$$

where

$$\gamma_{a/b} = \gamma_{ic}^{a/b} + \gamma_{oc}^{a/b} + \gamma_l^{a/b} \quad (2.38)$$

are the decay rates for the in-coupling mirror (ic), the out-coupling mirror (oc) and the losses (l). The interaction with the environment is encoded in the last term

$$\sqrt{2\gamma_a}\delta\hat{A}_{\text{env}} = \sqrt{2\gamma_{ic}^a}\hat{A}_{ic} + \sqrt{2\gamma_{oc}^a}\hat{A}_{oc} + \sqrt{2\gamma_l^a}\hat{A}_l \quad (2.39)$$

$$\sqrt{2\gamma_b}\delta\hat{B}_{\text{env}} = \sqrt{2\gamma_{ic}^b}\hat{B}_{ic} + \sqrt{2\gamma_{oc}^b}\hat{B}_{oc} + \sqrt{2\gamma_l^b}\hat{B}_l \quad (2.40)$$

for each of the fields. In order to solve the system of coupled differential equations (2.36) and (2.37), it is useful to make a couple of assumptions in order to simplify the system. First of all, the finesse of the cavity is much higher for the fundamental field is much higher than for the second harmonic, i.e.  $\gamma_a \ll \gamma_b$ , hence the evolution of the pump field occurs rapid in comparison to the fundamental and therefore we can assume  $\dot{\hat{b}} = 0$ , cf. [Bow98]. Furthermore, for simplicity, we may assume no coupling to the environment, i.e.  $\gamma_{oc}^b = \gamma_1^b = 0$  resulting in  $\gamma_b = \gamma_{ic}^b$ . Finally, as the OPA is operated below threshold, i.e.  $\epsilon |\alpha|^2 \ll \sqrt{2\gamma_b} \bar{B}_{ic}$  with  $\bar{B}_{ic}$  being the expectation value of  $\hat{B}_{ic}$ , the pump depletion can also be neglected. With these assumptions we arrive at the expression

$$\hat{b} = \sqrt{\frac{2}{\gamma_b}} \hat{B}_{ic}, \quad (2.41)$$

which is then inserted into Eq. (2.36)

$$\begin{aligned} \dot{\hat{a}} &= -\gamma_a \hat{a} + \epsilon \sqrt{\frac{2}{\gamma_b}} \hat{B}_{ic} \hat{a}^\dagger + \sqrt{2\gamma_a} \delta \hat{A}_{env} \\ &= -\gamma_a \hat{a} + \Lambda \hat{B}_{ic} \hat{a}^\dagger + \sqrt{2\gamma_{ic}^a} \delta \hat{A}_{ic} + \sqrt{2\gamma_{oc}^a} \delta \hat{A}_{oc} + \sqrt{2\gamma_1^a} \delta \hat{A}_1. \end{aligned} \quad (2.42)$$

Here we used the abbreviation  $\Lambda = \sqrt{2/\gamma_b} \epsilon$  to shorten the expression.

Arriving at this equation enables us now to calculate the field spectra to investigate the influence of different parameters onto the generated squeezing. For this, we first linearize the equation using  $\hat{a} = \alpha + \delta \hat{a}$  and then drop all the nonfluctuating components. Further we assume that the fluctuations are small compared to the coherent amplitude, and therefore we neglect the higher order terms in the fluctuations  $\delta \hat{a}$ . Note that, in the linearization of the pump field, we use  $\hat{B}_{ic} = \beta_{ic} e^{-i\Phi_b} + \hat{B}_{ic}$  with now a real  $\beta_{ic}$ . This leads to

$$\delta \dot{\hat{a}} = -\gamma_a \delta \hat{a} + \Lambda \left( \beta_{ic} e^{-i\Phi_b} \delta \hat{a}^\dagger + \alpha \delta \hat{B}_{ic} \right) + \sqrt{2\gamma_{ic}^a} \delta \hat{A}_{ic} + \sqrt{2\gamma_{oc}^a} \delta \hat{A}_{oc} + \sqrt{2\gamma_1^a} \delta \hat{A}_1 \quad (2.43)$$

$$\delta \dot{\hat{a}}^\dagger = -\gamma_a \delta \hat{a}^\dagger + \Lambda \left( \beta_{ic} e^{i\Phi_b} \delta \hat{a} + \alpha \delta \hat{B}_{ic}^\dagger \right) + \sqrt{2\gamma_{ic}^a} \delta \hat{A}_{ic}^\dagger + \sqrt{2\gamma_{oc}^a} \delta \hat{A}_{oc}^\dagger + \sqrt{2\gamma_1^a} \delta \hat{A}_1^\dagger. \quad (2.44)$$

Using these two linearized operators we can define the quadrature fluctuation operators

$$\delta \dot{\hat{X}}^{a+}(\phi_b) = \left( \delta \dot{\hat{a}} + \delta \dot{\hat{a}}^\dagger \right) \quad (2.45)$$

$$\begin{aligned} &= -\gamma_a \delta \hat{X}^{a+} + \Lambda \beta_{ic} \left( e^{-i\Phi_b} \delta \hat{a}^\dagger + e^{i\Phi_b} \delta \hat{a} \right) + \Lambda \alpha \delta \hat{X}_{ic}^{B+} + \sqrt{2\gamma_{ic}^a} \delta \hat{X}_{ic}^{A+} \\ &\quad + \sqrt{2\gamma_{oc}^a} \delta \hat{X}_{oc}^{A+} + \sqrt{2\gamma_1^a} \delta \hat{X}_1^{A+} \end{aligned} \quad (2.46)$$

for the amplitude quadrature

$$\delta\dot{\hat{X}}^{a-}(\phi_b) = -i \left( \delta\hat{a} - \delta\hat{a}^\dagger \right) \quad (2.47)$$

$$\begin{aligned} &= -\gamma_a \delta\hat{X}^{a+} - \Lambda\beta_{ic}i \left( e^{-i\Phi_b} \delta\hat{a}^\dagger - e^{i\Phi_b} \delta\hat{a} \right) + \Lambda\alpha \delta\hat{X}_{ic}^{B-} + \sqrt{2\gamma_{ic}^a} \delta\hat{X}_{ic}^{A-} \\ &\quad + \sqrt{2\gamma_{oc}^a} \delta\hat{X}_{oc}^{A-} + \sqrt{2\gamma_1^a} \delta\hat{X}_1^{A-} \end{aligned} \quad (2.48)$$

and for the phase quadrature. These operators are time dependent. However in a measurement we usually address the frequency regime, therefore we Fourier transform these operators using  $FT[\delta\hat{c}(t)] = \delta\tilde{c}$  and  $FT[\delta\dot{\hat{c}}(t)] = -i\omega\tilde{c}(t)$  and find for the amplitude quadrature fluctuation

$$\begin{aligned} FT[\dot{\hat{X}}^{a+}(\Phi_b)] &= -i\omega\delta\tilde{X}^{a+} \\ &= -\gamma_a\delta\tilde{X}^{a+} + \Lambda\beta_{ic} \left( e^{-i\Phi_b} \delta\hat{a}^\dagger + e^{i\Phi_b} \delta\hat{a} \right) + \Lambda\alpha\delta\tilde{X}_{ic}^{b+} + \sqrt{2\gamma_{ic}^a} \delta\tilde{X}_{ic}^{a+} \\ &\quad + \sqrt{2\gamma_{oc}^a} \delta\tilde{X}_{oc}^{a+} + \sqrt{2\gamma_1^a} \delta\tilde{X}_1^{a+} \\ &= \frac{1}{\gamma_a - i\omega} \left( \Lambda\beta_{ic} \left( e^{-i\Phi_b} \delta\hat{a}^\dagger + e^{i\Phi_b} \delta\hat{a} \right) + \Lambda\alpha\delta\tilde{X}_{ic}^{b+} + \sqrt{2\gamma_{ic}^a} \delta\tilde{X}_{ic}^{a+} \right. \\ &\quad \left. + \sqrt{2\gamma_{oc}^a} \delta\tilde{X}_{oc}^{a+} + \sqrt{2\gamma_1^a} \delta\tilde{X}_1^{a+} \right) \end{aligned}$$

and analogously the phase quadrature fluctuation

$$\begin{aligned} FT[\dot{\hat{X}}^{a-}(\Phi_b)] &= \frac{1}{\gamma_a - i\omega} \left( -\Lambda\beta_{ic}i \left( e^{-i\Phi_b} \delta\hat{a}^\dagger - e^{i\Phi_b} \delta\hat{a} \right) + \Lambda\alpha\delta\tilde{X}_{ic}^{b-} + \sqrt{2\gamma_{ic}^a} \delta\tilde{X}_{ic}^{a-} \right. \\ &\quad \left. + \sqrt{2\gamma_{oc}^a} \delta\tilde{X}_{oc}^{a-} + \sqrt{2\gamma_1^a} \delta\tilde{X}_1^{a-} \right). \end{aligned}$$

As we are looking at the field that leaves the cavity we are looking at the transmitted quadrature fluctuation, for which the boundary condition

$$\delta\tilde{X}_t^{a+}(\Phi_b) = \sqrt{2\gamma_{oc}^a} \delta\tilde{X}^{a+}(\Phi_b) - \delta\tilde{X}_{oc}^{a+}(\Phi_b) \quad (2.49)$$

$$\begin{aligned} &= \frac{1}{\gamma_a - i\omega} \left( +\Lambda\beta_{ic} \left( e^{-i\Phi_b} \delta\hat{a}^\dagger + e^{i\Phi_b} \delta\hat{a} \right) + \sqrt{2\gamma_{oc}^a} \alpha \delta\tilde{X}_{ic}^{b+} + \sqrt{\gamma_{ic}^a \gamma_{oc}^a} \alpha \delta\tilde{X}_{ic}^{a+} \right. \\ &\quad \left. + (2\gamma_{oc}^a - \gamma_a + \Lambda\beta_{ic} + i\omega) \delta\tilde{X}_{oc}^{a+} + 2\sqrt{\gamma_1^a \gamma_{oc}^a} \delta\tilde{X}_1^{a+} \right) \end{aligned} \quad (2.50)$$

holds. With these lengthy terms it is possible to calculate the noise spectra in transmission via the calculation of the self correlations of the quadrature fluctuations. Here, we restrict the consideration to the pump phase  $\Phi_b = 0$  to keep the following equations

clearer. This results in the noise spectra in transmission

$$\begin{aligned}
V_t^{a\pm}(\Phi_b = 0) &= \langle \delta \tilde{X}_t^{a\pm}, \delta \tilde{X}_t^{a\pm\dagger} \rangle \\
&= \langle \delta \tilde{X}_t^{a\pm} \delta \tilde{X}_t^{a\pm\dagger} \rangle - \langle \delta \tilde{X}_t^{a\pm} \rangle \langle \delta \tilde{X}_t^{a\pm\dagger} \rangle \\
&= \frac{1}{\gamma_a - 2\gamma_a \Lambda \beta_{ic} + \Lambda^2 \beta_{ic}^2 + \omega^2} \left( 2\gamma_{oc}^a \alpha^2 \Lambda^2 V_{ic}^{b\pm} + 4\gamma_{ic}^a \gamma_{oc}^a V_{ic}^{a\pm} + 4\gamma_1^a \gamma_{oc}^a V_1^{a\pm} \right. \\
&\quad \left. + (4\gamma_{oc}^a + \gamma_a^2 + \Lambda^2 \beta_{ic}^2 - 4\gamma_{oc}^a \gamma_a \pm 4\gamma_{oc}^a \Lambda \beta_{ic} \mp 2\gamma_a \Lambda \beta_{ic} + \omega^2) V_{oc}^{a\pm} \right) \quad (2.51)
\end{aligned}$$

which resembles our measurement outcome if we use a balanced homodyne detector, see Sec. 3.7.

In Fig. 2.8 the output variances of the amplitude and phase quadrature are displayed over the detection frequency  $\omega$ , whereas the parameters used to generate this plot are listed in Tab. 2.1. What is clearly visible is that the amplitude quadrature is suppressed below the vacuum level, i.e. squeezed, for all detection frequencies and the phase quadrature is enhanced, i.e. anti-squeezed. Furthermore, for each frequency, the product of the variances of amplitude and phase quadrature has a lower bound defined by the Heisenberg uncertainty principle. Note that due to the losses we're not dealing with a pure squeezed vacuum state, which would be a minimum uncertainty state. Hence we see more anti-squeezing than squeezing.

---

<sup>1</sup>The nonlinear interaction strength depends on the nonlinear crystal, here it is shown for the example of periodically poled potassium titanyl phosphate (PPKTP), taken from [Jan07].

Quantity		Value
Wavelength of mode $\hat{a}$	$\lambda_a$	1064 nm
Wavelength of mode $\hat{b}$	$\lambda_b$	532 nm
Frequency of mode $\hat{a}$	$\omega_a$	$(2\pi \cdot c)/\lambda_a$
Frequency of mode $\hat{b}$	$\omega_b$	$(2\pi \cdot c)/\lambda_b$
Speed of light	$c$	$2.998 \cdot 10^8 \text{ ms}^{-1}$
Planck constant	$h$	$6.626 \cdot 10^{-34} \text{ Js}$
Cavity round trip path length	$d$	275 mm
Cavity round trip time	$\tau$	$d/c$
Nonlinear interaction strength for PPKTP <sup>1</sup>	$\Lambda = \sqrt{2/\gamma_b} \epsilon$	$1100 \cdot 10^{-4}$
Complex amplitude of mode $\hat{a}$	$\alpha$	1
Pump power $P$ dependent complex amplitude of mode $\hat{b}$	$\beta_{\text{ic}}(P)$	$\sqrt{(P \cdot \lambda_b)/(h \cdot c)}$
Overall Cavity decay rate of mode $\hat{a}$	$\gamma_a$	$1.2 \cdot 10^8$
Out-coupling cavity decay rate of mode $\hat{a}$	$\gamma_{\text{oc}}^a$	$0.1/\tau$
In-coupling cavity decay rate of mode $\hat{a}$	$\gamma_{\text{ic}}^a$	$0.0005/\tau$
Loss cavity decay rate of mode $\hat{a}$	$\gamma_{\text{l}}^a$	$0.0095/\tau$
Overall cavity decay rate for mode $\hat{b}$	$\gamma_b = \gamma_{\text{ic}}^b$	$0.95/\tau$
Out-coupling variance of mode $\hat{a}$	$V_{\text{oc}}^{a\pm}$	1
In-coupling variance of mode $\hat{a}$	$V_{\text{ic}}^{a\pm}$	1
Loss variance of mode $\hat{a}$	$V_{\text{l}}^{a\pm}$	1
In-coupling variance of mode $\hat{b}$	$V_{\text{ic}}^{b\pm}$	1

Table 2.1.: Values used to calculate Fig. 2.8.

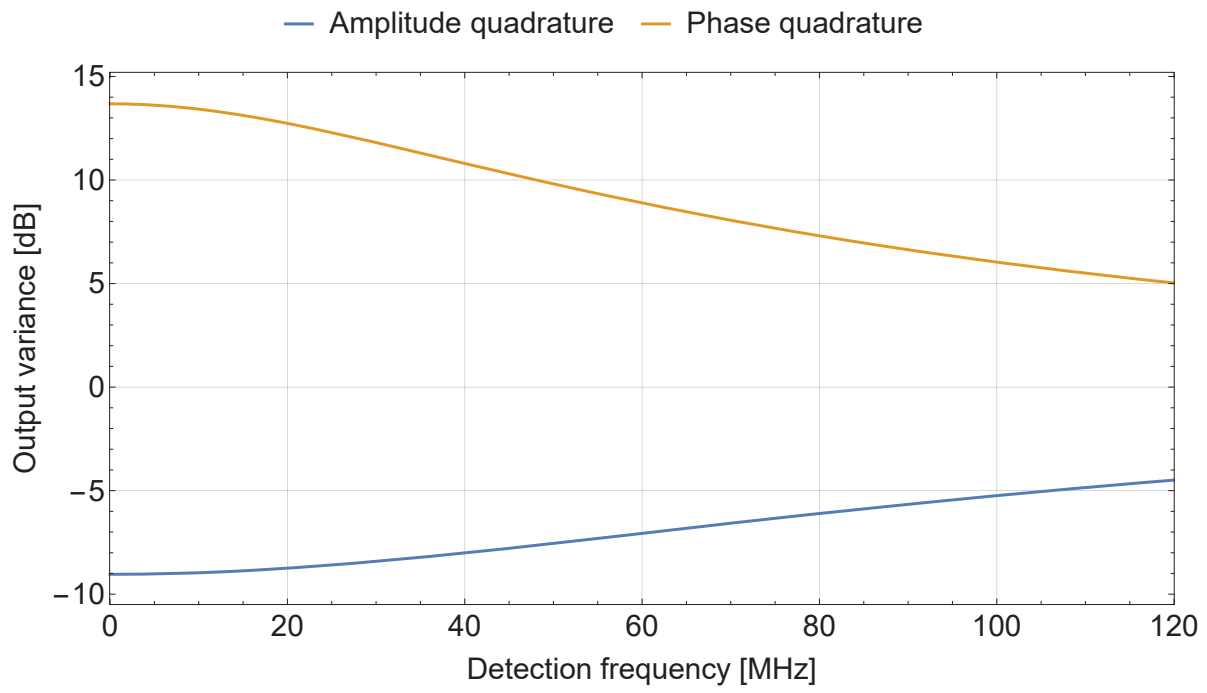
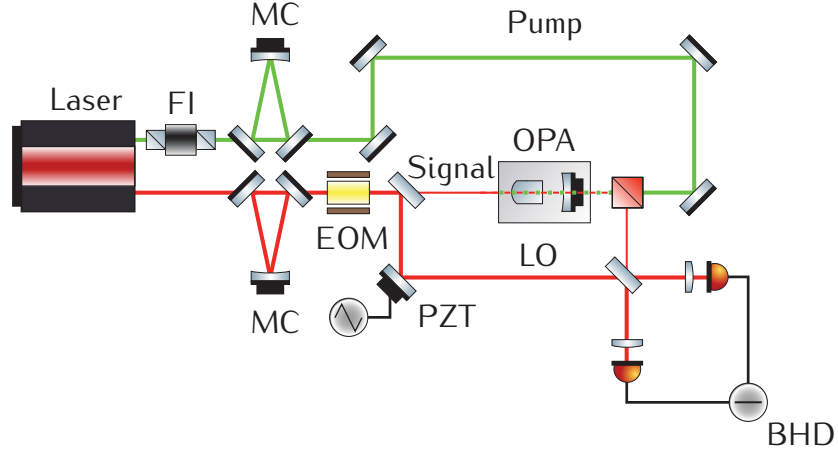


Figure 2.8.: Output of an OPA, normalized with respect to the vacuum, using the Heisenberg approach to simulate the squeezing and anti-squeezing for the phase  $\Phi_b = 0$ .

## Chapter 3.

# Experimental tools and techniques

Quantum optical experiments require a lot of complex components. This chapter gives an overview about optical components and experimental techniques used throughout this thesis. All explanations follow the outlines in [BR08, ST13, VW06, Boy08, Jan07, Lam98, Whi97] if not denoted otherwise.



**Figure 3.1.:** General setup for the generation and detection of a squeezed light field, as used in our laboratory. The laser generates two phase locked laser fields, one at 1064 nm (infrared) and one at 532 nm (green). The latter is generated through second harmonic generation inside the laser. The green laser is send through a Faraday Isolator (FI) to prevent back reflection into the laser. Both beams are temporally and spatially cleaned trough the mode cleaning cavity. The infrared laser beam is phase modulated by 35 MHz in the electro-optical modulator (EOM). Afterwards, the infrared beam is split into a strong local oscillator (LO) and a weak signal field, which is send into the optical parametric amplifier (OPA). Along with the signal field the strong green pump enters the OPA cavity. The squeezed field exiting the OPA is send to a 50:50 beam splitter, where it is overlapped with the LO. The relative phase between the squeezed field and LO is controlled by a piezo mounted mirror (PZT). This technique is known as balanced homodyne detector (BHD), see Sec. 3.7.

### 3.1. Laser System

The heart of optical experiments is the laser source. In our case we used an *INNO-LIGHT Diabolo* providing us with two phase locked laser beams and extremely stable frequencies, 2 MHz/min frequency drift, at the output. The active medium used in this laser is a neodymium doped yttrium aluminium garnet (Nd:YAG). The Nd:YAG crystal forms a monolithic ring oscillator, that is pumped by two electrically driven laser diodes, generating the infrared laser beam at 1064 nm. This monolithic layout ensures a high mechanical stability and results in the desired long term frequency stability. The infrared beam is sent through an optical isolator and an electro-optical modulator (EOM, c.f. Sec. 3.3), applying a phase modulation at 12 MHz onto the laser beam, before part of it is sent into an additional resonator, containing a nonlinear crystal to generate the second harmonic beam at 532 nm. This doubling resonator is electronically stabilized to the frequency of the Nd:YAG laser, resulting in an infrared beam of 246 mW at 1064 nm and the frequency doubled green beam of 423 mW at 532 nm, provided by the laser. As the phase modulation is applied onto the infrared beam before it enters the doubling resonator, each laser beam comes with a phase modulation, which is handy for controlling the following mode cleaning cavities.

The experiments described in this thesis use the green laser as the pump to induce the  $\chi^{(2)}$  nonlinear process inside the nonlinear crystal. The infrared laser serves two different purposes. Firstly, the infrared beam is split into signal and local oscillator beam. Part one, the signal beam, is used for the control of the cavity length in the squeezing process and in some cases for a coherent displacement of the generated quantum state. Part two, the local oscillator, is used in the balanced homodyne detection or, as we will see in Sec. 4, in the homodyne cross correlation measurement in order to quantify the generated state. For doing so, some more optical components and control systems for these components are necessary, which are explained in the following.

### 3.2. Mode Cleaner Cavity (MC)

For optical experiments that work below the shot noise limit, it is mandatory to have a laser that is spatially and temporally shot noise limited, because these experiments are extremely sensitive to spectral fluctuations and spatial mode-matching imperfections. This is achieved by using a ring resonator called mode cleaner (MC), which is used to

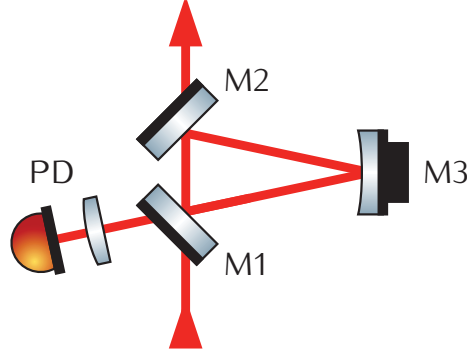


Figure 3.2.: Schematic of a mode cleaning cavity.

produce a pure spatial laser profile, i.e. produce a perfect Gaussian beam shape, and reduce the excess noise of the laser beam, see [WUG98, Ste08], to ensure a shot noise limited laser beam in the following experiments. The MCs are placed directly after the laser outputs in both the green and the infrared beams, each consisting of three mirrors. Two of them are just planar mirrors, M1 and M2. The third mirror, M3, on the other hand has a radius of curvature of 100 cm, refocusing the beam in the MC, and is mounted onto a piezo electric transducer, which allows us to change the total length of the resonator, cf. Fig. 3.2. The radius of curvature of mirror M3, along with the cavity length, defines the spatial eigenmode of the cavity. All three mirrors are mounted on a copper block which contains holes to transmit the light.

To quantify the quality of the resonator one can use the finesse. The finesse can be thought of as a quality factor for an optical resonator as it is dependent on the free spectral range  $\mathcal{FSR}$  and the full width at half maximum (FWHM)

$$\mathcal{F} = \frac{\mathcal{FSR}}{\text{FWHM}}. \quad (3.1)$$

These two quantities characterize an optical resonator as the  $\mathcal{FSR}$  gives information about the spectral distance between two resonant modes and the FWHM gives the width of each resonant mode. Combining both gives the number of round trips each mode does before leaving the resonator. The more round trips, the higher is the finesse and hence, the higher is the quality of the resonator.

In terms of the power reflectivities, the theoretical finesse is given for two mirrors with different reflectivities by, c.f. [ST13],

$$\mathcal{F} = \frac{\pi (R_1 R_2)^{\frac{1}{4}}}{1 - (R_1 R_2)^{\frac{1}{2}}}, \quad (3.2)$$

where  $R_1, R_2$  are the power reflectivities of the mirrors. For equal reflectivities  $R_1 = R_2 = R$  this expression reduces to

$$\mathcal{F} = \frac{\pi \sqrt{R}}{1 - R}, \quad (3.3)$$

where  $R$  is the reflectivity of the mirrors. In our case we have mirrors with a polarization dependent reflectivity, hence for different polarizations we have a different finesse called low ( $\mathcal{F}_l$ ) and high ( $\mathcal{F}_h$ ) finesse respectively. The reflectivity of the mirrors used in our setup for s-polarized light at 1064 nm and at an angle of incidence of  $43.5^\circ$  is  $r = 0.999717$  [Fil] resulting in the theoretical high finesse of 11089. P-polarized light, on the other hand, has a reflectivity of  $r = 0.992875$  again for  $43.5^\circ$  angle of incidence and 1064 nm resulting in the theoretical low finesse of 440. These values are only achieved in the experiment if the mirror surfaces are perfectly clean and correctly positioned. The dependence of the finesse on the correct position of the mirrors is useful in the building process, see Sec. 6.1. The experimentally achieved finesse for 1064 nm are  $\mathcal{F}_h = 11843$  and  $\mathcal{F}_l = 421.67$  respectively.

Quantifying the losses per round trip of the MC is possible by comparing the transmission in the high and low finesse cases respectively. In general the transmission through such a resonator is given by:

$$T_i = \left( \frac{1 - r_i^2}{1 - r_i^2 \delta} \right)^2, \quad (3.4)$$

with  $r_i^2 = R_i$  being the power reflectivity of the high and low finesse respectively and  $\delta$  the loss per round trip. Using Eq. (3.4) for both finesse along with the loss  $\delta$  and the relation between reflectivity and transmittivity  $R_i + T_i = r_i^2 + t_i^2 = 1$  one receives

$$\frac{T_h}{T_l} = \frac{I_h \cdot I_0}{I_0 \cdot I_l} \propto \frac{P_h}{P_l} \propto \frac{U_h}{U_l} = \left( \frac{t_h^2 (1 - (1 - t_l^2)(1 - \delta))}{t_l^2 (1 - (1 - t_h^2)(1 - \delta))} \right)^2, \quad (3.5)$$

where  $U_h=656$  mV and  $U_l=661$  mV are the voltages detected with a photo diode in transmission for the high and low finesse respectively, resulting in a total loss of  $\delta=4$  ppm<sup>1</sup>.

## Operation Mode

A MC is a ring resonator working as optical low pass filter where the edge frequency is defined as half the line width of the cavity. This works as, assuming the TEM00 mode is near resonance of the cavity, higher modes, like the TEM01, are far off resonance due to the Gouy phase shift between the modes [ST13]. In this way a specific frequency and consequently a specific mode is selected. Here it is the TEM00 mode that is transmitted and used in the experiments. All higher order modes are reflected. As the reflected modes are not required in the experiment, this signal is used for locking the MC on resonance with the Pound-Drever-Hall (PDH)[DHK83, Bla01] technique, see Sec. 3.4.

To achieve an optimal filtering it is necessary that the incoming laser beam fits the resonator eigenmode. The resonator eigenmode is defined by the wavelength of the laser beam, the resonator length, here 480.5 mm, and the radius of curvature of the mirror M3. To fit the incoming laser to the resonator eigenmode the laser is sent over a precisely adjusted distance through two lenses and onto two mirrors. With the mirrors the incidence of the laser onto the resonator is adjusted and the lenses manipulate the diameter of the beam, hence enabling us to mode match the laser mode onto the resonator eigenmode. Note that this mode matching is necessary for every cavity and detection scheme used in our experiments. The wavelength dependent waist size of the eigenmode of the MC, given by the radius of curvature of mirror M3 and the cavity length, for 1064 nm is 370  $\mu$ m and for 532 nm is 260  $\mu$ m.

## 3.3. Electro-Optic Modulator (EOM)

The equations and descriptions in the following subsection follow the explanations in [ST13].

An electro-optic modulator (EOM) utilizes the electro-optical effect occurring in anisotropic media in dependence of an electric field applied to that medium. These effects induce

---

<sup>1</sup>For more detailed notes see App. A

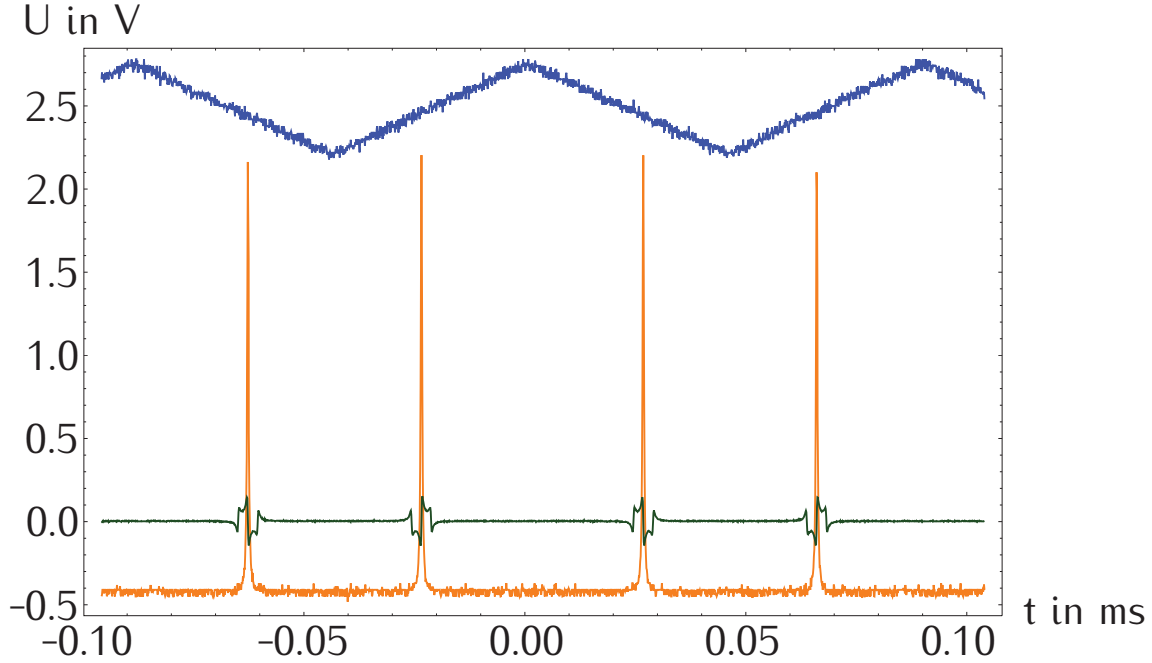


Figure 3.3.: When applying a ramp onto the piezo, blue line, to which the curved mirror is attached, we are changing the resonator length periodically, called scanning. For this, we excite different modes inside the MC. If correctly aligned, only the TEM00 mode is resonant and will be the only one visible while scanning the resonator. Note that if the amplitude of the ramp is large enough we can see one or more full  $\mathcal{FSR}$ . The orange line is the TEM00 mode transmitted through the MC. Using the Pound-Drever-Hall (PDH) technique, see Sec. 3.4, we can generate an error signal (green).

an appearance of or change in the birefringence of the medium due to a change in the refractive index  $n$ .

There are two known electro-optic effects, the Pockels effect and the Kerr effect. The Pockels effect is the linear change of the birefringence with the change in the electrical field strength. Hence, in the Pockels effect,  $\varsigma$  is negligibly small and therefore

$$n(E) = n_0 - \frac{1}{2}\tau n^3 E. \quad (3.6)$$

In our laboratory, we used a lithium niobate ( $\text{LiNbO}_3$ ) crystal which shows the Pockels effect. Hence in the following only the Pockels effect will be considered and a material

showing the Pockels effect, along with electrodes that provide the electrical field, will be referred to as Pockels cell.

When light is transmitted through a Pockels cell it undergoes a phase shift

$$\varphi \approx \varphi_0 - \pi \frac{\tau n^3 E l}{\lambda_0} \quad (3.7)$$

which depends on the length  $l$  of the cell, the electric field  $E$  and the wavelength  $\lambda_0$  of the transmitted light. This phase shift is used throughout our experiments to apply a phase modulation onto the laser field, necessary for the Pound-Drever-Hall technique, see Sec. 3.4, of the resonators in the experiments. The applied phase modulation in our case is in the range of MHz. If the alignment of the Pockels cell is not correct, i.e. the crystal axis and ray axis is neither perpendicular nor parallel, we also receive a change in the polarization.

The Pockels cell, see Fig. 3.4 used in our experiment contains a  $\text{LiNbO}_3$  crystal, which sides are cut in the Brewster angle to reduce the losses due to reflection. For the control of the electric field, two copper plates are placed on opposite sides of the  $\text{LiNbO}_3$  crystal, parallel to the direction of propagation of the light resulting in a transverse modulator.



**Figure 3.4.:** Schematic of the Pockels cell used in our experiments with the  $\text{LiNbO}_3$  crystal along with the two electrodes.

### 3.4. Pound-Drever-Hall (PDH) Technique

The Pound-Drever-Hall (PDH) technique is a commonly used control technique for optical resonators, see [DHK83, Pou46, Bla01]. In general, this technique is used to hold the length of the resonator stable, called locking, on resonance for the used laser field, i.e. frequency. If the resonator is locked on resonance, all resonant light is transmitted and hence we see a minimum in reflection. If the resonator drifts off of resonance, we see an increasing reflected intensity. This increase however provides not enough information for the control, as this increase is a consequence of a no longer fulfilled resonance condition which is given by the resonator length. The light of frequency  $\omega$  is only resonant in the

resonator if the resonator length is in integer multiple of the wavelength  $\lambda = c/2\pi\omega$ . If the resonator length is detuned from resonance, this condition is not necessarily fulfilled anymore. Now the increase in the reflected intensity is symmetric around resonance and can have two possible reasons: Either the resonator is too long for the used light to be resonant in the cavity or the cavity is too short. A correction of the resonator length in the wrong direction might cause a breakdown of the lock and hence of the measurement. However, the derivative of the reflected intensity is asymmetric around resonance and this provides us with the needed information for the locking. Fortunately there is a straightforward way to access the derivative in a measurement called the PDH technique, see Fig. 3.5. This technique uses a phase modulation at the frequency  $\Omega$  imprinted onto the light field by an EOM, see Sec. 3.3, resulting in sidebands before entering the resonator. The resulting field reads

$$E_{\text{inc}} = E_0 [J_0(\beta)e^{i\omega t} + J_1(\beta)e^{i(\omega+\Omega)t} - J_1(\beta)e^{i(\omega-\Omega)t}] , \quad (3.8)$$

where  $J_{0/1}(\beta)$  are Bessel functions and  $\beta$  is the modulation depth. This expression contains three different frequency components in the beam that are incident on the cavity which we want to stabilize. These three are the carrier at the frequency  $\omega$  and the two sidebands at the frequencies  $\omega \pm \Omega$ . This modulated beam is sent into the cavity and reflected, resulting in

$$E_{\text{ref}} = E_0 [F(\omega)J_0(\beta)e^{i\omega t} + F(\omega + \Omega)J_1(\beta)e^{i(\omega+\Omega)t} - F(\omega - \Omega)J_1(\beta)e^{i(\omega-\Omega)t}] \quad (3.9)$$

with the reflection coefficient  $F(\omega) = E_{\text{ref}}/E_{\text{inc}}$ , c.f. [Bla01].

The Faraday rotator (FR) and the polarizing beam splitter (PBS) prevent the reflected modulated light to reenter the laser and destabilize it and instead redirect the reflected intensity to a photo diode (PD), see Sec. 3.6, where the reflected signal is detected. As the PD detects the power rather than the fields, the detected signal is

$$\begin{aligned} P_{\text{ref}} &= |E_{\text{ref}}|^2 \\ &= P_c |F(\omega)|^2 + P_s \{|F(\omega + \Omega)|^2 + |F(\omega - \Omega)|^2\} \\ &\quad + 2\sqrt{P_c P_s} \{\text{Re}[F(\omega)F^*(\omega + \Omega) - F^*(\omega)F(\omega - \Omega)] \cos(\Omega t) \\ &\quad + \text{Im}[F(\omega)F^*(\omega + \Omega) - F^*(\omega)F(\omega - \Omega)] \sin(\Omega t)\} + O(2\Omega) \end{aligned} \quad (3.10)$$

with the nominal frequency  $\omega$ , an envelope with a beat pattern with frequencies at  $\Omega$ , arising from interference of carrier and sidebands, and  $2\Omega$ , arising from interference of

the sidebands. In Eq. (3.10), the  $2\Omega$  terms are only noted to exist but not specifically displayed, as they are not relevant in the PDH technique. However, the terms arising from the interference of the carrier and the sidebands scaling with the sine and cosine of  $\Omega$  are relevant, as these terms contain the phase of the reflected carrier in which we are interested.

The detected power is sent into an electronic mixer, where it is mixed with the same frequency used before in the EOM. The mixer multiplies both input signals and low pass filters them. The result of this multiplication and low pass filtering contains the sum and the difference of the mixed frequencies. If we are careful with the phase between the two input signals, the filtering of the signal results in the so-called error signal that is asymmetric around resonance, see Fig. 3.3. This error signal is a DC signal and, due to its asymmetry, it is now possible to decide on which side of the resonance we are and use this information to feed it back into the control loop. The control loop contains a proportional–integral (PI) controller, which gives the correction and a high voltage (HV) amplifier which applies the correction onto the piezo in the resonator, thereby actively controlling the piezo.

It is also possible, to use the transmitted field rather than the reflected one, which is used, e.g., for the locking of the pump phase in the squeezing process in the optical parametric amplifier (OPA).

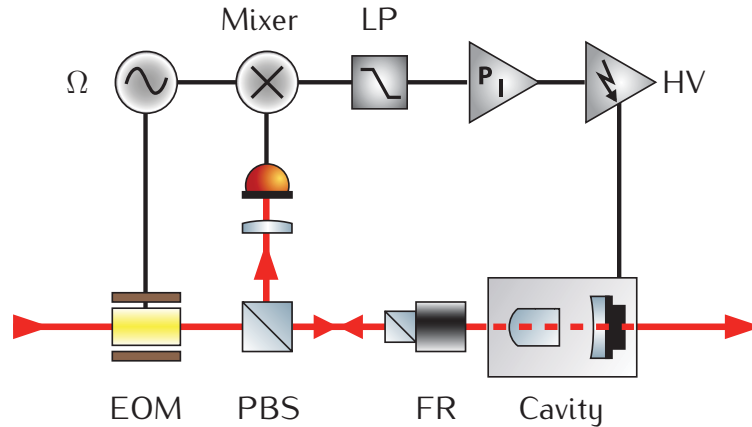


**Figure 3.5.:** Schematic of the PDH principle. The EOM phase modulates the laser field with the frequency  $\Omega$ , before it is sent into the cavity. The FR rotates the polarization of the light so that, on the PBS, the reflected beam is not transmitted but rather reflected and hence sent onto a PD. The PD signal is mixed down with  $\Omega$  in the mixer, low-pass filtered (LP) and then sent into the PID controller which gives a correction into the HV amplifier that drives the piezo in the resonator and hence controls the resonator length.

### 3.5. Optical Parametric Amplifier (OPA)

The following section follows the explanations in [BR08, Whi97, Jan07, Boy08]. Here, the theoretical description of an OPA given in 2.4 is completed by the description of the experimental implementation.

There are in total two OPAs in our laboratory, each containing a different crystal. The reason for this is rather a practical one, as the first crystal, magnesium oxide doped lithium niobate ( $\text{MgO:NbLiO}_3$ ), was easily available to start the first experiments and the second crystal, periodically poled potassium titanyl phosphate (PPKTP), was ordered shortly afterwards. Both crystals are coated on one side with an antireflection (AR) coating and on the other side with a highreflection (HR) coating. We choose this coating as we use a hemilithic cavity design in our experiments, see Fig. 3.6, cf. [BLB01, BSBL02, SLMS98, Hag10]. In these cavities, one mirror is the HR side of the crystal.

The efficiency of the optical parametric amplification in the crystal depends on the phase matching of the different beams involved. Perfect phase matching is achieved if

$$\Delta k = k_1 + k_2 - k_3 = 0, \quad (3.11)$$

where  $k_{1,2,3}$  are the wavevectors of the three contributing beams with the frequencies  $\omega_{1,2,3}$ . The difficulty here arises from the frequency dependent refractive index resulting in a non perfect phase matching. However, there are two different ways to achieve the perfect phase matching: either using a crystal that displays birefringence or use a periodically poled crystal, where the later results in quasi-phase matching. Birefringence is the effect that the refractive index depends on the polarization of the beams. We differ between two types of phase matching. In type *I* phase matching the two low frequency beams at  $\omega_1$  and  $\omega_2$  have the same polarization and the beam at  $\omega_3$  is orthogonally polarized to  $\omega_{1,2}$ , whereas in type *II* the  $\omega_1$  and  $\omega_2$  beams are orthogonally polarized. Furthermore, there are two different ways to tune phase matching to the perfect point. Either by tuning the angle or by tuning the temperature. The tuning by angle is only applicable if the propagation direction of the beam and the optical axes have an angle of  $0^\circ$  or  $90^\circ$  between each other. The tuning by temperature however is not restricted by that. For example, lithium niobate has a birefringence that is strongly temperature dependent.

Another way to achieve phase matching is using periodical poled crystals, which is called quasi phase matching. A periodical poling means that the crystal is fabricated

in a way that the orientation of one of the crystalline axes is inverted periodically as a function of position, where the period is twice the coherence length  $L_{\text{coh}}$ , see [Boy08]. Furthermore, here we are using the nonlinear coefficient  $d_{33}$  rather than an off-diagonal one we need quasi-phase matching. By switching the orientation, we are inverting the sign of the nonlinear coupling coefficient and thereby compensate the wavevector mismatch  $\Delta k \neq 0$ . Again the perfect phase matching can be achieved by tuning either the angle or the temperature.

In our experiments, we are using degenerate OPAs, where the two lower frequency beams have indeed the same frequency  $\omega_1 = \omega_2$ , called signal and idler, and therefore  $\omega_3 = 2\omega_1$ , called pump.

To actually produce squeezing in the OPA, more conditions must be met. For the precise design of the OPA, which depends on the crystal type, length and radius of curvature and reflectivities of the mirrors forming the cavity, the Boyd-Kleinman-theory was used. For more detailed information about the Boyd-Kleinman theory, see [BK68]. Following the Boyd-Kleinman-theory, we end up with, depending on the crystal and hence the sort of phase matching and crystal length, specifications of cavity length and beam diameter for signal and pump.

Fig. 3.6 shows the discussed hemilithic cavity. We send the control beam at  $\omega_1$  via a PBS into the cavity through the HR coated side of the crystal, also referred to as in-coupling mirror. The polarization of the reflected signal is turned using a rotator, so it is transmitted through the PBS, where it was reflected before, to be sent to the PD for the PDH locking, cf. Sec. 3.4. Along with the control beam, the pump at  $\omega_3$  is sent into the cavity. In contrast to the control beam, the strong pump enters the cavity through the PZT mirror, also referred to as out-coupling mirror, as the squeezed field exits the cavity through this mirror. The pump field induces the nonlinear effect in the OPA, resulting in parametric amplification and deamplification of the fundamental field, depending on the pump phase. In order to lock the pump phase on amplification or deamplification, resulting in phase or amplitude squeezing, we use the same PD we use for the cavity control. A fraction of the amplified and deamplified control field exits the cavity through the input coupler, i.e. the HR coated side of the crystal. Therefore, the PD now detects the parametric amplification and deamplification induced by the pump and, as the control field carries the modulated sidebands, we can use the same output of the PD with a second mixer to generate an error signal for the pump phase. In order to create a stable lock, we need to make sure that the two error signals of the OPA and the pump phase are out of phase, as they would influence each other otherwise. This is done while looking

at the error signal of the OPA in the locked case. If the phases of the two mixers and therefore of the error signals are not correctly aligned, we see parametric amplification and deamplification on the error signal of the OPA, which can be removed by tuning the phase of the error signal of the OPA. By locking the pump phase on deamplification, we generate a amplitude squeezed state and by locking the pump phase on amplification, we generate a phase squeezed state. The squeezed output is separated from the pump at a dichroic mirror and then send, e.g., to a balanced homodyne detector (BHD), see Sec. 3.7.

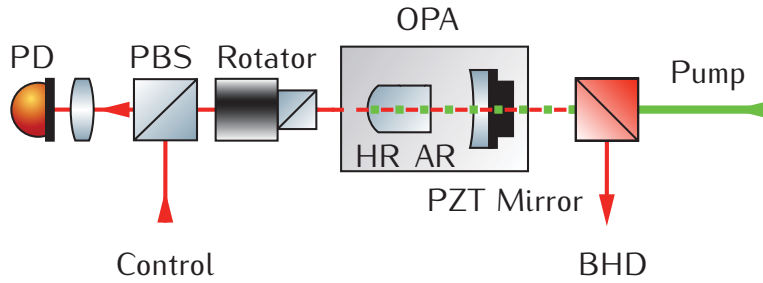


**Figure 3.6.:** Schematic of a hemilithic cavity used as OPA in our experiments. The control beam at 1064 nm, which is sent into the resonator through the HR coated side of the crystal, is used in the PDH locking and the pump at 532 nm, that enters the cavity through the PZT mirror, induces the nonlinear process. Through the PZT mirror, which is also referred to as out-coupling mirror, the squeezed field leaves the cavity and is separated from the pump field using a dichroic mirror.

### 3.6. Photo Diodes

The photo diodes (PD) are a crucial part of the experiment, where the actual photo diode, the light sensitive semiconductor, is embed into a transimpedance amplifier. The edge frequencies of the high pass (HP) and low pass (LP) filter, after the transimpedance amplifier and in front of the two outputs, define the actual purpose of the circuit. Note that out of convenience, we will in the following refer to the complete detector, containing the actual diode as well as the circuit, as PD. The HP filter leaves us with the fluctuations on the beam, used as input either for the mixer in the PDH or as input for the BHD. The LP filter, on the other hand, leaves us with a current that is proportional to the intensity of the incident light and gives us, on the one hand, information about the alignment of the cavities and, on the other hand, we can measure the overlap between two beams

by looking at the direct current (DC) output, which is handy e.g. in BHD. The edge frequency of the LP filter is usually around a few hundreds of kHz. Depending on the frequency range we want to use the PD for, we choose the HP filter.

In case of the locking diodes, the frequencies of interest are either 12 MHz or 35 MHz, which are the modulation frequencies for the PDH loops, hence usually we choose a frequency as edge frequency for the HP filter that contain these two below 12 MHz. In this way, the locking diodes are multifunctional for any locking loop in the experiment.

To measure quantum effects with a homodyne detector, one has to choose a lower edge frequency for the filters, as the quantum fluctuations are best detectable between 4 MHz and 8 MHz in our experiments. Below 4 MHz we see thermal and electrical fluctuations. Above 8 MHz the locking modulation frequencies, see Sec. 3.4, become dominant. Hence the edge frequency is chosen to be around 1 MHz to suppress the thermal and electrical fluctuations but still get all the fluctuations. Furthermore building homodyne PDs is more critical as they come in pairs. It is crucial that both PDs have the same transfer function and the same quantum efficiency. To receive comparable transfer functions, we made sure that both detectors see the same intensity. We ensured this, by measuring the intensity, which is proportional to the output voltage at the DC port, using an oscilloscope for each PD, with respect to the PD specific offset. The transfer function itself is measured between 10 kHz and 100 MHz with a network analyzer that also applies a modulation in the desired frequency range onto the used light source, here a laser diode. The quantum efficiency is quantified in a different way. We place the PD into the laser beam, as a quantum noise limited light source, and vary the laser power using a waveplate and a PBS. Now the laser power is measured with a power meter and for each measured power we measure the voltage at the DC output of the PD with the oscilloscope with respect to the offset along with the spectrum using a spectrum analyzer. Between each measurement the laser power is bisect and the dark noise of the PDs is subtracted. As we are dealing with quantum noise limited light, we expect a difference in the spectra of 3 dB between two laser powers. If this is not fulfilled, we are dealing with additional noise sources in the circuit. That this condition is fulfilled was tested for every PD used in the experiments. Using the voltage  $U$  at the DC output of the PD, in dependence of the corresponding laser power  $P$ , we can estimate the quantum efficiency  $\eta$  of the PD as

$$\eta = \frac{U \cdot h \cdot c}{R_{\text{TI}} \cdot P \cdot \lambda \cdot e}, \quad (3.12)$$

where  $R_{\text{TI}}$  is the impedance of the transimpedance amplifier,  $h$  is the Planck constant,  $c$  is the speed of light,  $\lambda$  the wavelength of the used light and  $e$  the elementary charge. The PDs used in the experiments presented in this thesis have a quantum efficiency  $\approx 95\%$ . Furthermore, for every pair of PDs that is supposed to work as homodyne detector, it is ensured that the transfer functions and the quantum efficiencies are equal, see App. B. This is achieved by using electrical components with small fabrication tolerances, e.g. resistors with  $<1\%$  tolerance. If the transfer functions and quantum efficiencies are not equal from the start, we have only limited options to adjust them, as these differences mainly arise from differences in the electrical components. Hence, we usually exchange the crucial electrical components, e.g. in the transimpedance amplifier, until we have equal transfer functions and spectra. The quantum efficiency depends on the used photo diode, here we mean the light sensitive semiconductor, and hence, the quantum efficiency can only be adjusted by changing the used photo diode in the circuit.

### 3.7. Balanced Homodyne Detection (BHD) and Quantum State Tomography

The balanced homodyne detection (BHD) is a standard technique throughout quantum optical experiments, see Fig. 3.7. It is comparable to a Mach-Zehnder interferometer. The signal and the local oscillator (LO) originate from the same source, are parted whereas the LO is much stronger than the signal. The signal is manipulated, e.g. send to an OPA to produce squeezing. An additional phase shift is applied to the LO, before both beams are recombined on a 50:50 beam splitter (BS).

In general, the two input beams can be described as

$$\alpha_{\text{in}}(t) = \alpha_{\text{in}} + \delta X_{\text{in}}^+(t) + \delta X_{\text{in}}^-(t) \quad (3.13)$$

$$\alpha_{\text{LO}}(t) = [\alpha_{\text{LO}} + \delta X_{\text{LO}}^+(t) + \delta X_{\text{LO}}^-(t)] e^{i\phi_{\text{LO}}}, \quad (3.14)$$

where  $\phi_{\text{LO}}$  is the relative phase between LO and signal, which is tuned by the phase shifter in the LO arm. The phase shift is introduced by a mirror that is mounted onto a piezo electric transducer (PZT).

As the LO is much stronger than the signal  $\alpha_{\text{LO}} \gg \alpha_{\text{in}}$  we can make a few assumptions. First of all, as we are dealing with a 50:50 BS the fields incident two detectors, D1 and

D2, read as

$$\alpha_{D1} = \sqrt{\frac{1}{2}} \alpha_{LO}(t) + \sqrt{\frac{1}{2}} \alpha_{in}(t) \quad (3.15)$$

$$\alpha_{D2} = \sqrt{\frac{1}{2}} \alpha_{LO}(t) - \sqrt{\frac{1}{2}} \alpha_{in}(t). \quad (3.16)$$

However, the detectors only detect intensities and convert them into a current. The difference current of the two detectors, which is our measurement signal, is

$$I_-(t) = 2\alpha_{LO} \left( \delta X_{in}^+(t) \cos(\phi_{LO}) + i\delta X_{in}^- \sin(\phi_{LO}) \right). \quad (3.17)$$

This difference current scales with the coherent amplitude of the LO,  $\alpha_{LO}$ , but the fluctuations of the LO,  $\delta X_{LO}^+$  and  $\delta X_{LO}^-$ , are suppressed. Therefore, even with a LO noise level above the quantum noise limit, the result would not be affected. Furthermore, the coherent amplitude of the signal  $\alpha_{in}$  has no influence on the difference current, whereas the fluctuations of the signal scale with the cosine and sine of the phase  $\phi_{LO}$ . Hence, by tuning the phase  $\phi_{LO}$  we can address either the fluctuations in the phase or the amplitude quadrature of the signal or a superposition of both,  $\hat{X}^{\Phi_{LO}}$ . This property allows us to fully characterize the quantum state under investigation.

In order to reconstruct the phase space functions introduced in Sec. 2.3.4, we need to measure the quadratures  $\hat{X}^{\Phi_{LO}}$  for different phases  $\Phi_{LO}$ . These measurements result in the quadrature distribution,  $\text{pr}(\hat{X}^{\Phi_{LO}}, \Phi_{LO})$ , of the investigated state. We then can use tomographic techniques, called quantum state reconstruction (QSR), see e.g. [Leo97, KVHS11], to compute the different phase space function. As this technique is a tomographic technique, i.e. measuring the marginals of an object, here the quadrature distribution of a quantum state, for different angles and reconstructing the original cross section from this, it is called quantum state tomography (QST). To do so efficiently, it is necessary to know the value of  $\phi_{LO}$ . One method is to fix the phase and gather the data for that specific phase. Then go on to the next phase and again gather the data for that specific phase [KVHS11], resulting in a discrete resolution in the phase. There is however an alternative approach, which will be discussed in more detail in Sec. 3.8.

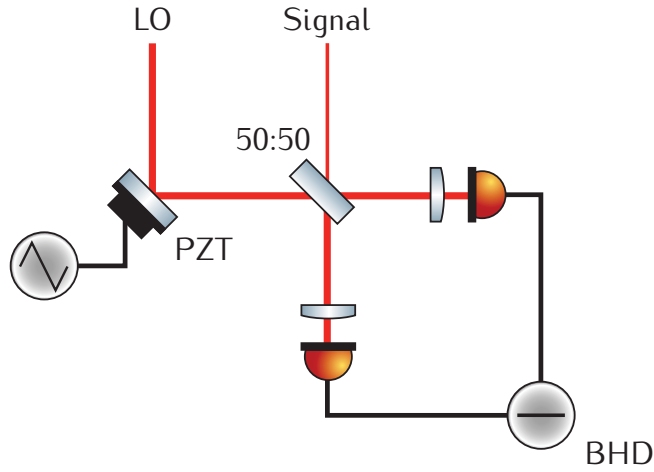
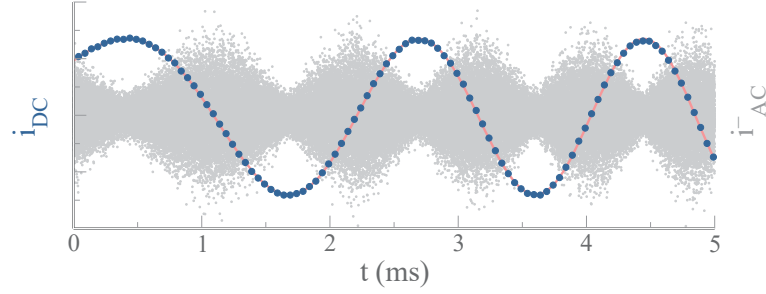


Figure 3.7.: Schematic of the BHD/QST principle.

### 3.8. Continuous Sampling

As mentioned above, in the common QST we are changing the relative phase  $\phi_{LO}$  between signal and LO in discrete steps. This, however, results in difficulties, as a continuous phase distribution is required for the quantum state reconstruction (QSR). If we perform only phase locked measurements (PLM), that means with discrete phase steps between two measurements, we need to interpolate between two phases. An idea of Semjon Köhnke, PhD student in our group, was to continuously vary the phase, rather than in discrete steps. This continuous sampling method, which we presented in [1], is a method to perform a QST with an arbitrarily high phase resolution, and an interpolation between the phases is not necessary.

In general the experimental setup for continuous sampling is similar to PLM, as the phase  $\phi_{LO}$  is tuned via a piezo mounted mirror. The difference is, that during the measurement, we apply a ramp onto the piezo resulting in a continuous scan over the full phase interval. By simultaneously measuring the alternating (AC) currents of the PDs, which carry the fluctuations of interest, the DC current of at least 1 PD, and the ramp, we can estimate the phase  $\phi_{LO}$  at every time step of the measurement. We do so by using the interference between signal and local oscillator, detected with the DC current of the PDs. This is possible, as the control beam we sent into the OPA, to lock the OPA and the pump phase, carries the optical phase of our signal. The interference of the control beam and LO on the DC output of the PDs then holds the information of the phase between signal and LO. This interference is investigated for each slope of the ramp applied onto the PZT, see Fig. 3.8. We can infer a sine function  $I_{DC} = a \sin(\varphi(t)) + b$



**Figure 3.8.:** Measured AC (gray dots) and DC (blue dots) currents for one slope of the ramp along with the fit (orange line).

with a certain amplitude  $a$  and an offset  $b$ . Due to the nonlinear but smooth response of the piezo over time we use a fourth-order polynomial  $\varphi(t) = gt^4 + ft^3 + et^2 + dt + c$  resulting in the fit function

$$I_{DC}(t) = a \sin(gt^4 + ft^3 + et^2 + dt + c) + b, \quad (3.18)$$

which is applied to the DC current. This fit provides us with the phase information necessary in the QSR yet in comparison to PLM with an arbitrary high resolution.

Continuous sampling is the technique of choice for the experiments performed throughout this thesis and the resulting publications [1, 2, 3].



## Chapter 4.

# Anomalous quantum correlations of squeezed light

The results presented in this chapter were achieved in cooperation with the *Theoretical Quantum Optics Group* of Prof. Dr. Werner Vogel, specifically in cooperation with Benjamin Kühn and were published in [3]. To be more precisely, the theoretical derivations and data analysis of this joint project was done by Benjamin Kühn. My part in this project concerned the design and building of the experimental setup, as well as the data acquisition.

The standard BHD presented in Sec. 3.7 has a lot of benefits, but it also has the disadvantage, that, for nonunity quantum efficiencies of the PDs, we measure actually a convolution of the true field strength distribution and a Gaussian noise distribution in which the efficiency  $\eta$  enters in the exponent, see [Vog95]. Therefore, for a decreasing  $\eta$ , the efficiency of the reconstruction also decreases and hence we need to pay attention to the quantum efficiencies. Still, by using BHD we can detect squeezing faithfully. Furthermore, the BHD is by design linear in the field, i.e., it addresses only the first and second order moments, further they are symmetrically ordered. To extract information about the nonclassical properties of the quantum state from these moments, we need to insert quantum mechanical commutation relations. As we usually deal with nonunity quantum efficiencies in real experiments, we are looking for a measurement technique to test nonclassicality that does not display this drawback. Moreover, we want a technique that can also address higher moments, to be more specific up to the fourth order normally ordered moments, that give a so far unknown insight into the quantumness of squeezed states.

One benefit of the presented experiment [3] and the corresponding theory [OHM87, Vog95] is that the problem in standard BHD, see Sec. 3.7, arising from nonunity quantum efficiencies of the PDs, is circumvented. Moreover, we use this approach to address the desired normally ordered moments of the intensity, the electrical field strength, and the correlation of both, up to the fourth order, without using commutation relations in the data analysis. To achieve this goal, we performed a four port homodyne detection with an unbalanced BS, the so called homodyne cross correlation measurement (HCCM), with a beam splitting ratio of 14:86, which we choose to be able to address the correlation of intensity and electrical field strength, combined with the continuous phase readout presented in Sec. 3.8 and [1].

But why should we struggle with a new detection scheme if BHD already gives the information about the squeezing and by using the QST we can even reconstruct the Husimi-Q, the Wigner, or the regularized Glauber-Sudarshan P-function? The answer is as simple as it is beautiful: The HCCM scheme presented here is able to show nonclassical effects even in an area of the phase where anti-squeezing, and, therefore, no squeezing is detected. Moreover, all calculations performed in this experiment are purely classical, hence, it delivers a direct proof of quantum physics, because the results of this experiment violate a classical inequality and can therefore not be explained in a classical sense.

The first part of this chapter addresses the theoretical description of the presented method, followed by the experimental details and the results achieved in combination of both.

## 4.1. Theoretical description

As mentioned above, the presented method was proposed by Werner Vogel in 1995 [Vog95]. In his paper, he theoretically analyzed two different measurement schemes: the homodyne intensity correlation measurement (HICM) and the HCCM. The benefit of both measurement schemes is, that the PD quantum efficiency enters as a prefactor rather than through a convolution like in BHD. Hence, these methods are not that sensitive to nonunity quantum efficiencies of PDs. The HICM method was originally introduced in [Vog91] and just recently experimentally realized to certify quadrature squeezing in resonance fluorescence light from a single quantum dot [SJJ15]. As this measurement

scheme was not used in our experiment, it is not further discussed here. Hence, this chapter concentrates on the HCCM, which was not realized experimentally before.

The HCCM has some crucial differences to the standard BHD. First of all the LO power is of the same order of magnitude as the signal power. The second difference is, that, rather than subtracting the electric current fluctuations of the two detectors, their correlation is analyzed. The two AC time sequences  $[\tilde{c}_1^{(1)} \cdots \tilde{c}_1^{(N_\phi)}]_\phi$  and  $[\tilde{c}_2^{(1)} \cdots \tilde{c}_2^{(N_\phi)}]_\phi$ , each containing  $N_\phi$  points, are measured for different phases  $\phi$ . The resulting same-time correlation

$$C(\phi) = \overline{\tilde{c}_1(\phi)\tilde{c}_2(\phi)} = \frac{1}{N_\phi} \sum_{\ell=1}^{N_\phi} \tilde{c}_1^{(\ell)}(\phi) \tilde{c}_2^{(\ell)}(\phi) \quad (4.1)$$

is proportional to the intensity noise correlation  $\Delta G^{(2,2)}(\phi) = \langle \Delta I_1 \Delta I_2 \rangle_\phi$ , where  $\langle \cdot \rangle$  is the classical expectation value, as the used detectors are working in a linear regime for the used intensities,  $I_1$  and  $I_2$ , which are the intensities detected by the two PDs in the experimental HCCM setup. Hence, the same-time correlation can be written as

$$C(\phi) = \zeta_1 \zeta_2 \Delta G^{(2,2)}(\phi), \quad (4.2)$$

where  $\zeta_1$  and  $\zeta_2$  are prefactors containing the detection efficiencies and the gain factors of our PDs. The intensity noise correlation  $\Delta G^{(2,2)}(\phi)$  is phase dependent and consists of three components

$$\Delta G^{(2,2)}(\phi) = \Delta G_0^{(2,2)} + \Delta G_1^{(2,2)}(\phi) + \Delta G_2^{(2,2)}(\phi), \quad (4.3)$$

each with a distinct dependence on the LO phase and electric field strength. Furthermore, these three components contain different information of intensity and electrical field strength noise, as well as the correlation of both. We define the coefficients  $\mathcal{T}_i$  by  $\mathcal{T}_0 = 1$ ,  $\mathcal{T}_1 = |R|/|T| - |T|/|R|$ ,  $\mathcal{T}_2 = -1$  and  $\mathcal{T} = |T|^2|R|^2$ , where  $|T|^2$  and  $|R|^2$  are the intensity transmission and reflection coefficients of the BS respectively. The contributions are given as follows:

The first term,

$$\Delta G_0^{(2,2)} = \mathcal{T} \mathcal{T}_0 \langle (\Delta I)^2 \rangle, \quad (4.4)$$

is independent of the phase  $\phi$  and the LO field strength  $E_L$  and gives information about the signal intensity noise  $\Delta I = I - \langle I \rangle$ .

The second term,

$$\Delta G_1^{(2,2)}(\phi) = \mathcal{T}\mathcal{T}_1 E_L \langle \Delta E_\phi \Delta I \rangle, \quad (4.5)$$

with the signal electric field strength  $E_\phi = E_\phi^{(+)} + E_\phi^{(-)}$  and the corresponding fluctuation  $\Delta E_\phi = E_\phi - \langle E_\phi \rangle$ , is linear dependent on the electric field strength of the LO and  $2\pi$  periodic in phase. One important property of this term is, that the corresponding moment  $\langle \Delta E_\phi \Delta I \rangle$  contains two noncommuting observables, namely  $\Delta E_\phi$  and  $\Delta I$ , which is why it is referred to as an anomalous moment and is hard to access experimentally. This is remarkable as the Heisenberg uncertainty principle prevents us from measuring two noncommuting observables simultaneously, yet we can address a moment containing both. To observe this anomalous moment, we introduced the second alteration in the setup compared to BHD. The splitting ratio of the BS is in our experiment 14:86 as the visibility for the anomalous moment  $\langle \Delta E_\phi \Delta I \rangle$ , arising from the prefactors  $\mathcal{T}\mathcal{T}_1$  in Eq. (4.5), is highest for this splitting ratio.

The third and final term,

$$\Delta G_2^{(2,2)}(\phi) = \mathcal{T}\mathcal{T}_2 E_L^2 \langle (\Delta E_\phi)^2 \rangle, \quad (4.6)$$

is quadratic with the electric field strength of the LO and  $\pi$  periodic in phase. This  $\pi$  periodicity results from the fact, that  $E_\phi$  is  $2\pi$  periodic and consequently the second order moment is  $\pi$  periodic.

These three different terms in Eq. (4.3) can be extracted from the same-time correlation  $C(\phi)$  using either the phase dependency or the dependency of the electrical field of the LO. We want to point out that these three different moments are simultaneously addressed in a single experiment.

Note that the expressions (4.4)–(4.6) are also correct for a lossy BS with  $|T|^2 + |R|^2 < 1$ . The corresponding theory in [Vog95] can also be extended to an asymmetric BS, see [UWTP16]. This extension was necessary, as the BS in the performed experiment was indeed a lossy BS. For such an asymmetric BS, the intensity reflection–transmission ratio is  $|R_L|^2 : |T_L|^2$  for the LO and for  $|R_S|^2 : |T_S|^2$  the signal. This yields the more general coefficients  $(\mathcal{T}_0, \mathcal{T}_1, \mathcal{T}_2) = ((|R_S|/|R_L|)(|T_S|/|T_L|), |R_S|/|T_L| - |T_L|/|R_S|, -1)$  and  $\mathcal{T} = |T_S||T_L||R_S||R_L|$ . However, we may assume symmetric transmittance, i.e.  $|T_S|^2 = |T_L|^2$ , as both beams, the signal and the LO, are transmitted through the BS and, therefore, experience the same losses. The asymmetry results from the reflectance of our BS, as it

is different for the LO and the signal side, due to the fact that the BS has a beam splitter coating on the one side and an anti-reflex coating on the other side. Hence, one beam, here the signal beam, is directly reflected on the beam splitter coating side, whereas the other, here the LO, passes the anti-reflex coating, is transmitted through the BS once, reflected on the back side of the beam splitter coating and then again transmitted through the BS, see Fig. 4.1. Therefore, this beam experiences additional losses in the reflected arm, that the signal beam does not experience, and, therefore, the reflection coefficients are not the same for both beams.

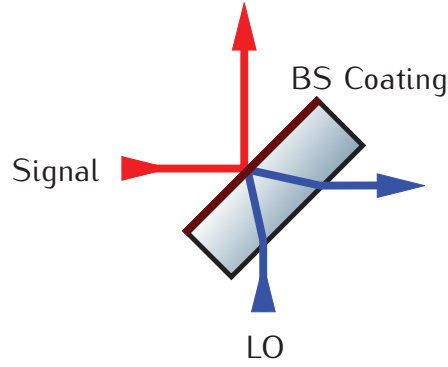


**Figure 4.1.:** Visualization of the asymmetry in the reflection coefficients for signal and LO. The signal beam, red, is directly reflected on the side of the BS with the beam splitter coating (BS Coating). The LO beam, blue, must pass the BS medium, is reflected on the BS coating and passes the BS medium again.

## 4.2. Experimental setup

The experimental setup is displayed in Fig. 4.2. The OPA, see Secs. 2.4 and 3.5, containing a magnesium oxide-doped lithium niobate ( $\text{MgO}:\text{LiNbO}_3$ ) crystal, was pumped with 243 mW at 532 nm resulting in a gain of 2.3 to generate a coherently displaced phase squeezed state of -2.7 dB squeezing and 5.5 dB anti-squeezing. The coherent displacement is necessary, as the LO power must be in the range of the signal power, in order to see all the contributions in Eq. (4.3) from the HCCM. If the signal is a squeezed vacuum state, this would result in a too low total power to be detected by our PDs. We achieved the coherent displacement by inserting a strong control beam into the cavity, rather than a weak one, resulting in 284  $\mu\text{W}$  of signal power. This is sufficient for our PDs to actually detect the light and, therefore, the quantum fluctuations. Furthermore, additional contributions in  $\Delta G^{(2,2)}(\phi)$  arise from classical fluctuations of the LO, where

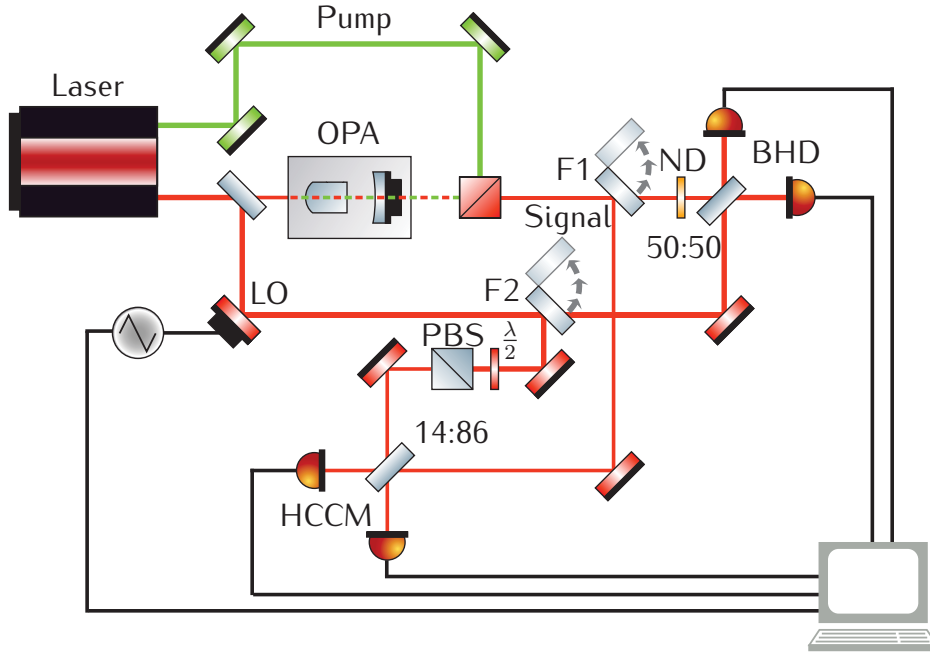


**Figure 4.2.:** Experimental setup for the generation and detection of a coherently displaced phase squeezed state. The squeezed state was generated in an OPA using a strong control beam to induce the coherent displacement. For the detection, the flip mirrors F1 and F2 are used to send the squeezed state and the LO either into the HCCM or the BHD.

the dominant effect is a constant offset. This constant offset is obtained by a measurement with blocked signal, which yields a direct observation of the intensity fluctuation of the LO, including the occurring correlated dark noise in the two detectors. In order to correct this effect, the constant offset is removed from the measured correlation  $C(\phi)$  with unblocked signal. Moreover, even if uncorrelated dark noise in both detectors were stronger than the quantum noise of the signal, it does not influence the measurement result.

The detection step consists not only of the HCCM, but also of a BHD, which is used to perform an independent state characterization with an established technique. To switch between both measurement techniques, we use the flip mirrors F1 and F2, see Fig. 4.2. However, the relatively high signal power used in our experiment raises a problem as in a common BHD, low signal powers of a few tens of  $\mu\text{W}$  and a much stronger LO power of around 1 mW are used resulting in a ratio of approx. 30, see Sec. 3.7. If we would keep this ratio for our coherently displaced squeezed state, we would need a LO power of 10 mW to do BHD and this would destroy our PDs. To circumvent this problem, we placed a neutral density (ND) filter in the signal beam port of the BHD. In this way we reduce the signal power in the BHD to  $32\mu\text{W}$  and a LO power of 1.03 mW is sufficient

to perform BHD. Of course the reduction of the signal power also reduces the squeezing detected by the BHD, but since we know the ratio of power reduction, we can estimate the initial squeezing. In both detection steps we use the continuous sampling technique, cf. Sec. 3.8, and filtered the AC data from 4–8 MHz.

As the extraction of the different moments (Eqs. (4.4)–(4.6)) requires either to measure the same-time correlation  $C(\phi)$  (Eq. (4.1)), the AC times sequences for different phases or different electric field strengths of the LO, two different techniques were used for the variation of these parameters. The phase variation and readout was done using the continuous phase readout scheme as shown in Sec. 3.8 and Ref. [1]. The variation of the LO electric field strength was achieved by a combination of a PBS and a waveplate in the LO arm of the HCCM. The intensity of the LO was measured with a power meter. Moreover, as two of the three terms of  $\Delta G^{(2,2)}(\phi)$ , namely  $\Delta G_0^{(2,2)}(\phi)$  and  $\Delta G_2^{(2,2)}(\phi)$ , contain a phase-independent part, an additional measurement with a blocked LO is necessary, resulting in the measured same-time correlation  $C_{\text{block}}$ .

Note, that the variance of the signal measured with the blocked LO for the investigated coherently displaced phase squeezed state, must fulfill the necessary classicality condition  $\langle(\Delta I)^2\rangle \geq 0$ .

### 4.3. Results

As mentioned above, the same-time correlation  $C(\phi)$  is proportional to the intensity noise correlation  $\Delta G^{(2,2)}(\phi)$ . Hence, the contributions

$$C_k(\phi) = \zeta_1 \zeta_2 \Delta G_k^{(2,2)}(\phi) \quad (4.7)$$

with  $k = 0, 1, 2$  can be separated from the total correlation  $C(\phi)$ , which is given by a second degree trigonometric polynomial

$$C(\phi) = a_0 + \sum_{k=1}^2 [a_k \cos(k\phi) + b_k \sin(k\phi)] \quad (4.8)$$

with the real parameters  $a_k$  and  $b_k$ , as proposed in [Vog95]. The individual contributions  $C_k(\phi)$  with  $k = 0, 1, 2$  are obtained from these measurements as

$$C_0(\phi) = C_{\text{block}} \quad (4.9)$$

$$C_1(\phi) = a_1 \cos(\phi) + b_1 \sin(\phi) \quad (4.10)$$

$$C_2(\phi) = a_2 \cos(2\phi) + b_2 \sin(2\phi) + a_0 - C_{\text{block}}. \quad (4.11)$$

Note that, we are using the sum of sine and cosine to not restrict ourself to pure phase squeezing.

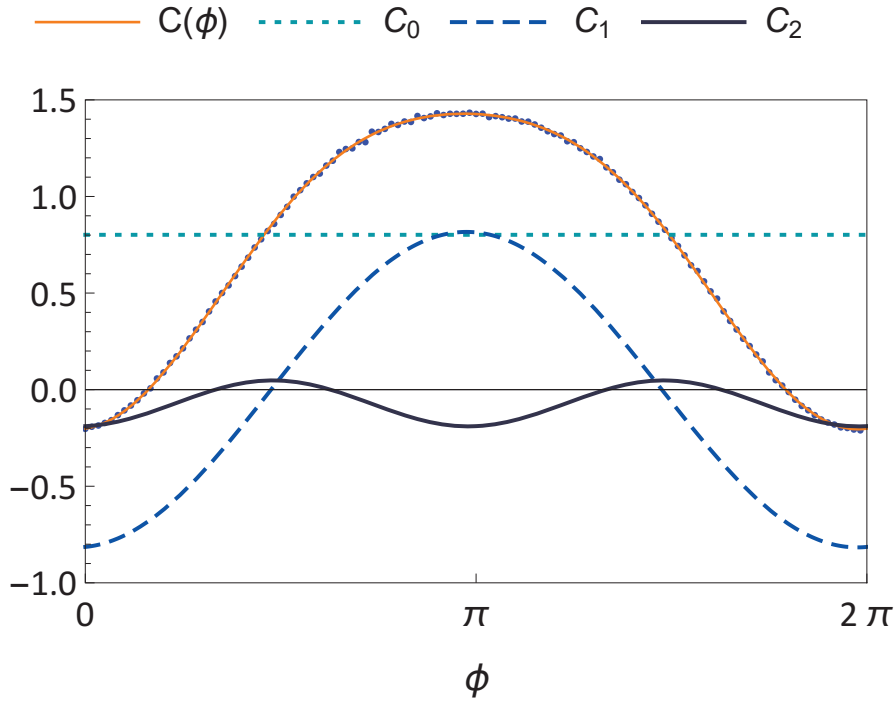


**Figure 4.3.:** The measured correlation  $C(\phi)$  (blue markers) as a function of phase. The error bars of one standard deviation statistical uncertainty are within the size of the markers. The fit according to Eq. (4.8) is shown by the thin solid orange curve, composed of the contributions  $C_0$  (dotted line),  $C_1$  (dashed line) and  $C_2$  (solid blue line).

In Fig. 4.3 the measured same-time correlation  $C(\phi)$  as a function of the phase  $\phi$  is shown as the blue markers for 120 phases equidistantly distributed in the interval  $[0, 2\pi]$ . Note that even though we continuously sample the phase we use here only 120 phases, which is sufficient in the analysis. The orange line is the theoretical fit according to Eq. (4.8). The three different components  $C_0$ ,  $C_1$  and  $C_2$  are extracted from  $C(\phi)$  by the different phase dependencies. They are displayed as the light blue dotted line  $C_0$ , the blue dashed line  $C_1$ , and the solid dark blue line  $C_2$ . They show the characteristic phase

dependencies, where  $C_0$ , the intensity noise moment, is phase independent and hence just a constant value.  $C_1$ , the intensity field strength noise correlation moment, is  $2\pi$  dependent on the phase, and  $C_2$ , the field noise moment, is  $\pi$  periodic in phase.

As mentioned above, the different contributions can also be separated by the distinct dependence on the LO field strength. Therefore, we probed the five different LO powers 0 (blocked LO), 117, 166, 216 and 275  $\mu\text{W}$ , still using the continuous phase sampling method, but only using the phases  $\phi = 3\pi/4$  and  $\phi + \pi$ . This is reasonable as the intensity noise correlation  $\Delta G^{(2,2)}(\phi)$  fulfill for every state the properties

$$\Delta G_0^{(2,2)}(\phi) = \Delta G_0^{(2,2)}(\phi + \pi), \quad (4.12)$$

$$\Delta G_1^{(2,2)}(\phi) = -\Delta G_1^{(2,2)}(\phi + \pi), \quad (4.13)$$

$$\Delta G_2^{(2,2)}(\phi) = \Delta G_2^{(2,2)}(\phi + \pi). \quad (4.14)$$

The result of this separation is shown in Fig. 4.4, where the blue filled dots mark the measured correlations  $C(\phi = 3\pi/4)$  and the unfilled dots mark the measured correlations  $C(\phi + \pi)$  for the different LO field strengths rescaled to the randomly chosen LO power 166  $\mu\text{W}$ . This rescaling is done, as it is not crucial to know the exact value of the LO power for the subsequently introduced nonclassicality criterion, but rather the ratios between the different LO powers, and hence we can choose any reference power. The orange lines are the theoretical fits according to Eq. (4.8). The contribution  $C_0$  is shown as the light blue dotted line and displays, as expected, no dependence on the LO field strength.  $C_1$  is shown as the blue dashed line and is linearly dependent on the LO field strength and the contribution  $C_2$  is displayed as the dark blue line and is quadratically dependent on the LO field strength.

However, we are not stopping with the mere separation of the different moments from the measured correlation. We formulated a classical inequality and inserted these separated moments.

Such an inequality can be formulated with the extracted moments in terms of the Cauchy-Schwartz inequality

$$\langle \Delta E_\phi \Delta I \rangle^2 \leq \langle (\Delta I)^2 \rangle \langle (\Delta E_\phi)^2 \rangle, \quad (4.15)$$

which is always fulfilled by classical states. As we know the beam splitting ratios for an asymmetric beams splitter, which we used to define the coefficients  $\mathcal{T}_0$ ,  $\mathcal{T}_1$  and  $\mathcal{T}_2$  we can

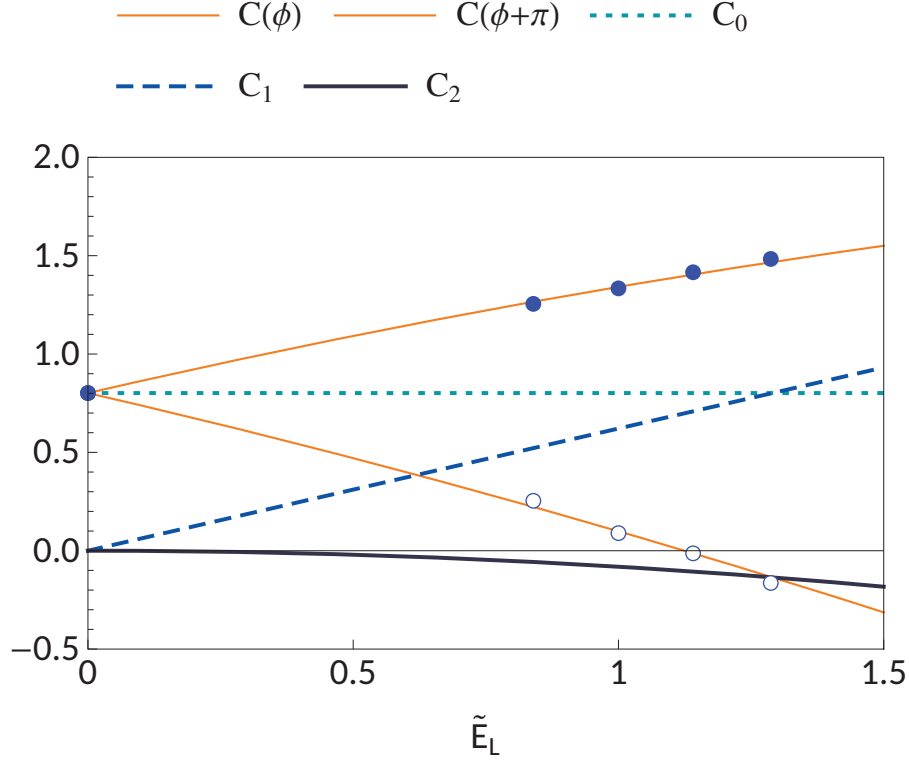


**Figure 4.4.:** The measured correlation  $C(\phi)$  (filled markers) and  $C(\phi + \pi)$  (unfilled markers) for  $\phi = 3\pi/4$  and  $\phi + \pi$ , respectively, as a function of the rescaled LO field strength  $\tilde{E}_L$ . The error bars of one standard deviation statistical uncertainty are within the size of the markers. The quadratic fits are composed of the contributions  $C_0$  (dotted line),  $C_1$  (dashed line), and  $C_2$  (solid blue line).

rewrite this inequality

$$(C_1(\phi)/\mathcal{T}_1)^2 \leq C_0(\phi)/\mathcal{T}_0 \cdot C_2(\phi)/\mathcal{T}_2, \quad (4.16)$$

where the contributions  $C_k(\phi)$  are extracted from the measured correlation  $C(\phi)$ . We rewrite Eqs. (4.15) and (4.16) to

$$M(\phi) = \langle (\Delta I)^2 \rangle \langle (\Delta E_\phi)^2 \rangle - \langle \Delta E_\phi \Delta I \rangle^2 \geq 0 \quad (4.17)$$

and

$$L(\phi) = C_0(\phi)/\mathcal{T}_0 \cdot C_2(\phi)/\mathcal{T}_2 - (C_1(\phi)/\mathcal{T}_1)^2 \geq 0 \quad (4.18)$$

and, therefore, these two inequalities are related via

$$L(\phi) = \zeta_1^2 \zeta_2^2 \mathcal{T}^2 E_L^2 M(\phi). \quad (4.19)$$

As the only difference between both is the positive prefactor  $\zeta_1^2 \zeta_2^2 \mathcal{T}^2 E_L^2$ , it is obvious that the sign of  $L(\phi)$  and  $M(\phi)$  is equal. Therefore, to test the necessary condition Eq. (4.15) for a classical correlated signal, it is sufficient to directly show  $L(\phi) \geq 0$ . Note, that no knowledge of the efficiencies and gain factors of the detection process is required. Furthermore, only the ratios  $|R_L|^2 : |T_L|^2$  and  $|R_S|^2 : |T_S|^2$  are needed in the calculation and not the transmittance and reflectance itself. This makes the test robust against BS losses.

The classical inequality (4.15) contains no precognition on quantum theory, such as noncommuting operators. Hence, a violation of this inequality shows nonclassicality of the investigated state without knowledge or acceptance of quantum physics, as a violation of this inequality cannot be explained by any classical theory.

In Fig. 4.5 we show  $L(\phi)$  for the probed displaced squeezed state, as a function of the phase  $\phi$ . The figure is divided in a classically allowed region for nonnegative values of  $L(\phi)$  and a region for negative values of  $L(\phi)$ , which indicates nonclassical correlations. As the investigated state is a squeezed state, we included a shaded area which marks the region where the detection of squeezing, e.g. with a BHD, is sufficient to show the nonclassical correlation of the input state. The blue solid line in Fig. 4.5 is the function  $L(\phi)$  for the measured squeezed state obtained via the phase dependency. It is significantly negative for a wide range of phases  $\phi$ , which is a clear violation of the classicality condition Eq. (4.15) for almost all phases. As an example, for  $\phi = 3\pi/4$  no squeezing is present and still the classicality condition Eq. (4.15) with a significance of 28 standard deviations. This is a remarkable result, as it means, that the anomalous quantum correlations are not limited to a phase region where squeezing is present, but they are also present in the antisqueezed phase region.

The blue dot in Fig. 4.5 is the value of  $L(\phi)$  obtained by the separation through LO field strength for the phase  $\phi = 3\pi/4$ . Again, we find a clear violation of Eq. (4.15) outside of the region where squeezing would prove nonclassicality. The larger error bar results from the fact that we do not scan the LO field strength continuously like we did with the phase, but rather we change the LO field strength in 5 discrete steps. Therefore, a drift of the squeezing ellipse yields a larger uncertainty than the separation by phase. However, even with the higher uncertainty we still reach a significance of 4.7 standard deviations for the separation by LO field strength.

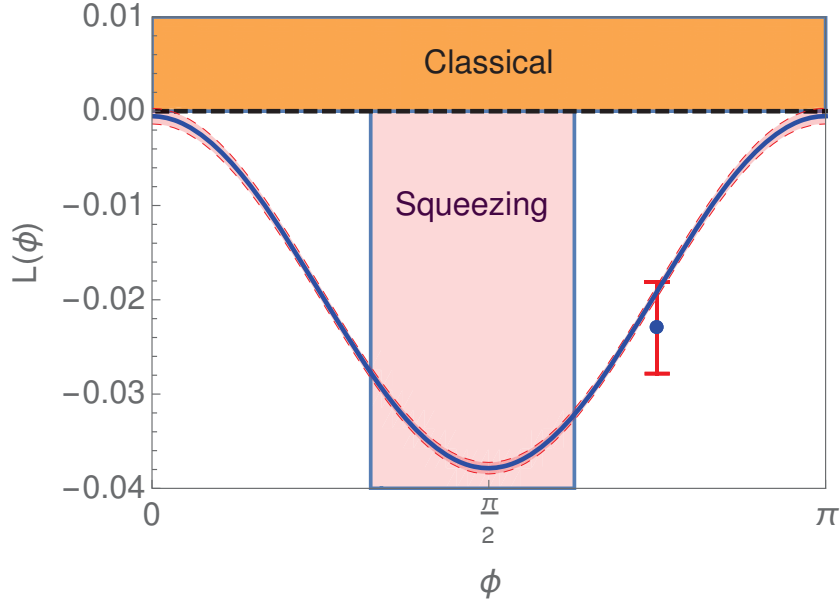


**Figure 4.5.:** The solid line shows  $L(\phi)$  as a function of phase as obtained through separation by different phase periodicity. Due to the  $\pi$ -periodicity of the plot, we confine ourselves to the interval  $[0, \pi]$ . The thin dashed lines correspond to an error of one standard deviation. The thick dashed line marks the border between the classical and nonclassical regions. Squeezing is present within the light-colored interval. The marker at  $\phi = 3\pi/4$  (anti-squeezed region) follows from the separation by the LO field strength from data measured for  $\phi$  and  $\phi + \pi$ . The error corresponds to one standard deviation.

#### 4.4. Summary and conclusions

In summary, we performed the first experimental realization of the 1995 proposed HCCM. With this measurement, we are able to observe up to forth-order moments of the field fluctuations of the investigated coherently displaced phase squeezed state. Moreover, we measured the moments of three pairwise noncommuting observables in a single measurement scenario. This enables us to determine even an anomalous moment  $\langle \Delta E_\phi \Delta I \rangle$  composed of two noncommuting observables, intensity and field noise fluctuation with a high significance. The extracted moments can be used in a quantum correlation test. This shows that anomalous quantum correlations exists even outside the squeezing region of phases, which is especially beneficial if we are looking at a strongly squeezed state, as the squeezed phase interval decreases with increased squeezing. Moreover, this may be beneficial for the detection of quantum effects under demanding conditions. Finally, it is noteworthy, that the data analysis is free of any quantum physical assumptions and, hence, a violation of Eq. (4.15) is a direct violation of classical physics.

## Chapter 5.

# Witnessing the degree of nonclassicality

The aim of this chapter is to introduce an experimentally accessible method to quantify the degree of nonclassicality for arbitrary quantum states of harmonic oscillator systems, based on the quantum superposition principle. For doing so we first give a general definition of our nonclassicality measure according to [GSV12, VS14] before we proceed presenting the witnessing approach given in [4]. The formulated witnesses are applied to different quantum states. This witnessing approach is also experimentally accessible, e.g. in terms of the quadrature variances.

The results presented here are a further development of the results gained during my Master thesis in the *Theoretical Quantum Optics Group* of Prof. Dr. Werner Vogel. During my Master project, I elaborated the witnessing approach and the optimization of the witness. While during PhD, we further developed the approach and presented different witnesses for the amount of nonclassicality, also being experimentally accessible.

### 5.1. Introduction

As mentioned in Sec. 2.3.4, we can distinguish classical and nonclassical states on the basis of the  $P$ -function. Now we want to address the issue of quantifying the identified nonclassicality. There are different approaches to quantify the nonclassicality of a system. One attempt uses the trace distance of a given quantum state to the set of all classical states [Hil87, MKN11a, Hil89]. Another distance based measure is based on the Bures distance [MMS02]. Other measures employ the Hilbert-Schmidt norm [DMMW99, DMMW00] or especially in quantum information-science, the Fisher information [Hal00]. Alternatively, a method was introduced using the negativities occurring

in the  $P$ -function. There the idea is to measure the amount of Gaussian noise necessary to remove the negativities of the corresponding  $P$ -function [Lee91, Lee95, LB95]. Also, the potential of a state to generate entanglement is a proposed way to quantify nonclassicality [ACR05]. This, however, connects the quantification of nonclassicality to the quantification of entanglement. The quantification of entanglement is possible, e.g., using the Schmidt number [HHHH09, GT09, SV11a, SV11c], which is the entanglement measure that is most closely related to the quantum superposition principle, which happens to be the foundation of quantum correlations, cf. e.g. [RBH01]. As the two problems of quantifying nonclassicality and entanglement are similar problems, the idea was to adapt the knowledge about the quantification of entanglement using the Schmidt number and apply it to quantify the nonclassicality. The Schmidt number results from the decomposition of entangled states into superpositions of pure separable states, which have a tensor product form. The state is more entangled for an increasing number of superpositions of separable states. Now we are looking for an analogon for nonclassicality. Recently the amount of nonclassicality for pure and mixed states was defined from an operational and an algebraic point of view, denoted as the degree of nonclassicality [GSV12, VS14]. This degree is based on the decomposition of a quantum state into superpositions of coherent states. The coherent states are chosen, because they resemble the behavior of the classical harmonic oscillator most closely, cf. Sec. 2.2.2 and [Gaz09]. Our measure of nonclassicality is related to the number of superposition of coherent states which are necessary to represent the quantum state and the more superposition needed the higher is the degree of nonclassicality. This is the measure of choice for our witnessing of the degree of nonclassicality.

### 5.1.1. General definition

As mentioned above, we want to decompose an arbitrary pure quantum state into superpositions of coherent states,

$$|\psi_r\rangle = \lambda_1 |\alpha_1\rangle + \dots + \lambda_r |\alpha_r\rangle, \quad (5.1)$$

where  $\lambda_k \in \mathbb{C} \setminus \{0\}$  and  $|\alpha_k\rangle$  are coherent states for  $k = 1, \dots, r$  with  $r$  being the minimal number of superpositions of coherent states and, therefore, our degree of nonclassicality [GSV12, VS14]. The states of a specific number of superpositions  $r$  form a set  $\mathcal{S}_r$ , which is the closure of all pure states with a number of superpositions less than or equal to  $r$ . As this definition applies to pure states only and we aim to consider mixed states as

well, we define the mixed states using a convex roof construction,

$$\hat{\rho}_r = \int_{|\psi_r\rangle \in \mathcal{S}_r} dP_{\text{cl}}(\psi_r) |\psi_r\rangle \langle \psi_r|, \quad (5.2)$$

where  $P_{\text{cl}}$  is a classical probability distribution. All these states  $\hat{\rho}_r$  are elements of the following closed, convex set:

$$\mathcal{M}_r = \overline{\text{conv}\{|\psi_r\rangle \langle \psi_r| : |\psi_r\rangle \in \mathcal{S}_r\}}. \quad (5.3)$$

We find the closure in the trace norm, because it is the simplest norm for operators and, as all norms are equivalent, the norm can be chosen arbitrarily. With this definition, we can now give the full definition for the degree of nonclassicality of an arbitrary quantum state  $\hat{\rho}$ . We have

$$\hat{\rho} \in \mathcal{M}_r \Leftrightarrow D_{\text{Ncl}}(\hat{\rho}) \leq r, \quad (5.4)$$

$$\hat{\rho} \notin \mathcal{M}_r \Leftrightarrow D_{\text{Ncl}}(\hat{\rho}) > r, \quad (5.5)$$

$$\hat{\rho} \in \mathcal{M}_r \setminus \mathcal{M}_{r-1} \Leftrightarrow D_{\text{Ncl}}(\hat{\rho}) = r, \quad (5.6)$$

whereas the last equation means, that the degree of nonclassicality is equal to  $r$  if and only if  $\hat{\rho}$  lies in  $\mathcal{M}_r$ , but not in  $\mathcal{M}_{r-1}$ . That also implies that we need to find the optimal decomposition of our quantum state into superpositions of coherent states. Here we seek for a witnessing approach and an optimization of the witness found.

### 5.1.2. Witnessing approach

The problem at hand, deciding whether a quantum state  $\hat{\rho}$  lies in a specific set  $\mathcal{M}_r$  or not, is comparable to decide whether a point lies in a specific convex set or not. Hence, we can use an approach known from convex geometry, the Hahn–Banach separation theorem, see e.g. [Yos08], in order to formulate a witness for our degree of nonclassicality. Applying it to our specific problem, we can state that for any state  $\hat{\rho} \notin \mathcal{M}_r$  there exists a Hermitian operator  $\hat{K}$  such that

$$\langle \hat{K} \rangle = \text{tr}(\hat{\rho} \hat{K}) > b_r(\hat{K}). \quad (5.7)$$

The parameter

$$b_r(\hat{K}) = \sup_{|\psi_r\rangle \in \mathcal{S}_r} \frac{\langle \psi_r | \hat{K} | \psi_r \rangle}{\langle \psi_r | \psi_r \rangle} \quad (5.8)$$

can decide whether or not the state lies in a specific closed, convex set or not. It is the least upper bound and denotes the maximally attainable expectation value of  $\hat{K}$  for states in  $\mathcal{M}_r$ .

The Hahn-Banach separation theorem for our task is schematically depicted in Fig. 5.1. The different closed, convex, nested sets are shown as ellipses for different  $r$  and tangent hyperplanes  $b_r$ . Every state on the right of such a hyperplane, given by  $b_r$ , cannot be an element of the set  $\mathcal{M}_r$ .

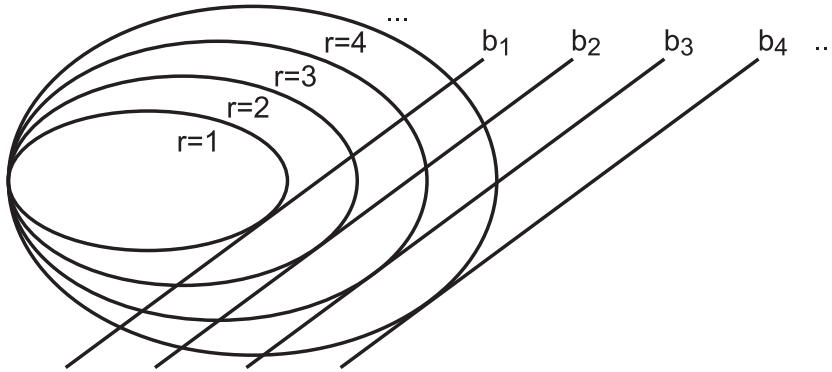


**Figure 5.1.:** Schematic representation of the application of the Hahn-Banach separation theorem. The sets  $\mathcal{M}_r$  are depicted as ellipses for several  $r$  with the tangent hyperplanes, which allow to determine whether or not the investigated state lies in a specific set  $\mathcal{M}_r$ . The parameter  $b_r$  defines this hyperplane.

With the parameter  $b_r(\hat{K})$  we can now define our witness operator

$$\hat{W}_r = b_r(\hat{K})\hat{1} - \hat{K}, \quad (5.9)$$

which has the properties that

$$\text{Tr}(\hat{\rho}\hat{W}_r) \geq 0 \quad \forall \quad \hat{\rho} \in \mathcal{M}_r \quad (5.10)$$

$$\text{Tr}(\hat{\rho}\hat{W}_r) < 0 \quad \forall \quad \hat{\rho} \notin \mathcal{M}_r. \quad (5.11)$$

Using the witness operator in the definition of the degree of nonclassicality leads to

$$\text{Eq. (5.4)} \Leftrightarrow \forall \hat{W}_r : \text{Tr}(\hat{\rho}\hat{W}_r) \geq 0, \quad (5.12)$$

$$\text{Eq. (5.5)} \Leftrightarrow \exists \hat{W}_r : \text{Tr}(\hat{\rho}\hat{W}_r) < 0, \quad (5.13)$$

and, therefore, we obtain the necessary and sufficient condition that a quantum state  $\hat{\rho}$  has a degree of nonclassicality of  $r$ ,  $D_{\text{Ncl}}(\hat{\rho}) = r$ , if and only if

$$\exists \hat{W}_{r-1} : \text{Tr}(\hat{\rho}\hat{W}_{r-1}) < 0 \text{ and } \forall \hat{W}_r : \text{Tr}(\hat{\rho}\hat{W}_r) \geq 0, \quad (5.14)$$

which is equivalent to the definition in Eq. (5.6).

Analogously to this approach, we can also consider the infimum in Eq. (5.8) in order to construct a witness

$$\hat{W}'_r = \hat{K} - b'_r(\hat{K})\hat{1} \text{ and } b'_r(\hat{K}) = \inf_{|\psi_r\rangle \in \mathcal{S}_r} \frac{\langle \psi_r | \hat{K} | \psi_r \rangle}{\langle \psi_r | \psi_r \rangle}. \quad (5.15)$$

Hence, we need to rewrite Eq. (5.7) to

$$\langle \hat{K} \rangle = \text{tr}(\hat{\rho}\hat{K}) < b'_r(\hat{K}), \quad (5.16)$$

which means that the measured expectation value  $\langle \hat{K} \rangle$  is below the bound  $b'_r(\hat{K})$  and this is the minimal possible expectation value of  $\hat{K}$  for states in the set  $\mathcal{M}_r$ .

Note that the sets  $\mathcal{M}_r$  have a nested structure and, therefore, it holds

$$\begin{aligned} \mathcal{M}_1 &\subset \mathcal{M}_2 \subset \dots \subset \mathcal{M}_\infty, \\ b_1(\hat{K}) &\leq b_2(\hat{K}) \dots \leq b_\infty(\hat{K}), \\ b'_1(\hat{K}) &\geq b'_2(\hat{K}) \dots \geq b'_\infty(\hat{K}). \end{aligned} \quad (5.17)$$

### 5.1.3. Optimization

The definition of  $b_r(\hat{K})$  leads directly to the optimization problem,

$$b_r = \frac{\langle \psi_r | \hat{K} | \psi_r \rangle}{\langle \psi_r | \psi_r \rangle} \rightarrow \text{optimum}, \quad (5.18)$$

with respect to  $|\psi_r\rangle \in \mathcal{S}_r$ . Here the maximum  $b_r(\hat{K})$  (see Eq. (5.7)) of all optima  $b_r$  is

$$b_r(\hat{K}) = \sup b_r \quad (5.19)$$

and, similarly, for the minimum (see Eq. (5.16)) of all optima,

$$b'_r(\hat{K}) = \inf b_r. \quad (5.20)$$

Inserting the definition of  $|\psi_r\rangle$  from Eq. (5.1) into Eq. (5.18) results in

$$b_r = \frac{\sum_{k,l=1}^r \lambda_k^* \lambda_l \langle \alpha_k | \hat{K} | \alpha_l \rangle}{\sum_{k,l=1}^r \lambda_k^* \lambda_l \langle \alpha_k | \alpha_l \rangle}. \quad (5.21)$$

In order to find the least upper bound of Eq. (5.21), we use the necessary optimization conditions

$$0 = \frac{\partial b_r}{\partial \lambda_k^*} \quad \text{and} \quad 0 = \frac{\partial b_r}{\partial \alpha_k^*} \quad (5.22)$$

for  $k = 1, \dots, r$ . Now, the first condition Eq. (5.22) in combination with Eq. (5.18) is computed to be

$$\sum_{l=1}^r \langle \alpha_k | \hat{K} | \alpha_l \rangle \lambda_l = b_r \sum_{l=1}^r \langle \alpha_k | \alpha_l \rangle \lambda_l, \quad (5.23)$$

or in vectorial notation

$$\mathcal{G}_{\hat{K}} \Lambda = b_r \mathcal{G}_1 \Lambda, \quad (5.24)$$

with  $\Lambda = (\lambda_l)_{l=1}^r$  and the matrix  $\mathcal{G}_{\hat{L}}$  for operators  $\hat{L}$  defined as

$$\mathcal{G}_{\hat{L}} = (\langle \alpha_k | \hat{L} | \alpha_l \rangle)_{l=1}^r. \quad (5.25)$$

In Eq. (5.24) the value  $b_r$  corresponds to a generalized eigenvalue. Therefore, we can apply standard methods in the treatment of eigenvalue problems to our problem at hand. Note, that with an increasing number of superpositions  $r$ , the dimensionality of Eq. (5.24) increases as well.

Similarly the second condition in Eq. (5.22) is combined with Eq. (5.18) and can be rewritten to

$$0 = \lambda_k^* (\langle \alpha_K | \hat{a} \hat{K} | \psi_r \rangle - \langle \alpha_k | \hat{a} | \psi_r \rangle), \quad (5.26)$$

where we can assume, without loss of generality, that  $\lambda_k \neq 0$ , as for the case  $\lambda_{k_0} = 0$  for some  $k_0$  the degree of nonclassicality  $r_0$  would be smaller than  $r$ . This allows us to rewrite Eq. (5.26) also in vectorial notation,

$$\mathcal{G}_{\hat{a}\hat{K}} \Lambda = b_r \mathcal{G}_{\hat{a}} \Lambda. \quad (5.27)$$

Note that we started with two necessary optimality conditions and end up with two eigenvalue equations with the same eigenvalue  $b_r$ . Hence, it is sufficient to solve only one of the to eigenvalue equations. Here we use Eq. (5.23).

The above results, also presented in [4], describe the general approach to design a witness of the degree of nonclassicality. In the following, we will apply this approach to some examples using different operators  $\hat{K}$ , also addressing a general numerical implementation.

## 5.2. Previous results

Here we consider some results which have been previously presented in our publication [4]. To achieve these results, we applied our method to some examples and consider analytical and numerical solutions for different degrees of nonclassicality  $r$ .

The simplest example is for the case  $r = 1$ , which simplifies the optimization condition (5.24) to  $b_1 = \langle \alpha_1 | \hat{K} | \alpha_1 \rangle$ , which is straightforward solvable for any operator  $\hat{K}$ . In order to construct a corresponding witness operator, we may consider an operator  $\hat{f} = f(\hat{a}^\dagger, \hat{a})$ , which is a function of the annihilation,  $\hat{a}$ , and creation operator,  $\hat{a}^\dagger$ . Defining

$$\hat{K} =: \hat{f}^\dagger \hat{f} :, \quad (5.28)$$

where  $: \cdot :$  denotes the normal ordering prescription, and one obtains the bound

$$b_1 = |f(\alpha_1^*, \alpha_1)|^2 \geq 0. \quad (5.29)$$

Using this definition in the witness construction in Eq. (5.15) including the minimal eigenvalue  $b_1$  we arrive at the witness operator

$$\hat{W}_1 = \hat{K} - 0 =: \hat{f}^\dagger \hat{f} : . \quad (5.30)$$

Note that this witness is in the case  $b'_r(\hat{K}) = \inf_{\alpha_1} |f(\alpha_1^*, \alpha_1)|^2 > 0$  not optimal. The optimal witness in this case is

$$\hat{W}_1^{(\text{opt})} =: \hat{f}^\dagger \hat{f} : - b'_r(\hat{f}^\dagger \hat{f}) \hat{1}, \quad (5.31)$$

which is an even finer witness than  $\hat{W}_1$ . Note that there is an equivalent definition for finer or optimal witness in [LKCH00]. This is however the trivial case. Let us now move on to more advanced cases with  $r > 1$ , starting with  $r = 2$ . For  $r = 2$ , Eq. (5.24) is the eigenvalue problem of a 2x2 matrix. The solutions of these eigenvalue problems, are given analytically, namely

$$b_2^\pm = \frac{1}{2} [\text{Tr}(\mathcal{G}_1^{-1} \mathcal{G}_{\hat{K}}) \pm \Delta] \quad (5.32)$$

$$\Delta = \sqrt{[\text{Tr}(\mathcal{G}_1^{-1} \mathcal{G}_{\hat{K}})]^2 - 4 \det[\mathcal{G}_1^{-1} \mathcal{G}_{\hat{K}}]}. \quad (5.33)$$

If we are addressing even higher  $r$ , i.e  $r > 2$ , our eigenvalue problem has no such simple solution. In this case we have to find the roots of the characteristic polynomial of the eigenvalue problem, where the polynomial reads as

$$0 = \chi(b_r) = \det[\mathcal{G}_{\hat{K}} - b_r \mathcal{G}_1]. \quad (5.34)$$

Deriving the minimal or maximal root  $b_r$  of the polynomial (5.34) and choosing arbitrary  $\alpha_1, \dots, \alpha_r$ , we receive the value of  $b'_r$  or  $b_r$  respectively.

Now that we have a numerically solvable equation in dependence of the operator  $\hat{K}$ , we can concern ourself with the numerical implementation in order to determine the values  $b'_r$  or  $b_r$ .

### 5.2.1. General numerical implementation

The aimed for, general numerical implementation of Eq. (5.34) is obtained by the two-step straightforward approach:

- (i) calculate the minimal or maximal root of  $\chi(b_r)$ ,
- (ii) minimize/maximize this root over the amplitudes  $(\alpha_1, \dots, \alpha_r) \in \mathbb{C}^r$ .

This numerical implementation is not restricted to a specific operator  $\hat{K}$ . Hence, we can now construct the bounds  $b'_r$  and  $b_r$  for any measurable observable  $\hat{K}$ . The experimental outcome is the expectation value  $\langle \hat{K} \rangle$ . We can compare this quantity with the bound,  $b'_r$  or  $b_r$ , for the degree of nonclassicality  $r$ , cf. Eqs. (5.7) and (5.16).

Here we want to give one very intuitive example for the calculation of the bounds  $b'_r$  for various  $r$ . We consider an operator  $\hat{K}$ , which is based on the quadrature variance, namely  $\hat{K} = [\Delta\hat{x}(\phi)]^2$ . Because of the transformation properties [4], we can restrict our considerations, without loss of generality, to the operator

$$\hat{K} = \hat{x}(0)^2 = (\hat{a} + \hat{a}^\dagger)^2 = 2\hat{a}^\dagger\hat{a} + \hat{a}^2 + \hat{a}^{\dagger 2} + \hat{1}. \quad (5.35)$$

The numerical results for the boundaries  $b'_r$  are listed in Table 5.1 together with the corresponding squeezing values up to  $r = 5$ . Whenever a squeezing value exceeds a bound, we have certified the degree of nonclassicality to be greater than  $r$ . For example, if we are measuring -6.5 dB squeezing, we have certified the degree of nonclassicality to be  $r = 3$ . Note that in [4] we considered boundaries up to  $r = 9$  as the squeezing world record was -12.7 dB [ESB10], yielding a degree of nonclassicality of  $r = 8$ . This value was beaten by the same authors just in 2016 and now the new squeezing world record is -15 dB [VMDS16], which corresponds to a degree of nonclassicality of  $r = 10$ .

$r$	$b'_r(\hat{K})$	squeezing
1	1.000000	0.00 dB
2	0.443071	-3.5 dB
3	0.256447	-5.9 dB
4	0.169295	-7.7 dB
5	0.121006	-9.2 dB
$\vdots$	$\vdots$	$\vdots$
$\infty$	0	$\infty$

**Table 5.1.:** The calculated boundaries  $b'_r(\hat{K})$  for states in  $\mathcal{M}_r$  of the observable  $\hat{K} = [\Delta\hat{x}(\varphi)]^2$  are listed. Whenever the experimentally realized squeezing power exceeds the squeezing bounds, we have certified the degree of nonclassicality to be greater than  $r$ , i.e.  $D_{\text{Ncl}}(\hat{\rho}) > r$ .

### 5.2.2. Optimal witness for pure states

In this section, we want to address the formulation of an optimal witness for pure states. For this reason, we modify our approach to check whether a pure state is of a particular degree of nonclassicality and, therefore, in a specific set of pure states  $\mathcal{S}_r$  or not. In particular, we compute the distance  $d_r$

$$d_r = \text{Tr} \left( |\psi\rangle \langle\psi| - \frac{|\psi_r\rangle \langle\psi_r|}{\langle\psi_r|\psi_r\rangle} \right)^2 \rightarrow \min, \quad (5.36)$$

of our investigated state  $|\psi\rangle$  to the set  $\mathcal{S}_r$  with the coherent superposition state  $|\psi_r\rangle$  of a known degree of nonclassicality  $r$ . By taking the normalizations into account we arrive at

$$\begin{aligned} d_r &= 2 \left[ 1 - \frac{\langle\psi_r|(|\psi\rangle \langle\psi|)|\psi_r\rangle}{\langle\psi_r|\psi_r\rangle} \right] \\ &= 2[1 - b_r], \end{aligned} \quad (5.37)$$

from which we can directly derive a proper operator,  $\hat{K} = |\psi\rangle \langle\psi|$ . This relates to the parameter  $b_r$  and, therefore, to the definition of the degree of nonclassicality, cf. Eq. (5.4)–(5.6), as follows: if  $b_r(\hat{K}) = 1$  then  $d_r = 0$  and the pure state  $|\psi\rangle \langle\psi|$  lies in  $\mathcal{S}_r$ , cf. Eq. (5.4). If  $b_r(\hat{K}) < 1$ , then  $d_r > 0$  and the state  $|\psi\rangle \langle\psi|$  does not lie in  $\mathcal{S}_r$ , cf. Eq. (5.5). The combination of these two facts leads directly to the optimal, necessary and sufficient witness for arbitrary pure states,

$$\hat{W}_r = b_r(|\psi\rangle \langle\psi|)\hat{1} - |\psi\rangle \langle\psi|. \quad (5.38)$$

Now that we found the optimal witness for pure states, we can move on to compute  $b_r(\hat{K}) = b_r(|\psi\rangle \langle\psi|)$ . Thus we need to solve the equation

$$\mathcal{G}_{|\psi\rangle \langle\psi|} \Lambda = b_r \mathcal{G}_{\hat{1}} \Lambda, \quad (5.39)$$

cf. Eq. (5.24). As  $\mathcal{G}_{|\psi\rangle\langle\psi|} = g_{|\psi\rangle} g_{|\psi\rangle}^\dagger$ , with  $g_{|\psi\rangle} = (\langle\alpha_k|\psi\rangle)_{k=1}^r$ , is a rank 1 operator, the maximal solution reads

$$\Lambda = \mathcal{G}_{\hat{1}}^{-1} g_{|\psi\rangle} \quad (5.40)$$

and

$$b_r = g_{|\psi\rangle}^\dagger \mathcal{G}_{\hat{1}}^{-1} g_{|\psi\rangle}. \quad (5.41)$$

With this result, we can now apply our method to examples to estimate the degree of nonclassicality of different pure quantum state using the optimal witness.

### 5.2.3. Infinite superposition states

Let us focus on the general case of infinite superposition states in the Fock basis expansion,

$$|\psi\rangle = \sum_{n=0}^{\infty} \frac{\psi_n}{\sqrt{n!}} \hat{a}^{\dagger n} |0\rangle \quad (5.42)$$

for the rank 1 operator  $\hat{K} = |\psi\rangle\langle\psi|$ . The quantum states we want to investigate here exemplarily are the squeezed vacuum states. Because they have many applications on the one hand and, on the other hand, are easily accessible in our lab. For the investigation of the squeezed vacuum states we, use in Eq. (5.42):

$$\text{for even } n : \psi_n = \frac{1}{\sqrt{\mu}} \left( -\frac{\nu}{2\mu} \right)^{n/2} \frac{\sqrt{n!}}{(n/2)!}, \quad (5.43)$$

$$\text{for odd } n : \psi_n = 0, \quad (5.44)$$

resulting in the in Sec. 2.2.3 introduced form of the squeezed vacuum state,

$$|\psi\rangle = |\xi, 0\rangle = \frac{1}{\sqrt{\mu}} \exp\left(-\frac{\nu}{2\mu} \hat{a}^{\dagger 2}\right) |0\rangle, \quad (5.45)$$

where  $\mu = \cosh(|\xi|)$  and  $\nu = e^{i\phi_\xi} \sinh(|\xi|)$ , see also Sec. 2.2.3.

Now we are looking at the overlap of the squeezed vacuum states with three different sets  $\mathcal{S}_r$  for  $r = 1, 2, 3$ , using the definition of the inner product of the coherent state and

the squeezed vacuum state, see [VW06],

$$\langle \alpha | \xi, 0 \rangle = \frac{e^{-|\alpha|^2/2 - \nu \alpha^*/2\mu}}{\sqrt{\mu}}. \quad (5.46)$$

We compute the bounds  $b_r$  in Eq. (5.41) for  $r = 1, 2, 3$  depending on the squeezing parameter  $\xi$ . The results are displayed in Fig. 5.2, where the black line corresponds to the bound  $b_r$  for  $r = 1$ , the blue line for  $r = 2$  and the blue line for  $r = 3$ . This bounds means that whenever we exceed the value  $b_r(\xi)$ , we have successfully proven that the degree of nonclassicality  $D_{Ncl}(|\psi\rangle\langle\psi|) > r$ . Furthermore, this figure indicates that no finite  $r$  and  $|\xi| > 0$  gives the value  $b_r = 1$ , cf. [GSV12]. Therefore the amount of nonclassicality of a squeezed vacuum state is infinite, independent of the amount of squeezing. However, what we can also learn is that the higher the amount of squeezing is, the harder it becomes to exceed the bounds  $b_r$ . It is, at least from the experimental point of view, intuitive that with an increasing squeezing, we have an increasing verifiable degree of nonclassicality. What we expect to see in an experiment is that, due to statistical fluctuations and finite measuring time, we can certify a certain degree of nonclassicality that increases with the squeezing strength. This, however, still needs to be verified.

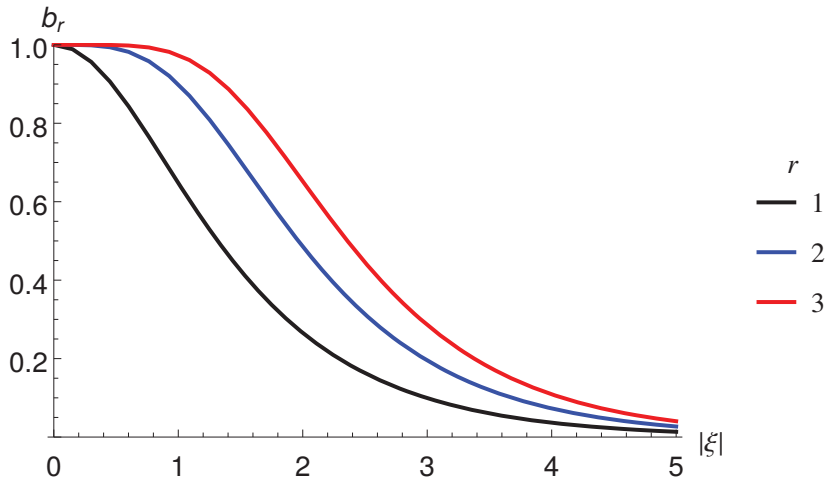


**Figure 5.2.:** The maximal bounds  $b_r = b_r(|\psi\rangle\langle\psi|)$  (black line  $r = 1$ , blue line  $r = 2$  and red line  $r = 3$ ) for the squeezed vacuum state  $|\psi\rangle = |\xi, 0\rangle$  is shown in dependence of the squeezing parameter  $|\xi|$ . We can state that a stronger squeezing, hence a larger  $|\xi|$ , yields a smaller bound  $b_r$  to be violated to verify a degree of nonclassicality above  $r$ . Further, we find that with increasing  $r$ , the range of values  $|\xi|$  for which the bound  $b_r = 1$  becomes wider.

### 5.3. Multimode Nonclassicality

For the sake of completeness, we want to address here the issue of witnessing a multimode degree of nonclassicality. Therefore, we define the  $N$ -mode degree of nonclassicality of pure states  $D_{Ncl}(|\psi_{r,N}\rangle \langle \psi_{r,n}|) = r$  as the number of superpositions of multimode coherent states,

$$|\psi_{r,N}\rangle = \sum_{j=1}^r \lambda_j |\alpha_j\rangle \in \mathcal{S}_{r,N}, \quad (5.47)$$

with  $\lambda_j \in \mathbb{C} \setminus \{0\}$  and the coherent amplitudes  $\alpha_j \in \mathbb{C}^N$  ( $\alpha_j \neq \alpha_{j'}$  for  $j \neq j'$ ). Similarly to the single mode approach, a convex roof construction yields a proper multimode nonclassicality measure for mixed states

$$\mathcal{M}_{r,N} = \overline{\text{conv}\{|\psi_{r,N}\rangle \langle \psi_{r,n}| : |\psi_{r,n}\rangle \in \mathcal{S}_{r,N}\}}. \quad (5.48)$$

Note that this notion of the degree of nonclassicality is invariant under classical mode transformations,

$$\hat{a}'_n = \sum_{n'}^N U_{n,n'} \hat{a}_{n'} \quad (5.49)$$

for  $n = 1, \dots, N$  and a unitary matrix  $\mathcal{U} = (U_{n,n'})_{n,n'=1}^N$ , whereas this transformation maps the coherent amplitudes as  $\alpha'_j = \mathcal{U}\alpha_j$ . Therefore the structure of Eq. (5.47) remains unchanged and we have in particular  $r' = r$ , with  $r'$  being the degree of nonclassicality in the transformed basis.

Now let us consider the  $N$ -mode witness construction, cf. Eq. (5.9), from multimode Hermitian operators  $\hat{K}$ :

$$\hat{W}_{r,N} = b_{r,N}(\hat{K})\hat{1} - \hat{K}, \quad (5.50)$$

with

$$b_{r,N} = \sup_{|\psi_{r,N}\rangle \in \mathcal{S}_{r,N}} \frac{\langle \psi_{r,N} | \hat{K} | \psi_{r,N} \rangle}{\langle \psi_{r,N} | \psi_{r,N} \rangle}. \quad (5.51)$$

Analogously to Eq. (5.15), we find

$$\hat{W}'_{r,N} = \hat{K} - b'_{r,N}(\hat{K})\hat{1}, \quad (5.52)$$

with

$$b'_{r,N} = \inf_{|\psi_{r,N}\rangle \in \mathcal{S}_{r,N}} \frac{\langle \psi_{r,N} | \hat{K} | \psi_{r,N} \rangle}{\langle \psi_{r,N} | \psi_{r,N} \rangle}. \quad (5.53)$$

The bounds  $b_{r,N}(\hat{K})$  and  $b'_{r,N}(\hat{K})$  are the least upper and smallest lower bound of the eigenvalues  $b_{r,N}$  of

$$\mathcal{G}_{\hat{K}}\Lambda = b_{r,N}\mathcal{G}_{\hat{1}}\Lambda. \quad (5.54)$$

As this multimode approach is similar to the single-mode one, we end up with similar eigenvalue problems, cf. Eq. (5.24) and (5.54), we can solve this multimode problem in the same way as we did in the single-mode case, and, therefore, also the numerical implementation can be generalized in a straightforward manner.

## 5.4. Witnessing using pattern functions

All theoretical derivations and examples shown so far were published in [4]. In these considerations, we already gave an experimentally accessible witness using the quadrature variances. This approach however, only uses the property of squeezing to quantify the nonclassicality of the quantum state. This section now considers a more general idea to quantify the nonclassicality of arbitrary quantum states using the quadrature data gained in a QST, cf. Sec. 3.7. For this purpose, we introduce pattern functions in coherent state basis, cf. [Leo97, LPD95], in order to reconstruct the density matrix of our measured quantum state. As the resulting density matrix is already in coherent state basis, we may use it to quantify the amount of nonclassicality. The first numerical implementation of these pattern functions in coherent state basis in our group, was done during the Master project of Hannes Sobottka [Sob14], supervised by myself. His Matlab-code, was used, including some minor modifications, for the following investigations.

### 5.4.1. Pattern functions in coherent state basis

The derivation of the pattern functions in coherent state basis presented here resembles the explanations in [Leo97, LPD95, Sob14] to some extend.

The reconstruction of the density matrix via pattern functions is a sampling approach, where the idea is to construct sampling functions  $(\mathcal{F}_{\alpha'\alpha}(q, \theta))$  that resemble the generalized quadrature distributions of the projector  $|\alpha\rangle\langle\alpha'|$ . Note that these sampling functions can be derived in any chosen basis, whereas we are restricting the discussion here to the coherent state basis. For a wider discussion of the general derivation of these sampling functions, please refer to [Leo97, LPD95]. The sampling functions  $\mathcal{F}_{\alpha'\alpha}$  detect the patterns of the generalized quadrature distribution in the measured quadrature distribution  $\text{pr}(q, \theta)$ , reasoning the notation they are also called *pattern functions*. The pattern functions connect the experimental data via

$$\rho_{\alpha'\alpha} = \langle\langle\mathcal{F}_{\alpha'\alpha}(q, \theta)\rangle\rangle_{q, \theta}, \quad (5.55)$$

where the double bracket denotes the statistical averaging of the pattern function with respect to  $q$  and  $\theta$ , from the measured quadrature distribution. Here, for every pair  $(q, \theta)$  one pattern function is calculated and averaged, successively building up the matrix  $\rho_{\alpha'\alpha}$ .

In general, the density matrix in coherent state basis reads as

$$\rho_{\alpha'\alpha} = \langle\alpha'|\hat{\rho}|\alpha\rangle, \quad (5.56)$$

where  $\hat{\rho}$  is the density operator of the state under study. In order to derive the pattern functions in coherent state basis, we start with the generalized quadrature distribution  $\text{pr}_{\alpha'\alpha}(x, \theta)$

$$\text{pr}_{\alpha'\alpha}(x, \theta) = \langle x|\hat{U}(\theta)|\alpha\rangle\langle\alpha'|\hat{U}^\dagger(\theta)|x\rangle, \quad (5.57)$$

where  $\hat{U}(\theta) \equiv \exp(-i\theta\hat{n})$  is the phase-shift operator, with the property  $\hat{U}(\theta)|\alpha\rangle = |\alpha\exp(-i\theta)\rangle$  and, therefore,

$$\text{pr}_{\alpha'\alpha}(x, \theta) = \langle x|\alpha\exp(-i\theta)\rangle\langle\alpha'\exp(-i\theta)|x\rangle. \quad (5.58)$$

Note while we were trying to reproduce the pattern functions, we encountered an issue concerning the inner product of two coherent states. This is due to a different definition

of the inner product of two coherent states. Leonhardt, [Leo97], uses the relation

$$\begin{aligned}\langle\beta|\alpha\rangle &= \exp\left[-\frac{1}{2}|\alpha-\beta|^2\right] \\ &= \exp\left[-\frac{|\beta|^2}{2}-\frac{|\alpha|^2}{2}+\beta^*\alpha+\beta\alpha^*\right].\end{aligned}\quad (5.59)$$

That this, however, is not correct is easily shown by starting the calculation with the definition of the coherent states, cf. Eq. (2.10),

$$|\alpha\rangle = e^{-|\alpha|^2/2} \sum_{n=0}^{\infty} \frac{\alpha^n}{\sqrt{n!}} |n\rangle \quad (5.60)$$

and, therefore, the inner product reads

$$\begin{aligned}\langle\beta|\alpha\rangle &= e^{-|\beta|^2/2} e^{-|\alpha|^2/2} \sum_{n,m=0}^{\infty} \frac{\beta^{*n} \alpha^m}{\sqrt{n!m!}} \langle n|m\rangle \\ &= \exp\left[-\frac{|\beta|^2}{2}-\frac{|\alpha|^2}{2}+\beta^*\alpha\right],\end{aligned}\quad (5.61)$$

cf. [VW06]. The difference between Eq. (5.59) and (5.61) might seem to be negligible. Yet it results in a different, final pattern function. Hence, the pattern function we used in our further calculations are derived with the inner product as given in Eq. (5.61).

Let us recall to the derivation of the pattern function  $\mathcal{F}_{\alpha'\alpha}(q, \theta)$  and, therefore, continue with Eq. (5.58). By taking a closer look at the definitions of Eq. (5.58) and (2.10), we can directly see that we end up with the problem of the inner product of the Fock state  $n$  with the quadrature state  $x$  ( $\langle n|x\rangle$ ). This is however a well studied problem, cf. Sec. 3.4 [VW06]. Hence, the result of Eq. (5.58) is

$$\text{pr}_{\alpha'\alpha}(x, \theta) = \frac{1}{\sqrt{2\pi}} \exp\left[-\frac{1}{2}(x-x_\theta)^2 - \frac{|\alpha|^2}{2} - \frac{|\alpha'|^2}{2} + \alpha\alpha'^*\right], \quad (5.62)$$

where

$$x_\theta = (\alpha e^{-i\theta} + \alpha'^* e^{i\theta}). \quad (5.63)$$

The pattern function  $\mathcal{F}_{\alpha'\alpha}(q, \theta)$  is obtained from the generalized quadrature distribution as

$$\mathcal{F}_{\alpha'\alpha}(q, \theta) = -\frac{\mathcal{P}}{\pi} \int_{-\infty}^{\infty} \frac{\text{pr}_{\alpha'\alpha}(x, \theta)}{(q - x)^2} dx, \quad (5.64)$$

where  $\mathcal{P}$  is Cauchy's principle value. If we now insert Eq. (5.62) into the equation above and use the general vacuum pattern-function

$$f_{00}(q) = -\mathcal{P} \int_{-\infty}^{\infty} \frac{\psi_0(x) \varphi_0(x)}{(q - x)^2} dx, \quad (5.65)$$

where  $\psi_0(x)$  and  $\varphi_0(x)$  are the regular and irregular wace functions respectively, cf. [Leo97], we find the pattern function in coherent state basis

$$\mathcal{F}_{\alpha'\alpha}(q, \theta) = \frac{1}{\pi} \cdot f_{00}(q - x_\theta) \cdot \exp \left[ \frac{1}{2} \left( -|\alpha|^2 - |\alpha'|^2 + 2\alpha\alpha'^* \right) \right]. \quad (5.66)$$

With this final result, we can now sample the density matrices of arbitrary quantum states in coherent state basis as long as we have the quadrature data. The numerical implementation was done, following the steps in [LMK96], and is not discussed in detail here. Note that we are actually dealing with four-dimensional density matrices, as the complex amplitudes  $\alpha = \text{Re}(\alpha) + i \cdot \text{Im}(\alpha)$  and  $\alpha' = \text{Re}(\alpha') + i \cdot \text{Im}(\alpha')$  each contain a real and an imaginary part. Furthermore, each entry of the four-dimensional matrix is a complex number. Hence, we needed to figure out a graphical representation, which is shown and discussed below.

### 5.4.2. Application to simulated data

In the following, we are going to present reconstructed density matrices for different simulated<sup>1</sup> and one experimentally recorded quantum state. We are starting with a vacuum state, before we proceed with a coherent state with an arbitrarily complex amplitude  $\alpha$  in order to explain the structure of the resulting density matrices. In Sec. 5.4.3, we are going to use the reconstructed density matrix of a compass state, being composed out of four coherent states, to find a general method to estimate the degree of nonclassicality. The compass state is considered, since we are aiming to decompose the investigated state into superpositions of coherent states and by starting with an example with known

<sup>1</sup>For details on the simulation see App. D

number of superpositions, we hope to find a reasonable way to witness the degree of nonclassicality in general. Finally, we are going to inspect squeezed vacuum states for two different squeezing strengths from simulation along with an experimentally generated squeezed vacuum state.

Note that most of the presented results are obtained from simulations, but as we simulate quadrature data in the form we would also obtain from BHD, and hence the method is similarly applicable to experimental data. We present this application for one specific, experimentally generated and measured squeezed vacuum state. Furthermore, all density matrices are normalized to  $\text{tr}[\rho_{\alpha'\alpha}] = 1$ . When we are considering a density matrix in coherent state basis, we are using the same types of plots. Hence, they will be explained in greater detail only for the vacuum state.

### Vacuum state

Let us start with the density matrix in coherent state basis  $\rho_{\alpha'\alpha}$  for the simple and intuitive example of a vacuum state  $|0\rangle$ .

In Fig. 5.3 we show the modulus of the reconstructed density matrix in coherent state basis for the vacuum state in 21x21 tiles. We chose to look at the modulus, in order to visualize the reconstructed density matrix elements in a convenient way. Nevertheless, we also paid attention to the real and imaginary parts of the density matrix and not only to the modulus<sup>2</sup>, in order to receive the full information for the nonclassicality quantification.

In each tile we vary the real, x-axis (left to right), and imaginary, y-axis (bottom to top), part of the complex amplitude  $\alpha$  from -5 to 5. Within each tile, we are looking at a different real and imaginary part combination of  $\alpha'$ . The real part of  $\alpha'$  is varied along the x-direction (left to right) from -5 to 5, so is the imaginary part of  $\alpha'$  in y-direction (bottom to top).

By looking at the Fig. 5.3, we can stress that we have a global structure over all tiles, as well as a local structure in each tile. Both the global and the local structure are symmetric around the central tile. The global structure is a circular structure that is centrosymmetric around the central tile ( $\text{Re}(\alpha') = \text{Im}(\alpha') = 0$ ) with a maximum at that center. This seems reasonable, as the vacuum state is also centrosymmetric in phase space around the center ( $\text{Re}(\alpha') = \text{Im}(\alpha') = 0$ ). The local structure in each tile strongly depends on the tile we are looking at. The further away the tile is from the center, the

<sup>2</sup>See App. C for examples.

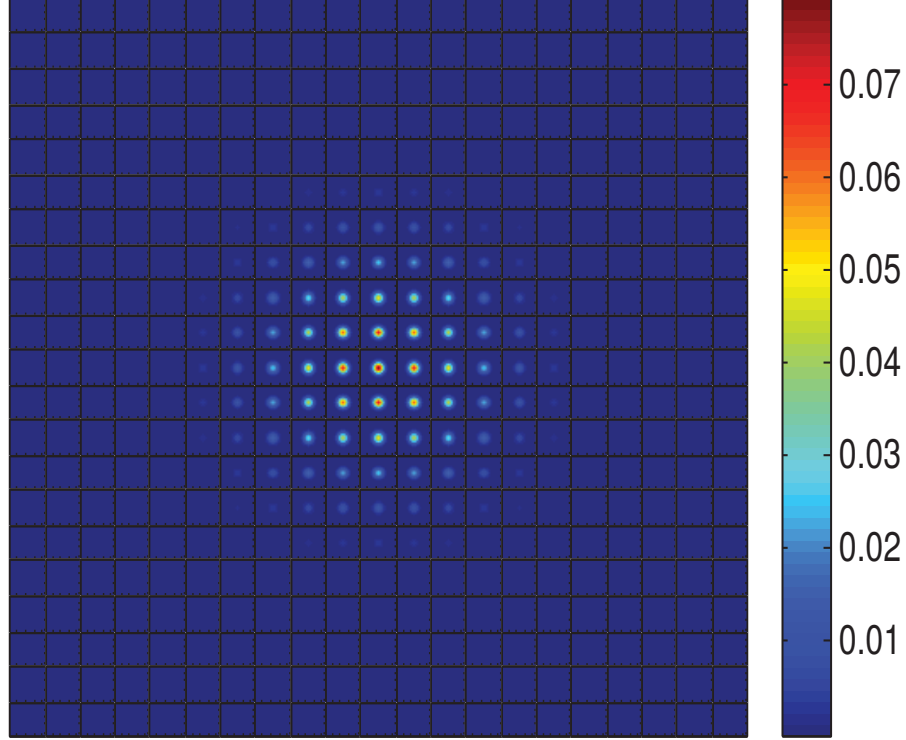


**Figure 5.3.:** Contour plot of the modulus of the reconstructed density matrix in coherent state basis  $\rho_{\alpha'\alpha}$  for a vacuum state. In each tiles we vary the real, x-axis (left to right), and imaginary, y-axis (bottom to top), part of  $\alpha$  from  $-5$  to  $5$ . Each individual tile concerns a different combination of real, along x-direction (left to right), and imaginary, along y-direction (bottom to top), part of  $\alpha'$ , also from  $-5$  to  $5$  in discrete steps. As this figure is supposed to give qualitative information about the state, we neglect the axes labeling to keep the figure clearer.

smaller is the corresponding density matrix element. Closer to the center, the structure is getting more significant, i.e., we see a circular structure with a maximum at the center. In order to take a closer look at the local structure, we consider the tile with the highest density matrix element and plot that tile as a surface plot, see Fig. 5.4. For the vacuum state, we see a Gaussian shape with its center at  $\text{Re}(\alpha') = \text{Im}(\alpha') = 0$ . This again seems reasonable, because of the vacuum state being centrosymmetric in phase space<sup>3</sup>.

<sup>3</sup>Note that for  $\alpha = \alpha'$  we can even compute the  $Q$ -function of the reconstructed density matrix.

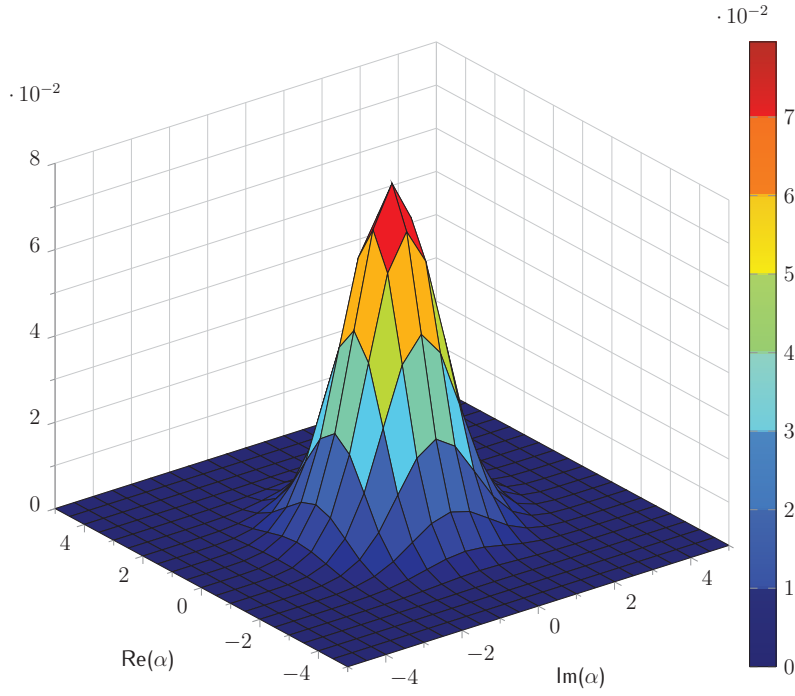


Figure 5.4.: Central tile of Fig. 5.3 (vacuum state) as surface plot.

### Coherent state

Now, we extend our considerations to coherent states, in particular the randomly chosen example of  $|\beta\rangle = |3 + i \cdot 0\rangle$ . Note that, by definition, the coherent state is a displaced vacuum state with the displacement  $\beta$ . Here, we use  $\beta$  to denote the input coherent amplitude of the simulation, whereas  $\alpha$  and  $\alpha'$  correspond to the reconstruction of the density matrices in coherent state basis. In Fig. 5.5 we clearly see that not only the local structures inside the tiles are displaced, but also the global structure is shifted in the same direction as the local structure. The center of the global structure now lies, as expected, around the tile with the real and imaginary part of  $\alpha'$ :  $\text{Re}(\alpha') = 3$  and  $\text{Im}(\alpha') = 0$ , cf. Fig. 5.5, so does the local structure in each tile, cf. e.g. Fig. 5.6.

#### 5.4.3. $\rho_{\alpha'\alpha}$ in the witnessing approach

The idea of using the density matrix in coherent state basis in the witnessing approach, arises from the definition of the bound  $b_r$

$$b_r(\hat{K}) = \sup_{|\psi_r\rangle \in \mathcal{S}_r} \frac{\langle \psi_r | \hat{K} | \psi_r \rangle}{\langle \psi_r | \psi_r \rangle}, \quad (5.67)$$

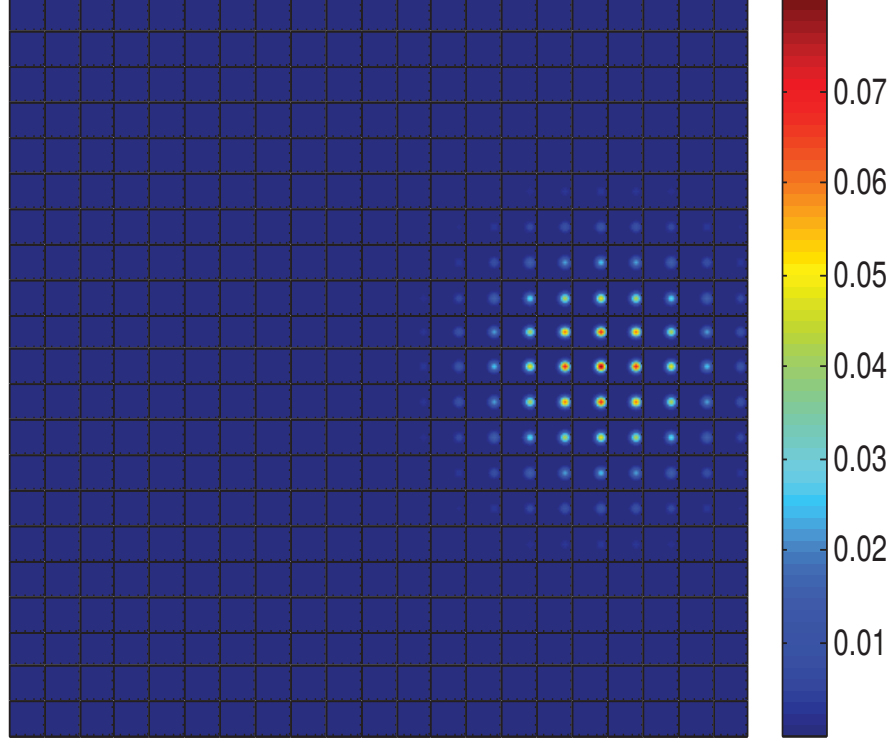


**Figure 5.5.:** Contour plot of the modulus of the reconstructed density matrix in coherent state basis  $\rho_{\alpha'\alpha}$  for a coherent state with  $\hat{\rho} = |\beta\rangle\langle\beta| = |3 + i \cdot 0\rangle\langle 3 + i \cdot 0|$ .

cf. Eq. (5.8), where  $|\psi_r\rangle = \sum_{k=1}^r \lambda_k |\alpha_k\rangle$ . Hence, what we are looking at is

$$b_r(\hat{K}) = \sup_{|\psi_r\rangle \in \mathcal{S}_r} \frac{\sum_{k,l=1}^r \lambda_k^* \lambda_l \langle \alpha_k | \hat{K} | \alpha_l \rangle}{\sum_{k,l=1}^r \lambda_k^* \lambda_l \langle \alpha_k | \alpha_l \rangle}, \quad (5.68)$$

where the numerator contains the matrix  $(\langle \alpha_k | \hat{K} | \alpha_l \rangle)_{k,l=1}^r$ . In case we choose the state itself as witness operator, i.e.  $\hat{K} = \hat{\rho}$ , the matrix  $(\langle \alpha_k | \hat{K} | \alpha_l \rangle)_{k,l=1}^r$  is our reconstructed density matrix in coherent state basis  $\rho_{\alpha',\alpha}$ . Therefore, we are trying to use these reconstructed density matrices in our witnessing approach, as they are experimentally accessible for arbitrary quantum states.

### Compass state with $R=4$

Let us turn to a rather complex, but still intuitive example: the compass state for  $R=4$  (see Eq. (2.16)). This is the first example of which we want to estimate the degree of nonclassicality, using the density matrix in coherent state basis. Due to the definition of

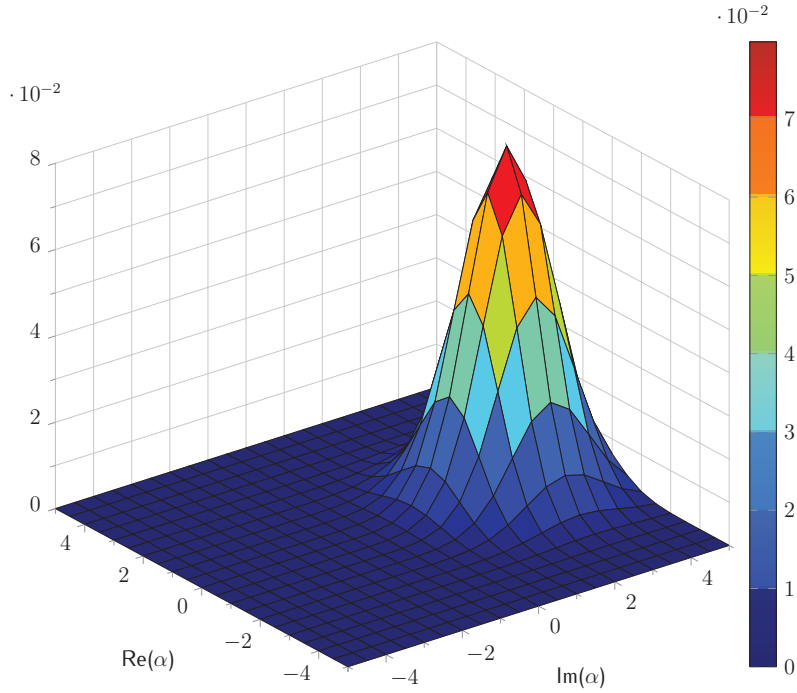


Figure 5.6.: The tile  $\text{Re}(\alpha') = 3$  and  $\text{Im}(\alpha') = 0$  of Fig. 5.5 (coherent state) as surface plot.

the compass state we know the correct degree of nonclassicality of this state. Therefore, we can probe whether our approach gives the correct results.

First, we simulate a compass state with  $R=4$ ,

$$|\beta_4\rangle = N_4(|\beta\rangle + |-\beta\rangle + |i\beta\rangle + |-i\beta\rangle), \quad (5.69)$$

where we choose  $\beta = 3 + i \cdot 0$ . The reconstructed density matrix  $\rho_{\alpha',\alpha}$  of the compass state  $|\beta_4\rangle$  is shown as a contour plot of the modulus of  $\rho_{\alpha',\alpha}$  in Fig. 5.7. The global structure is already much more complex than the one of the coherent state. Even though, the global structure is still centrosymmetric, it is no longer circular. The density matrix seems to be quartered on the four main diagonals and by looking at the real and imaginary parts of the density matrix, cf. App. C, we can see interference fringes arise from the superposition of the coherent states. Furthermore, we see this quartered structure in each tile, cf. Fig. 5.8.

Now we want to compare different superpositions of coherent states, with our simulated compass state. For this reason, we simulate a variation of test states. In the following, we will denote the density matrices of these test states as  $\sigma_{\alpha',\alpha}$ . We compare the density matrix of the simulated compass state  $\rho_{\alpha',\alpha}$  with those of the test states. In

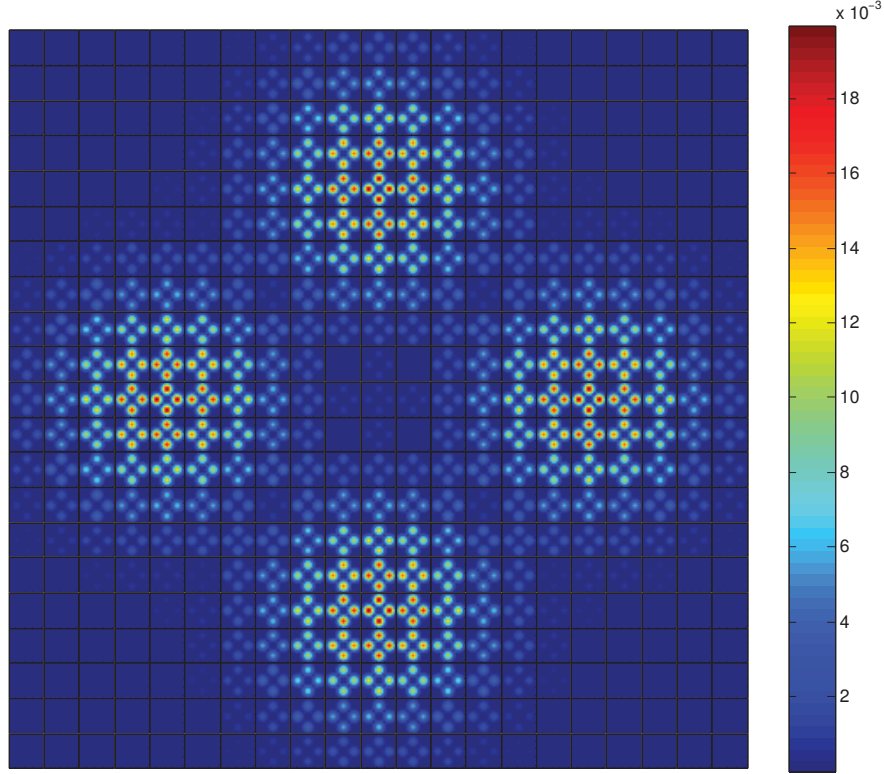


**Figure 5.7.:** Contour plot of the modulus of the reconstructed density matrix in coherent state basis  $\rho_{\alpha'\alpha}$  for the compass state  $|\beta_4\rangle$ .

order to quantify the closeness of the two density matrices, we introduce the Euclidean distance, cf. [DD09], between the two density matrices

$$\mathcal{D}(\rho_{\alpha',\alpha}, \sigma_{\alpha',\alpha}) = \sqrt{\sum_{\alpha',\alpha} |\rho_{\alpha',\alpha} - \sigma_{\alpha',\alpha}|^2}. \quad (5.70)$$

The closer this value approaches 0, the closer we are to our optimal decomposition. Note that this distance measure only indicates whether or not we are close to the correct decomposition, but does not quantify the quality of the decomposition.

The test states we are going to use here have similar structures. They are composed out of three, four or five coherent states, each with the same absolute displacement from the vacuum, but with a phase rotation  $\exp((2\pi i k)/R)$ , where  $R$  is the number of superpositions of coherent states and  $k = 0, \dots, R-1$ , cf. Eq. (2.16). These states will be referred to as  $\mathcal{T}_{r,\beta}$ , where  $r$  is the number of coherent states we use and  $\beta$  is the coherent amplitude of the displacement of each states to the vacuum. In order to reduce

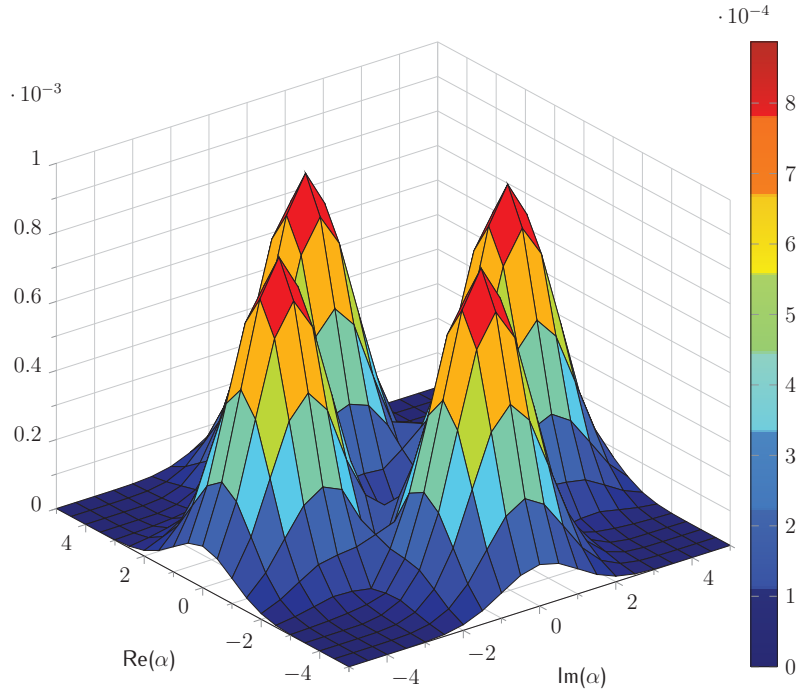


Figure 5.8.: Central tile of Fig. 5.7 as surface plot.

the number of test states, we chose the parameters  $\lambda_k$ , see Eq. (5.1), equal to one. All the computed distances for the different test states are listed in the Tab. 5.2. Here, we will consider two examples in greater detail.

First of all, we consider the test state  $\mathcal{T}_{3,3}$ , that is obviously not optimal, as this test state is composed out of three coherent states, cf. Fig. 5.9. The global structure of Fig. 5.9 is clearly not similar to the global structure of our investigated state in Fig. 5.7, which already indicates, that the test state is not optimal. The distance is  $\mathcal{D}(\rho_{\alpha'\alpha}(|\beta_4\rangle\langle\beta_4|), \sigma_{\alpha'\alpha}(\mathcal{T}_{3,3})) = 1.3709$ , which is clearly not equal to 0 and, therefore, the test state  $\mathcal{T}_{3,3}$  is not the optimal decomposition of the compass state  $|\beta_4\rangle\langle\beta_4|$ .

Next we are concerning a test state that is composed out of four coherent states  $\mathcal{T}_{4,3}$ , cf. Fig. 5.10. To be more specific, we are using the same  $\beta$  we used in the simulation of the compass state. The resulting density matrix of this test state is shown in Fig. 5.10. The global structure of this density matrix already resembles the one in Fig. 5.7. To quantify the closeness of the two density matrices, we compute again the distance  $\mathcal{D}(\rho_{\alpha'\alpha}(|\beta_4\rangle\langle\beta_4|), \sigma_{\alpha'\alpha}(\mathcal{T}_{4,3})) = 7.2058 \cdot 10^{-5}$ , which is very close to 0. This distance is the smallest distance between our simulated and reconstructed density matrix  $\rho_{\alpha',\alpha}$  and any of the used test states. Hence, we can conclude that the test state  $\sigma_{\alpha'\alpha}(\mathcal{T}_{4,3})$  is the one closest to the density matrix  $\rho_{\alpha',\alpha}$  of our simulated compass state.

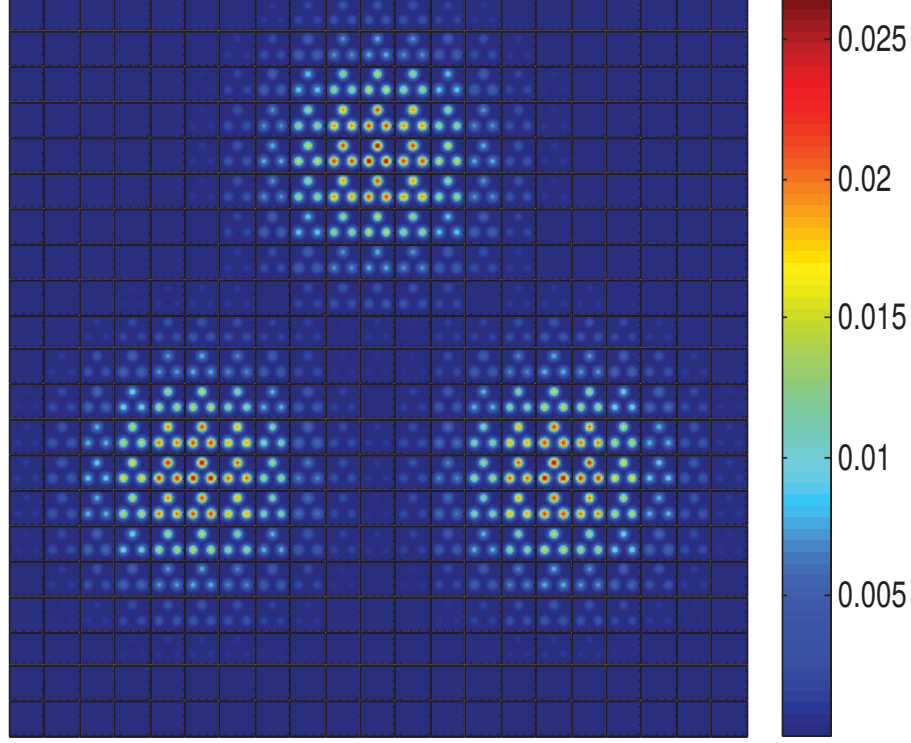
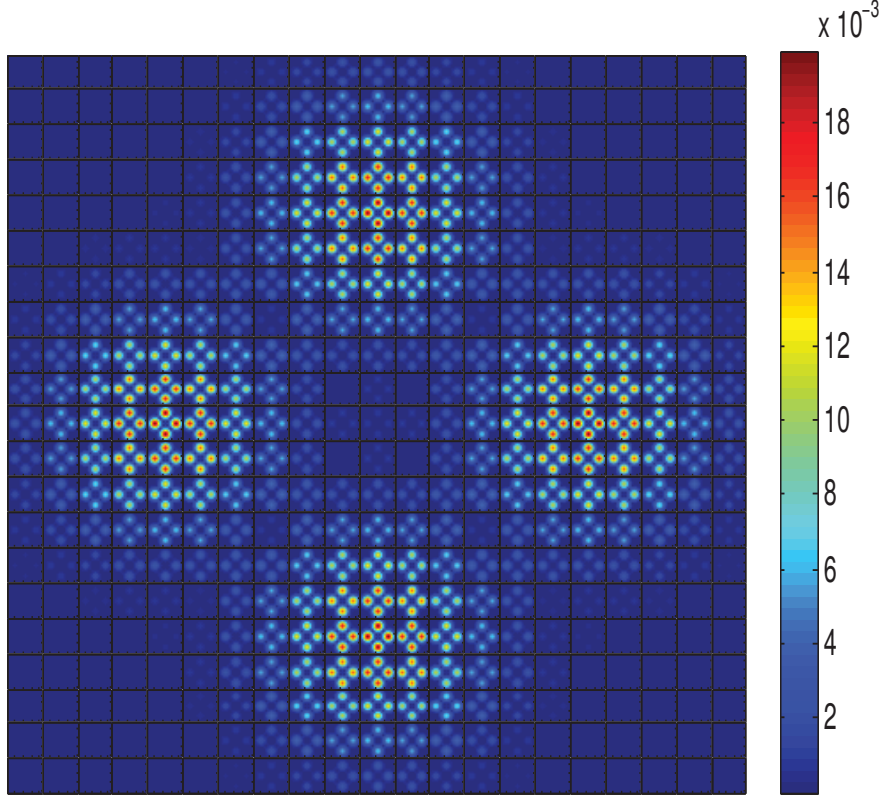


Figure 5.9.: Contour plot of the modulus of the reconstructed density matrix in coherent state basis  $\sigma_{\alpha'\alpha}(\mathcal{T}(3,3))$  for the compass state  $|\beta_4\rangle$ .

$\mathcal{D}(\rho_{\alpha'\alpha}( \beta_4\rangle\langle\beta_4 ), \sigma_{\alpha'\alpha}(\mathcal{T}_{3,1}))$	1.4157	$\mathcal{D}(\rho_{\alpha'\alpha}( \beta_4\rangle\langle\beta_4 ), \sigma_{\alpha'\alpha}(\mathcal{T}_{4,4}))$	1.1500
$\mathcal{D}(\rho_{\alpha'\alpha}( \beta_4\rangle\langle\beta_4 ), \sigma_{\alpha'\alpha}(\mathcal{T}_{3,2}))$	1.4155	$\mathcal{D}(\rho_{\alpha'\alpha}( \beta_4\rangle\langle\beta_4 ), \sigma_{\alpha'\alpha}(\mathcal{T}_{4,5}))$	1.6064
$\mathcal{D}(\rho_{\alpha'\alpha}( \beta_4\rangle\langle\beta_4 ), \sigma_{\alpha'\alpha}(\mathcal{T}_{3,3}))$	1.3709	$\mathcal{D}(\rho_{\alpha'\alpha}( \beta_4\rangle\langle\beta_4 ), \sigma_{\alpha'\alpha}(\mathcal{T}_{4,6}))$	1.8824
$\mathcal{D}(\rho_{\alpha'\alpha}( \beta_4\rangle\langle\beta_4 ), \sigma_{\alpha'\alpha}(\mathcal{T}_{3,4}))$	1.3925	$\mathcal{D}(\rho_{\alpha'\alpha}( \beta_4\rangle\langle\beta_4 ), \sigma_{\alpha'\alpha}(\mathcal{T}_{5,1}))$	1.4157
$\mathcal{D}(\rho_{\alpha'\alpha}( \beta_4\rangle\langle\beta_4 ), \sigma_{\alpha'\alpha}(\mathcal{T}_{3,5}))$	1.5246	$\mathcal{D}(\rho_{\alpha'\alpha}( \beta_4\rangle\langle\beta_4 ), \sigma_{\alpha'\alpha}(\mathcal{T}_{5,2}))$	1.4160
$\mathcal{D}(\rho_{\alpha'\alpha}( \beta_4\rangle\langle\beta_4 ), \sigma_{\alpha'\alpha}(\mathcal{T}_{3,6}))$	1.6989	$\mathcal{D}(\rho_{\alpha'\alpha}( \beta_4\rangle\langle\beta_4 ), \sigma_{\alpha'\alpha}(\mathcal{T}_{5,3}))$	1.4169
$\mathcal{D}(\rho_{\alpha'\alpha}( \beta_4\rangle\langle\beta_4 ), \sigma_{\alpha'\alpha}(\mathcal{T}_{4,1}))$	1.4091	$\mathcal{D}(\rho_{\alpha'\alpha}( \beta_4\rangle\langle\beta_4 ), \sigma_{\alpha'\alpha}(\mathcal{T}_{5,4}))$	1.4352
$\mathcal{D}(\rho_{\alpha'\alpha}( \beta_4\rangle\langle\beta_4 ), \sigma_{\alpha'\alpha}(\mathcal{T}_{4,2}))$	1.1144	$\mathcal{D}(\rho_{\alpha'\alpha}( \beta_4\rangle\langle\beta_4 ), \sigma_{\alpha'\alpha}(\mathcal{T}_{5,5}))$	1.5230
$\mathcal{D}(\rho_{\alpha'\alpha}( \beta_4\rangle\langle\beta_4 ), \sigma_{\alpha'\alpha}(\mathcal{T}_{4,3}))$	$7.2058 \cdot 10^{-5}$	$\mathcal{D}(\rho_{\alpha'\alpha}( \beta_4\rangle\langle\beta_4 ), \sigma_{\alpha'\alpha}(\mathcal{T}_{5,6}))$	1.6669

Table 5.2.: Distances between the compass state  $|\beta_4\rangle\langle\beta_4|$  and the test states  $\mathcal{T}_{n,\beta}$ .

The difficulty in finding the correct test state is the quite large number of parameters in the generation of the test state. Moreover, the more coherent states we used in the generation of the test state, the more parameters we need to optimize. In the above



**Figure 5.10.:** Contour plot of the modulus of the reconstructed density matrix in coherent state basis  $\sigma_{\alpha'\alpha}(\mathcal{T}(4,3))$  for the compass state  $|\beta_4\rangle$ .

example, we only used test states  $|\psi_r\rangle = \sum_{k=1}^r \lambda_k |\alpha_k\rangle$  with  $\lambda_k = 1 \forall k$  to reduce the number of parameters.

In order to determine the optimal decomposition, we would need to find an optimization algorithm that includes the parameters  $\lambda_k$ , the number of superpositions  $r$  in the test state, and the coherent displacements  $\beta$ . This algorithm then should find an optimal test state with  $\sigma_{\alpha'\alpha}(\mathcal{T}_{\text{opt}})$ , to reach a distance with the investigated quantum state  $\mathcal{D}(\rho_{\alpha'\alpha}, \sigma_{\alpha'\alpha}(\mathcal{T}_{\text{opt}})) \Rightarrow 0$ .

Note that so far, we were not able to connect the distance with the bound  $b_r$ , which we need in the witnessing approach. A direct connection is not possible, and we still need to find a way to compute the bound  $b_r$  for the optimal test state from our reconstruction. From the bound  $b_r$  we get the information, if we used the right number of superpositions to decompose our investigated state. Because  $b_r$  is smaller one if we used too few, larger one if we used too many, and equal one when we used the correct number of

superpositions. Still, the distance gives us enough information, when close to 0, to state that we are close to the right decomposition.

### Simulated squeezed vacuum states

Now that we indeed found an indicator for the closeness between two density matrices, we may consider a less obvious example, even though we cannot calculate the bound  $b_r$ . Still, we are able to make assumptions based on the distance between the investigated state and the test states. We choose to investigate two different squeezed vacuum states with two different squeezing strength, -3 dB and -10 dB respectively, denoted as  $\mathcal{SQ}_{S,\phi_\xi}$ , where  $S$  is the squeezing strength in dB and  $\phi_\xi$  the orientation in phase space.

The reconstructed density matrices for -3 dB and -10 dB are displayed in Fig. 5.11 and 5.12 respectively. They clearly display an ellipsoidal structure, locally as well as globally. Furthermore, we also see that for a higher squeezing strength the local and global structure is flattening.

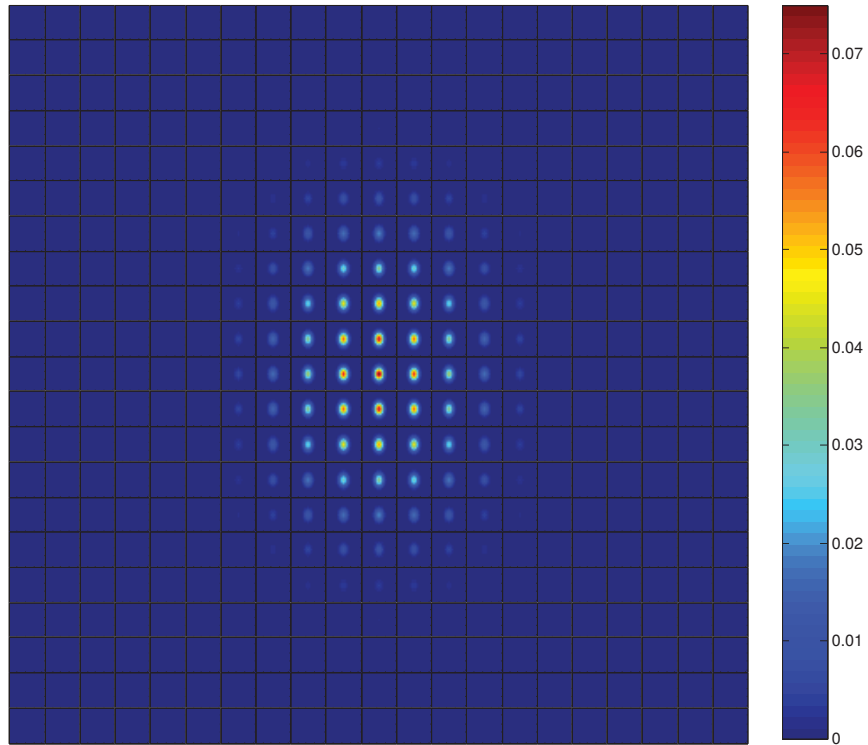


**Figure 5.11.:** Contour plot of the modulus of the reconstructed density matrix in coherent state basis  $\rho_{\alpha'\alpha}$  for a squeezed state with -3 dB squeezing.

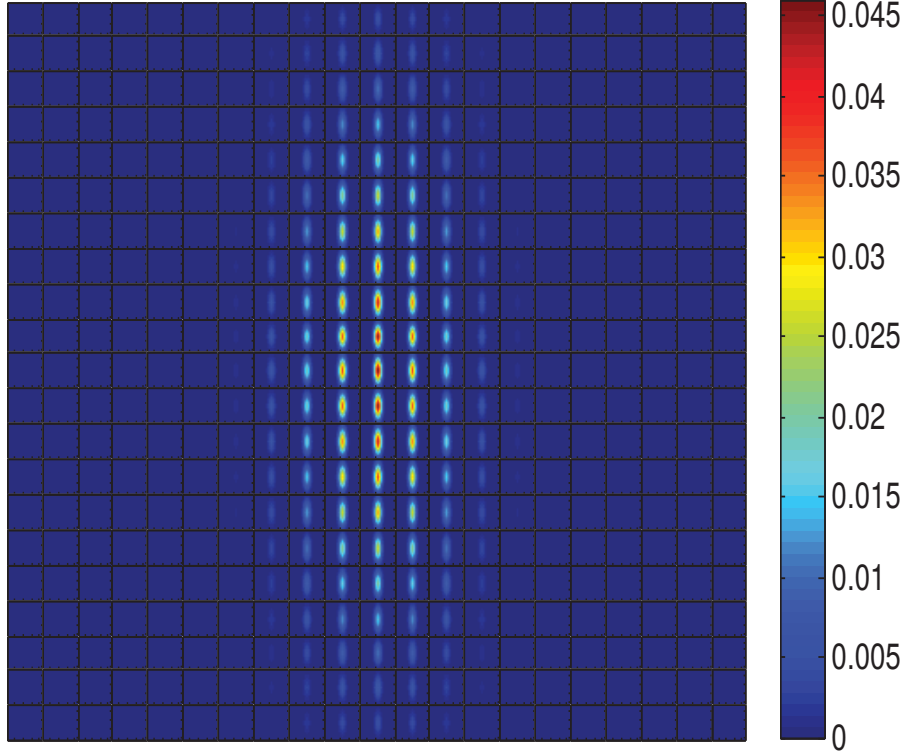


**Figure 5.12.:** Contour plot of the modulus of the reconstructed density matrix in coherent state basis  $\rho_{\alpha'\alpha}$  for a squeezed state with -10 dB squeezing.

Now we want to compare our squeezed states with different test states and compute the distances between the squeezed states and test states. As mentioned before, the degree of nonclassicality of squeezed states is infinity, but we expect, due to finite measuring time and statistical fluctuations, that we will need more superpositions of coherent states the stronger the squeezing is. Hence, we want to use test states with a different number of coherent states, to analyze whether or not we can see this behavior. Due to the huge number of possible test states we restricted them to three ( $\sigma_{|\beta_{t3}\rangle\langle\beta_{t3}|}$ ), four ( $\sigma_{|\beta_{t4}\rangle\langle\beta_{t4}|}$ ) or five ( $\sigma_{|\beta_{t5}\rangle\langle\beta_{t5}|}$ ) superpositions of coherent states. These test states are structured as follows:

$$|\beta_{t3}\rangle = \frac{\beta}{2} (|-1 + i \cdot 0\rangle + |0 + i \cdot 0\rangle + |1 + i \cdot 0\rangle), \quad (5.71)$$

$$|\beta_{t4}\rangle = \frac{\beta}{2} (|-2 + i \cdot 0\rangle + |-1 + i \cdot 0\rangle + |1 + i \cdot 0\rangle + |2 + i \cdot 0\rangle), \quad (5.72)$$

$$|\beta_{t5}\rangle = \frac{\beta}{2} (|-2 + i \cdot 0\rangle + |-1 + i \cdot 0\rangle + |0 + i \cdot 0\rangle + |1 + i \cdot 0\rangle + |2 + i \cdot 0\rangle) \quad (5.73)$$

with the coherent amplitude  $\beta$ . Again the parameters  $\lambda_k$  where chosen equal to one.

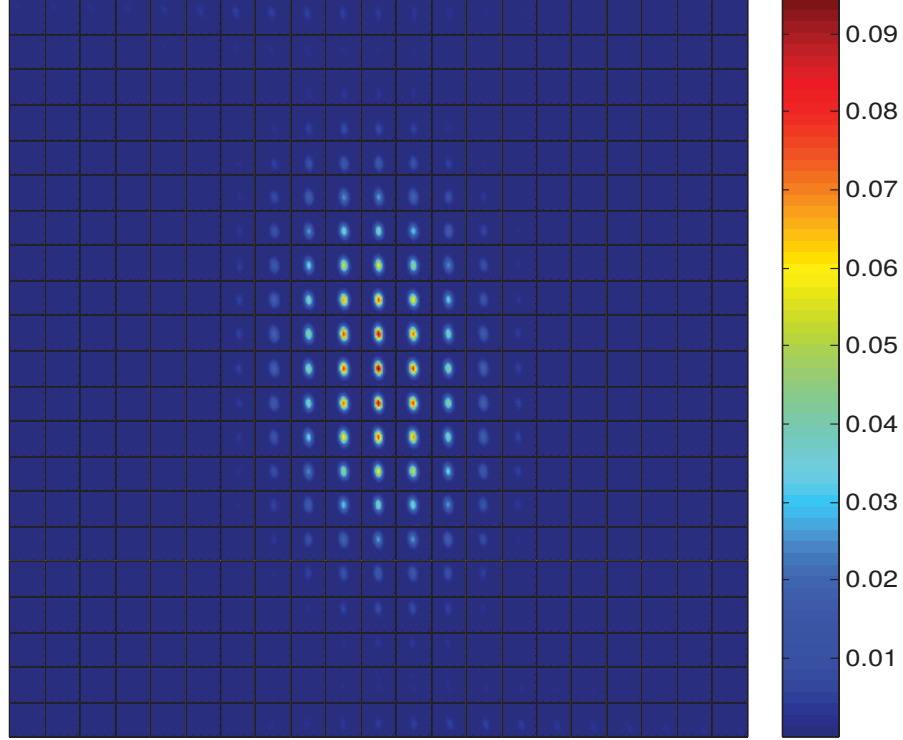


**Figure 5.13.:** Contour plot of the modulus of the reconstructed density matrix in coherent state basis  $\rho_{\alpha'\alpha}$  for a experimentally recorded squeezed state with -4.9 dB squeezing.

The different test states are denoted as  $\mathcal{TS}_{r,\beta}$ , where  $r$  is the number of superpositions of coherent states and  $\beta$  is the coherent amplitude we use. The resulting distances are shown in Tab. 5.3. For the state  $\mathcal{SQ}_{-3,0}$ , the smallest distance is achieved with the test state  $\mathcal{TS}_{5,1}$  ( $\mathcal{D}(\rho_{\alpha'\alpha}(\mathcal{SQ}_{-3,0}), \sigma_{\alpha'\alpha}(\mathcal{TS}_{5,1})) = 0.0783$ ). The Tab. 5.3 already shows, that the more superpositions we use, the closer we get to the optimal test state. It also shows the strong dependence on the coherent amplitude  $\beta$  we use in the generation of the test states. If  $\beta$  is too large or too small, the distance between the investigated state and the test state increases. Moreover, we already found a distance close to 0, which is already close to the optimum, hence we are close to the optimal test state. Now let us take a look at the distances for the squeezed state  $\mathcal{SQ}_{-10,0}$ . The smallest distance is achieved with the test state  $\mathcal{TS}_{5,2}$  ( $\mathcal{D}(\rho_{\alpha'\alpha}(\mathcal{SQ}_{-10,0}), \sigma_{\alpha'\alpha}(\mathcal{TS}_{5,2})) = 0.2972$ ). As this is not even close to 0 this indicates, that we need more superpositions of coherent states in order to decompose the investigated squeezed state with a squeezing of -10 dB. Hence, we can conclude, that the higher the squeezing of our state is, the more superpositions of coherent states we need to decompose the state.

$\mathcal{D}(\rho_{\alpha'\alpha}(\mathcal{SQ}_{-3,0}), \sigma_{\alpha'\alpha}(\mathcal{TS}_{3,1}))$	0.1809	$\mathcal{D}(\rho_{\alpha'\alpha}(\mathcal{SQ}_{-3,0}), \sigma_{\alpha'\alpha}(\mathcal{TS}_{4,4}))$	1.3872
$\mathcal{D}(\rho_{\alpha'\alpha}(\mathcal{SQ}_{-3,0}), \sigma_{\alpha'\alpha}(\mathcal{TS}_{3,2}))$	0.2014	$\mathcal{D}(\rho_{\alpha'\alpha}(\mathcal{SQ}_{-3,0}), \sigma_{\alpha'\alpha}(\mathcal{TS}_{4,5}))$	1.4673
$\mathcal{D}(\rho_{\alpha'\alpha}(\mathcal{SQ}_{-3,0}), \sigma_{\alpha'\alpha}(\mathcal{TS}_{3,3}))$	0.5912	$\mathcal{D}(\rho_{\alpha'\alpha}(\mathcal{SQ}_{-3,0}), \sigma_{\alpha'\alpha}(\mathcal{TS}_{4,6}))$	1.4483
$\mathcal{D}(\rho_{\alpha'\alpha}(\mathcal{SQ}_{-3,0}), \sigma_{\alpha'\alpha}(\mathcal{TS}_{3,4}))$	0.8708	$\mathcal{D}(\rho_{\alpha'\alpha}(\mathcal{SQ}_{-3,0}), \sigma_{\alpha'\alpha}(\mathcal{TS}_{5,1}))$	0.0783
$\mathcal{D}(\rho_{\alpha'\alpha}(\mathcal{SQ}_{-3,0}), \sigma_{\alpha'\alpha}(\mathcal{TS}_{3,5}))$	1.0363	$\mathcal{D}(\rho_{\alpha'\alpha}(\mathcal{SQ}_{-3,0}), \sigma_{\alpha'\alpha}(\mathcal{TS}_{5,2}))$	0.6761
$\mathcal{D}(\rho_{\alpha'\alpha}(\mathcal{SQ}_{-3,0}), \sigma_{\alpha'\alpha}(\mathcal{TS}_{3,6}))$	1.1194	$\mathcal{D}(\rho_{\alpha'\alpha}(\mathcal{SQ}_{-3,0}), \sigma_{\alpha'\alpha}(\mathcal{TS}_{5,3}))$	0.9860
$\mathcal{D}(\rho_{\alpha'\alpha}(\mathcal{SQ}_{-3,0}), \sigma_{\alpha'\alpha}(\mathcal{TS}_{4,1}))$	0.2025	$\mathcal{D}(\rho_{\alpha'\alpha}(\mathcal{SQ}_{-3,0}), \sigma_{\alpha'\alpha}(\mathcal{TS}_{5,4}))$	1.1323
$\mathcal{D}(\rho_{\alpha'\alpha}(\mathcal{SQ}_{-3,0}), \sigma_{\alpha'\alpha}(\mathcal{TS}_{4,2}))$	0.9619	$\mathcal{D}(\rho_{\alpha'\alpha}(\mathcal{SQ}_{-3,0}), \sigma_{\alpha'\alpha}(\mathcal{TS}_{5,5}))$	1.2079
$\mathcal{D}(\rho_{\alpha'\alpha}(\mathcal{SQ}_{-3,0}), \sigma_{\alpha'\alpha}(\mathcal{TS}_{4,3}))$	1.2708	$\mathcal{D}(\rho_{\alpha'\alpha}(\mathcal{SQ}_{-3,0}), \sigma_{\alpha'\alpha}(\mathcal{TS}_{5,6}))$	1.1701
$\mathcal{D}(\rho_{\alpha'\alpha}(\mathcal{SQ}_{-10,0}), \sigma_{\alpha'\alpha}(\mathcal{TS}_{3,1}))$	0.8379	$\mathcal{D}(\rho_{\alpha'\alpha}(\mathcal{SQ}_{-10,0}), \sigma_{\alpha'\alpha}(\mathcal{TS}_{4,4}))$	1.0732
$\mathcal{D}(\rho_{\alpha'\alpha}(\mathcal{SQ}_{-10,0}), \sigma_{\alpha'\alpha}(\mathcal{TS}_{3,2}))$	0.6211	$\mathcal{D}(\rho_{\alpha'\alpha}(\mathcal{SQ}_{-10,0}), \sigma_{\alpha'\alpha}(\mathcal{TS}_{4,5}))$	1.2565
$\mathcal{D}(\rho_{\alpha'\alpha}(\mathcal{SQ}_{-10,0}), \sigma_{\alpha'\alpha}(\mathcal{TS}_{3,3}))$	0.3957	$\mathcal{D}(\rho_{\alpha'\alpha}(\mathcal{SQ}_{-10,0}), \sigma_{\alpha'\alpha}(\mathcal{TS}_{4,6}))$	1.2934
$\mathcal{D}(\rho_{\alpha'\alpha}(\mathcal{SQ}_{-10,0}), \sigma_{\alpha'\alpha}(\mathcal{TS}_{3,4}))$	0.3776	$\mathcal{D}(\rho_{\alpha'\alpha}(\mathcal{SQ}_{-10,0}), \sigma_{\alpha'\alpha}(\mathcal{TS}_{5,1}))$	0.6900
$\mathcal{D}(\rho_{\alpha'\alpha}(\mathcal{SQ}_{-10,0}), \sigma_{\alpha'\alpha}(\mathcal{TS}_{3,5}))$	0.5922	$\mathcal{D}(\rho_{\alpha'\alpha}(\mathcal{SQ}_{-10,0}), \sigma_{\alpha'\alpha}(\mathcal{TS}_{5,2}))$	0.2972
$\mathcal{D}(\rho_{\alpha'\alpha}(\mathcal{SQ}_{-10,0}), \sigma_{\alpha'\alpha}(\mathcal{TS}_{3,6}))$	0.8139	$\mathcal{D}(\rho_{\alpha'\alpha}(\mathcal{SQ}_{-10,0}), \sigma_{\alpha'\alpha}(\mathcal{TS}_{5,3}))$	0.3836
$\mathcal{D}(\rho_{\alpha'\alpha}(\mathcal{SQ}_{-10,0}), \sigma_{\alpha'\alpha}(\mathcal{TS}_{4,1}))$	0.6355	$\mathcal{D}(\rho_{\alpha'\alpha}(\mathcal{SQ}_{-10,0}), \sigma_{\alpha'\alpha}(\mathcal{TS}_{5,4}))$	0.6770
$\mathcal{D}(\rho_{\alpha'\alpha}(\mathcal{SQ}_{-10,0}), \sigma_{\alpha'\alpha}(\mathcal{TS}_{4,2}))$	0.4828	$\mathcal{D}(\rho_{\alpha'\alpha}(\mathcal{SQ}_{-10,0}), \sigma_{\alpha'\alpha}(\mathcal{TS}_{5,5}))$	0.8584
$\mathcal{D}(\rho_{\alpha'\alpha}(\mathcal{SQ}_{-10,0}), \sigma_{\alpha'\alpha}(\mathcal{TS}_{4,3}))$	0.7975	$\mathcal{D}(\rho_{\alpha'\alpha}(\mathcal{SQ}_{-10,0}), \sigma_{\alpha'\alpha}(\mathcal{TS}_{5,6}))$	0.8805

**Table 5.3.:** Distances between the squeezed states  $\mathcal{SQ}_{S,\phi_\xi}$ , with  $\phi_\xi = 0$ , and the test states  $\mathcal{TS}_{r,\beta}$ .

### Experimental recorded squeezed state

As mentioned before, our presented technique is also applicable to experiments. Here, we present the reconstructed density matrix for a squeezed state with -4.9 dB squeezing<sup>4</sup>. We can see that the resulting ellipse, see Fig. 5.13, is tilted, indicating that we had a squeezed state with a slightly rotated phase and, therefore, not pure amplitude squeezing. The distances of the density matrix of the experimentally recorded squeezed state to the density matrices of some test states, the same as in Sec. 5.4.3, are listed in Tab. 5.4. Because of the tilting of the experimentally recorded squeezed state, which is a rotation in phase space, we decided to use test states that are also slightly rotated. We chose a rotation of  $t = \exp(-(\pi i)/30)$  to resemble the experimental rotation. The resulting test states are denoted as  $\mathcal{TS}_{r,\beta,t}$ .

<sup>4</sup>This state was recorded by Semjon Köhnke for the Master project of Hannes Sobottka.

$\mathcal{D}(\rho_{\alpha'\alpha}(\mathcal{SQ}_{ex}), \sigma_{\alpha'\alpha}(\mathcal{TS}_{3,1}))$	0.8162	$\mathcal{D}(\rho_{\alpha'\alpha}(\mathcal{SQ}_{ex}), \sigma_{\alpha'\alpha}(\mathcal{TS}_{4,4}))$	1.6495
$\mathcal{D}(\rho_{\alpha'\alpha}(\mathcal{SQ}_{ex}), \sigma_{\alpha'\alpha}(\mathcal{TS}_{3,2}))$	0.7047	$\mathcal{D}(\rho_{\alpha'\alpha}(\mathcal{SQ}_{ex}), \sigma_{\alpha'\alpha}(\mathcal{TS}_{4,5}))$	1.7492
$\mathcal{D}(\rho_{\alpha'\alpha}(\mathcal{SQ}_{ex}), \sigma_{\alpha'\alpha}(\mathcal{TS}_{3,3}))$	0.8184	$\mathcal{D}(\rho_{\alpha'\alpha}(\mathcal{SQ}_{ex}), \sigma_{\alpha'\alpha}(\mathcal{TS}_{4,6}))$	1.7560
$\mathcal{D}(\rho_{\alpha'\alpha}(\mathcal{SQ}_{ex}), \sigma_{\alpha'\alpha}(\mathcal{TS}_{3,4}))$	1.0525	$\mathcal{D}(\rho_{\alpha'\alpha}(\mathcal{SQ}_{ex}), \sigma_{\alpha'\alpha}(\mathcal{TS}_{5,1}))$	0.7185
$\mathcal{D}(\rho_{\alpha'\alpha}(\mathcal{SQ}_{ex}), \sigma_{\alpha'\alpha}(\mathcal{TS}_{3,5}))$	1.2714	$\mathcal{D}(\rho_{\alpha'\alpha}(\mathcal{SQ}_{ex}), \sigma_{\alpha'\alpha}(\mathcal{TS}_{5,2}))$	0.8738
$\mathcal{D}(\rho_{\alpha'\alpha}(\mathcal{SQ}_{ex}), \sigma_{\alpha'\alpha}(\mathcal{TS}_{3,6}))$	1.419	$\mathcal{D}(\rho_{\alpha'\alpha}(\mathcal{SQ}_{ex}), \sigma_{\alpha'\alpha}(\mathcal{TS}_{5,3}))$	1.1821
$\mathcal{D}(\rho_{\alpha'\alpha}(\mathcal{SQ}_{ex}), \sigma_{\alpha'\alpha}(\mathcal{TS}_{4,1}))$	0.7095	$\mathcal{D}(\rho_{\alpha'\alpha}(\mathcal{SQ}_{ex}), \sigma_{\alpha'\alpha}(\mathcal{TS}_{5,4}))$	1.3752
$\mathcal{D}(\rho_{\alpha'\alpha}(\mathcal{SQ}_{ex}), \sigma_{\alpha'\alpha}(\mathcal{TS}_{4,2}))$	1.1079	$\mathcal{D}(\rho_{\alpha'\alpha}(\mathcal{SQ}_{ex}), \sigma_{\alpha'\alpha}(\mathcal{TS}_{5,5}))$	1.4642
$\mathcal{D}(\rho_{\alpha'\alpha}(\mathcal{SQ}_{ex}), \sigma_{\alpha'\alpha}(\mathcal{TS}_{4,3}))$	1.4701	$\mathcal{D}(\rho_{\alpha'\alpha}(\mathcal{SQ}_{ex}), \sigma_{\alpha'\alpha}(\mathcal{TS}_{5,6}))$	1.4584

**Table 5.4.:** Distances between the experimentally recorded squeezed state  $\mathcal{SQ}_{ex}$  and the test states  $\mathcal{TS}_{r,\beta}$ .

$\mathcal{D}(\rho_{\alpha'\alpha}(\mathcal{SQ}_{ex}), \sigma_{\alpha'\alpha}(\mathcal{TS}_{3,1,t}))$	0.8133	$\mathcal{D}(\rho_{\alpha'\alpha}(\mathcal{SQ}_{ex}), \sigma_{\alpha'\alpha}(\mathcal{TS}_{4,4,t}))$	1.6384
$\mathcal{D}(\rho_{\alpha'\alpha}(\mathcal{SQ}_{ex}), \sigma_{\alpha'\alpha}(\mathcal{TS}_{3,2,t}))$	0.6906	$\mathcal{D}(\rho_{\alpha'\alpha}(\mathcal{SQ}_{ex}), \sigma_{\alpha'\alpha}(\mathcal{TS}_{4,5,t}))$	1.7453
$\mathcal{D}(\rho_{\alpha'\alpha}(\mathcal{SQ}_{ex}), \sigma_{\alpha'\alpha}(\mathcal{TS}_{3,3,t}))$	0.7931	$\mathcal{D}(\rho_{\alpha'\alpha}(\mathcal{SQ}_{ex}), \sigma_{\alpha'\alpha}(\mathcal{TS}_{4,6,t}))$	1.7562
$\mathcal{D}(\rho_{\alpha'\alpha}(\mathcal{SQ}_{ex}), \sigma_{\alpha'\alpha}(\mathcal{TS}_{3,4,t}))$	1.0245	$\mathcal{D}(\rho_{\alpha'\alpha}(\mathcal{SQ}_{ex}), \sigma_{\alpha'\alpha}(\mathcal{TS}_{5,1,t}))$	0.7083
$\mathcal{D}(\rho_{\alpha'\alpha}(\mathcal{SQ}_{ex}), \sigma_{\alpha'\alpha}(\mathcal{TS}_{3,5,t}))$	1.2472	$\mathcal{D}(\rho_{\alpha'\alpha}(\mathcal{SQ}_{ex}), \sigma_{\alpha'\alpha}(\mathcal{TS}_{5,2,t}))$	0.8450
$\mathcal{D}(\rho_{\alpha'\alpha}(\mathcal{SQ}_{ex}), \sigma_{\alpha'\alpha}(\mathcal{TS}_{3,6,t}))$	1.4025	$\mathcal{D}(\rho_{\alpha'\alpha}(\mathcal{SQ}_{ex}), \sigma_{\alpha'\alpha}(\mathcal{TS}_{5,3,t}))$	1.1543
$\mathcal{D}(\rho_{\alpha'\alpha}(\mathcal{SQ}_{ex}), \sigma_{\alpha'\alpha}(\mathcal{TS}_{4,1,t}))$	0.6964	$\mathcal{D}(\rho_{\alpha'\alpha}(\mathcal{SQ}_{ex}), \sigma_{\alpha'\alpha}(\mathcal{TS}_{5,4,t}))$	1.3574
$\mathcal{D}(\rho_{\alpha'\alpha}(\mathcal{SQ}_{ex}), \sigma_{\alpha'\alpha}(\mathcal{TS}_{4,2,t}))$	1.0841	$\mathcal{D}(\rho_{\alpha'\alpha}(\mathcal{SQ}_{ex}), \sigma_{\alpha'\alpha}(\mathcal{TS}_{5,5,t}))$	1.4659
$\mathcal{D}(\rho_{\alpha'\alpha}(\mathcal{SQ}_{ex}), \sigma_{\alpha'\alpha}(\mathcal{TS}_{4,3,t}))$	1.4509	$\mathcal{D}(\rho_{\alpha'\alpha}(\mathcal{SQ}_{ex}), \sigma_{\alpha'\alpha}(\mathcal{TS}_{5,6,t}))$	1.4682

**Table 5.5.:** Distances between the experimentally recorded squeezed state  $\mathcal{SQ}_{ex}$  and the tilted test states  $\mathcal{TS}_{r,\beta,t}$ .

In Tab. 5.5, we listed the distances of the reconstructed density matrix of the experimentally recorded squeezed state to the density matrices of the titled test states. Even though the distances reduced a little, they are still significantly larger than 0 and, therefore, we cannot make a reasonable statement which test state decomposes the experimentally squeezed state best. However, this illustrates the potential of the reconstruction method.

In all our considerations so far, we tried to reduce the number of test states by making some assumptions, e.g.,  $\lambda_k$  are equal to one. For a general investigation we need to optimize all possible parameters, i.e., the number of superpositions of coherent states  $r$ , the coherent amplitudes  $\beta$ , the parameters  $\lambda_k$ , and a possible rotation in phase space. We need to implement an algorithm that includes all of these parameters and optimizes

them to find the optimal test state. Finally, we still need to connect the distance  $\mathcal{D}$  with the bound  $b_r$ .

## 5.5. Summary and outlook

In this chapter, we introduced a witness to measure the amount of nonclassicality in quantum systems in terms of superpositions of coherent states. We applied the Hahn-Banach separation theorem to prove that the presented witnessing approach is necessary and sufficient. With this knowledge, we were able to formulate and solve an optimization problem, which requires to solve an eigenvalue problem. Moreover, we constructed a general optimal witness and solved the problem of finding a proper witness for pure states completely. Exemplary, we studied an unbound operator, based on the quadrature variances, and computed the degree of nonclassicality in terms of squeezing. This makes the presented measure experimentally accessible. Finally, we introduced a reconstruction of the density matrix of a quantum state from quadrature data in the coherent state basis. This reconstruction was performed for two simple examples, before applying it to the witnessing approach. We used a compass state as an intuitive example to find a general method to quantify the amount of nonclassicality with the reconstructed density matrices. To achieve this, we introduced test states with which we compared our compass state in terms of the Euclidean distance. We were not able to align the distance to a specific bound. But using the distance, we still have an indicator how good the decomposition of our quantum state into superpositions of coherent states is. We then applied this distance method to two different squeezed states with different squeezing strength and found that, the stronger the squeezing is, the higher is the distance with respect to the same number of superpositions of coherent states. Finally, we applied our method to an experimentally recorded squeezed state.

The question, how to connect the distance to the bound  $b_r$  is still open. Also we need to implement an algorithm, that includes all the different parameters and optimizes the distance for the state of interest, which is mainly a numerical issue.

## Chapter 6.

### Further work

During the course of a PhD, a lot of work is done, which is typically not present in the final thesis. Therefore, this chapter is dedicated to two examples of the further projects that were addressed during my PhD project. First, we will go back to the MC presented in Sec. 3.2, as during this thesis an optimized building technique for MCs was developed. Second, a joint project with the *Theoretical Quantum Optics Group* of Prof. Dr. Werner Vogel, specifically with Sergej Ryl and Dr. Jan Sperling, on unified nonclassicality criteria is discussed.

Note that these further projects are not discussed in detail as all the features would go beyond the scope of this thesis.

#### 6.1. Building a Mode Cleaner

As mentioned in Sec. 3.2, the MCs are a crucial part of the experiment. If we want to build such a device, we face the problem of positioning of the curved mirror M3, see Fig. 3.2. It is crucial that M3 is positioned correctly, in order to setup a stable cavity with a high finesse and, therefore, low loss per round trip. However, the correct position of the mirrors, especially M3, is not the only mandatory requirement of the MC, we also need to make sure that the mirrors are free of any dust or other impurities. To keep the mirrors and the interior of the MC clean, we choose to glue the mirrors onto the copper block. This has the benefit, that as soon as we are done with the gluing, the cavity will stay clean and stable for years. But this technique has the drawback that due to the gluing we have just one try. Therefore, if we want to succeed, we need a feedback for the right position before gluing.

The gluing of the two plain mirrors onto the copper block is not critical. We only have to make sure, that the surfaces of the copper and the mirror are clean, to which we glue the mirror is parallel to the ground, as the mirror might shift its position during the gluing process otherwise, and that the mirror is not pushed over the surface of the copper block, as this might produce some scratches on the mirror surface and hence reduce the quality of the mirror and thereby reduce the finesse of the resonator. To ensure that the mirror is not moved during the application of the glue, we put a little weight on top of the mirror.

The same technique is used for gluing first the PZT to the end of the copper block and afterwards a plain brass ring. This ring is necessary as the PZT does not have the right diameter to directly glue the final mirror onto it. After these two components are fixed onto the copper block, the block is brought into its final position. A laser beam at 532 nm is aligned into the resonator in such a way that the beam exits the back side of the copper block at its center. As the third mirror is not plain but has a radius of curvature of 100 cm, the positioning of this mirror is far more demanding. Therefore, a combination of a linear manual translation stage, a mirror mount and a lens mount is used, see the left side of Fig. 6.1. The mirror is placed into the lens mount, which enables us to align the height and the left right position (x-y position) and we use the mirror mount to align the inclination of the mirror. If these alignments would take place directly on the brass ring, we would risk to damage the mirror. Hence, we align the inclination and x-y position in a distance of approximately 5 mm and then use the translation stage to bring the mirror slowly into contact with the brass ring. Every misalignment during this process is immediately corrected with the lens and mirror mounts holding the mirror. To guarantee a good alignment, an additional PZT is used, see the right side of Fig. 6.1. This PZT is placed on the front side of the copper block at its center. In this way, it is possible to change the cavity length as the hole copper block is shifted and the back mirror is static. The mode picture is characteristic for the resonator and gives us the information about the quality of the cavity via the finesse, cf. Fig. 3.3, as the distance between two peaks on one slope of the ramp applied to the piezo is the FSR of the resonator. Additionally we measure the FWHM of one peak in the mode picture, and therefore, we can calculate the finesse, cf. Eq. (3.1). If we compare the theoretical with the actual finesse, we can decide whether the cavity is high quality enough and can glue the final mirror onto the brass ring or not. While moving the back mirror the mode picture will vanish until the mirror stands still again. As soon as the mirror has contact with the copper block, the mirror is glued on 4 points to fix the position. After the glue is hardened, the special mirror aligning tool is removed and the PZT attached to copper

block and mirror is used to scan the cavity length. If the mode picture still shows the high quality the glue is spread around the hole mirror, so that no dust can enter the cavity and the mode cleaner is ready for use. If this is not the case, we have to reopen the cavity and restart the procedure.

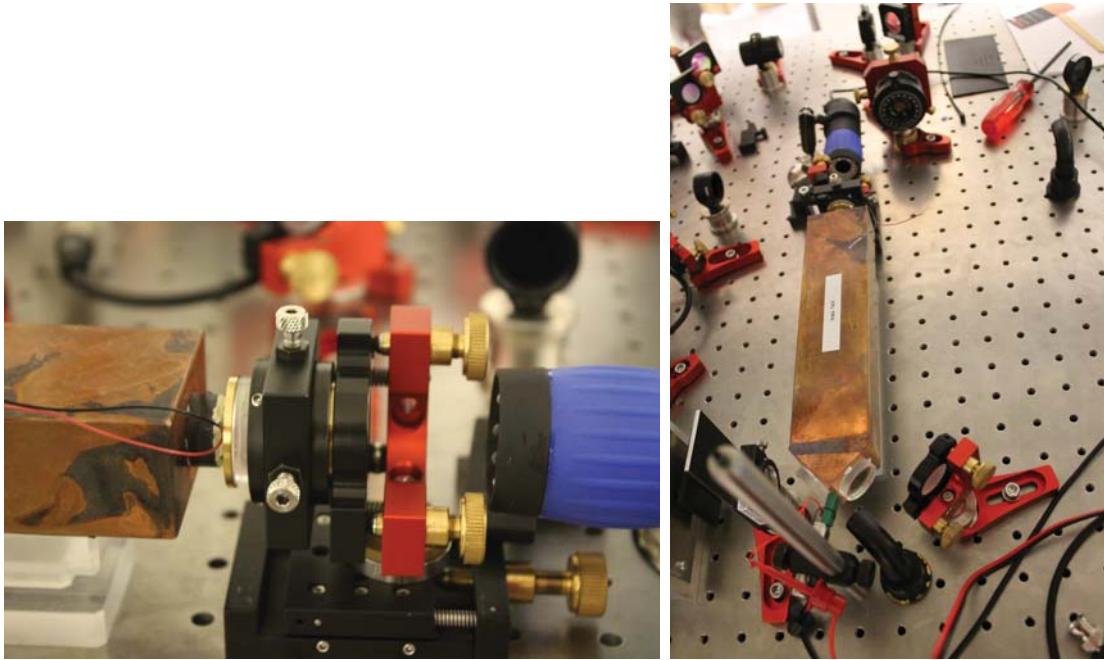


**Figure 6.1.:** Setup for gluing the back mirror, whose positioning is quiet demanding. **Left:** Close up of the mirror mount, which is a combination of a linear manual translation stage, a mirror mount and a lens mount, used for the positioning of the back mirror. **Right:** Full gluing set up including an additional PZT.

## 6.2. Unified Nonclassicality Criteria

This section concerns another joint project with the *Theoretical Quantum Optics Group* of Prof. Dr. Werner Vogel this time specifically with Sergej Ryl and Dr. Jan Sperling. The results achieved during this cooperation were published in [2] and are partly presented in this section. Hence, more details may be found in [2]. Note that, the theoretical derivation of the presented method, as well as the data analysis was done by Sergej Ryl. My co-worker Semjon Köhnke and me build the setup and acquired the data.

The aim of this project was to generalize the Bochner theorem [Vog00, RV02, RV33] by including derivations of the characteristic function. Therefore, the theoretical group developed the criterion, and we provided the experimental data for the application of this

criterion. This extension results in necessary and sufficient nonclassicality criteria and unifies the well known moment-based criteria [SRV05, SV05b] with those based on the characteristic function [Vog00, RV02, RV33]. To do so, we focused on two hierarchies of criteria, whereas both prove that the  $P$ -function is not a classical probability distribution in terms of experimental accessible quantities.

Let us start with the first hierarchy based on Bochner's theorem and the characteristic function. The characteristic function itself is the Fourier transform of the  $P$ -function [Vog00, RV02] and can be directly sampled from BHD [LS02, ZPB07, KVH09, MKN11b]. The second hierarchy is based on the matrix of moments [SRV05, SV05b], which contains statistical moments of the  $P$ -function. Whereas the different moments can identify different quantum effects. Some 2nd order moments can identify sub-Poisson [Man79] and squeezed light [SHY85], whereas higher order moments also identify entanglement [SV05a, MBW10] and space-time dependent quantum correlations [Vog08].

As mentioned above, we can directly sample the characteristic function of an investigated state out of BHD data. The  $P$ -function is for some states, as for example squeezed states, a highly singular distribution. Its characteristic function

$$\Phi(\beta) = \int d^2\alpha P(\alpha) e^{\beta\alpha^* - \beta^*\alpha}, \quad (6.1)$$

however, is a well behaved function.

At this point, we can apply Bochner's theorem as it provides necessary and sufficient conditions for a function to be a Fourier transform of a classical probability density [RV02, RV33]. It states that  $\Phi(\beta)$  is the characteristic function of a classical state if

- (i) the characteristic function is normalized  $\Phi(0) = 1$ ,
- (ii) the characteristic function is hermitic  $\Phi(-\beta) = \Phi^*(\beta)$ ,
- (iii) the characteristic function is positive semidefinite  $\rightarrow$  for any positive integer  $N$  and arbitrary complex numbers  $\beta_1, \dots, \beta_N$  holds

$$\Phi = [\Phi(\beta_i - \beta_j)]_{i,j=1}^N \geq 0. \quad (6.2)$$

The first two conditions are fulfilled by every state, regardless if the state is classical or not. Hence, the third condition is the condition of interest to distinguish between classical and nonclassical states. We use this condition and combine it with the matrix

of moments to formulate the generalized Bochner matrix (GBM)

$$\partial\Phi = \left[ (-1)^{n_i+m_j} \partial_{\beta}^{n_i+m_j} \partial_{\beta^*}^{n_i+m_j} \Phi(\beta) \Big|_{\beta=\beta_i-\beta_j} \right]_{i,j=1}^N, \quad (6.3)$$

where  $\vec{n} = (n_1, \dots, n_N)^T$  and  $\vec{m} = (m_1, \dots, m_N)^T$  are integers. Here we state, that for any classical state the GBM is positive semidefinite, i.e.  $\partial\Phi \geq 0$ . As this GBM is a combination of the characteristic function and the matrix of moments, we can formulate a minor representation for the generalized Bochner theorem: For a nonclassical state there exists a positive integer  $N$ , non-negative integers  $\vec{n}$  and  $\vec{m}$  and complex numbers  $\beta_1, \dots, \beta_N$  such that

$$\det \partial\Phi < 0. \quad (6.4)$$

Note that for specific values of  $\vec{n}$ ,  $\vec{m}$  and  $\beta_1, \dots, \beta_N$ , we end up at the original hierarchies. Hence, for  $n_1 = \dots = n_N = m_1 = \dots = m_N = 0$  we end up with the original Bochner matrices as in Eq. (6.2) of the same dimensionality  $N$ . Furthermore for  $\beta_1 = \dots = \beta_N = 0$  the GBM corresponds to the matrix of moments.

With our nonclassicality theorem based on the GBM, we simultaneously use the Bochner and the local matrix of moments nonclassicality probes.

As mentioned above, the characteristic function can be directly sampled from the BHD data

$$\Phi(\beta) = e^{|\beta|^2/2} \frac{1}{M} \sum_{j=1}^M e^{i|\beta|x_j(\phi)}, \quad (6.5)$$

where  $[x_j(\phi)]_{j=1}^M$  are  $M$  quadrature values  $x_j$  at the phase  $\phi$ .

Therefore, we can also sample the GBM from BHD data as it is based on the characteristic function as:

$$\begin{aligned} \partial_{\beta}^m \partial_{\beta^*}^n \Phi(\beta) &\approx \frac{1}{M} \sum_{j=1}^M e^{i(m-n)\phi_j} \left[ m D_n^{m-1}(x_j, \beta e^{i\phi_j}) + \beta e^{i\phi_j} D_n^m(x_j, \beta e^{i\phi_j}) \right. \\ &\quad \left. + n D_m^{n-1}(-x_j, \beta e^{-i\phi_j}) + \beta^* e^{-i\phi_j} D_m^n(-x_j, \beta e^{-i\phi_j}) \right] \end{aligned} \quad (6.6)$$

with the derivatives

$$D_q^r(x, \gamma) = \sum_{k_1+k_2+k_3=r} \frac{r!(-1)^{q+k_1+k_3}(q+k_1)!2^{-k_3/2}}{k_1!k_2!k_3!(\gamma+\gamma^*)^{q+k_1+1}} x^{k_2} e^{x\gamma-\gamma^2/2} H_{k_3}(\gamma/\sqrt{2}), \quad (6.7)$$

where  $H_{k_3}(\gamma/\sqrt{2})$  are Hermite polynomials and  $(x_j, \phi_j)_{j=1}^M$  is the quadrature distribution provided by the experiment.

With this formula, we can now directly test the nonclassicality of our generated quantum state.

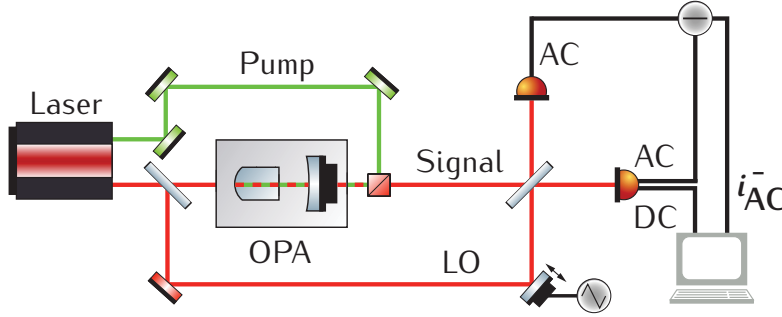


**Figure 6.2.:** Schematic of the experimental setup used to generate and measure the squeezed vacuum state. The OPA, containing a 7%MgO:LiNbO<sub>3</sub> crystal, was pumped with 290 mW at 532 nm resulting in a parametric gain of 3.3 and therefore in -4.13 dB squeezing at 1064 nm. The phase variation and readout was done using the continuous phase variation technique.

For the experimental application of our nonclassicality test, we generated a squeezed vacuum state in our OPA with the 7%MgO:LiNbO<sub>3</sub> crystal, cf. Fig. 6.2. We pumped it with 290 mW at 532 nm resulting in a parametric gain of 3.3 and, therefore, in -4.13 dB squeezing and 6.11 dB antisqueezing at 1064 nm. The overall efficiency of the experiment was 77%. For the phase estimation, we used again the continuous phase variation presented in Sec. 3.8 and [1].

With the experimentally sampled quadratures, we calculated a minor  $\det(\partial\Phi)$  of the GBM as shown in Fig. 6.3. In this figure, we plotted the second-order minor  $\det(\partial\Phi)$

$$\det \partial\Phi = \det \begin{pmatrix} 1 & -\langle : \hat{a} e^{\beta \hat{a}^\dagger - \beta^* \hat{a}} : \rangle \\ -\langle : \hat{a} e^{-\beta \hat{a}^\dagger + \beta^* \hat{a}} : \rangle & \langle : \hat{a}^\dagger \hat{a} : \rangle \end{pmatrix}, \quad (6.8)$$

where  $m_1 = m_2 = n_1 = 0, n_2=1$  and  $\beta = \beta_1 - \beta_2$  and  $::$  denotes normal operator ordering, along with the signed significance, contour plot,

$$\Sigma [\det(\partial\Phi)] = \frac{\det(\partial\Phi)}{\sigma [\det(\partial\Phi)]} \quad (6.9)$$

with the standard deviation  $\sigma [\det(\partial\Phi)]$ .

For a wide range of values  $\beta$ , we see that the minor  $\det(\partial\Phi)$  is negative and therefore according to inequality (6.4) certifies nonclassicality. The highest significance is reached at  $\det(\partial\Phi)|_{\beta=0} = -0.469 \pm 0.007$  with 70 standard deviations significance [2].

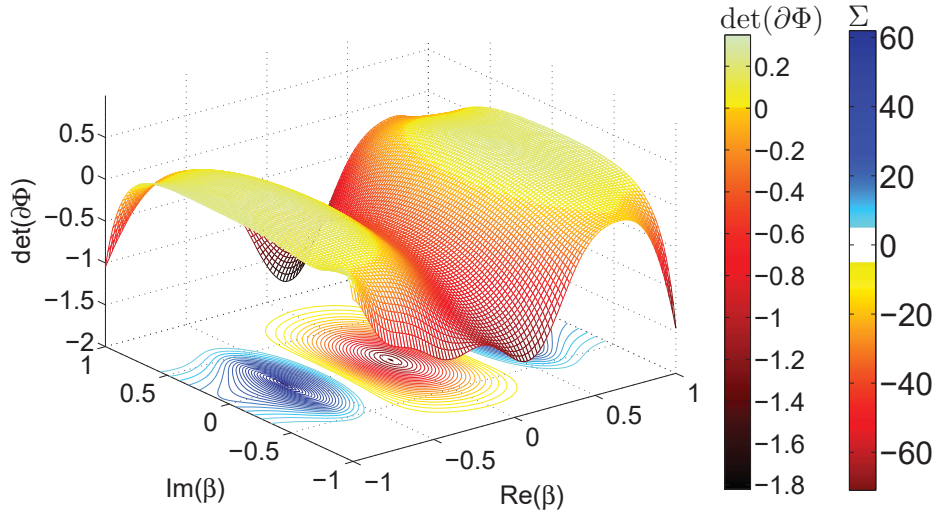


**Figure 6.3.:** The figure shows the sampled determinant  $\det(\partial\phi)$  as surface plot and the significances as contour plot gained from experimental data. The negativities of the determinant proves the nonclassicality of the investigated squeezed vacuum state. The nonclassicality of the squeezed state is certified with a significance up to 70 standard deviations at its origin.

In conclusion we derived necessary and sufficient nonclassicality probes by generalizing Bochner's theorem. This generalized Bochner theorem utilizes the benefits of both, the original Bochner theorem, allowing nonlocal characteristics in phase space, and the matrix of moments, which directly yields quantum features such as squeezing. Furthermore, we formulated a sampling formula to obtain the GBM out of data gained with a BHD and we used it to apply the generalized Bochner theorem to an experimentally generated squeezed vacuum state and we verified the state to be nonclassical.



## Chapter 7.

### Summary and Outlook

In this thesis, we gave a general introduction into the theoretical and experimental foundations of quantum optics used in this thesis. All the experimental tools presented, even so partly standard tools in quantum optics, were build in the framework of this thesis, in order to generate squeezed vacuum states and coherently displaced squeezed states. A new tool, the continuous sampling method was also discussed, as it is a crucial part of the performed experiments. We presented and discussed the homodyne cross correlation measurement, which uses an unbalanced beam splitter and equal powers in signal and local oscillator, showing nonclassical effects without any a priori assumptions about quantum physics in the experiment and the calculations. By doing so, we were able to extract three different noise moments of the field strength, the intensity, and their correlations from a simultaneous measurement. These moments were used in a formulated nonclassicality test that proved the nonclassical behavior of a phase squeezed state even in the anti-squeezed phase region, where the standard technique balanced homodyne detection fails to show nonclassicality. Afterwards we gave an introduction into the witnessing of nonclassicality of quantum states, which is not only a theoretical construct, but is also experimental accessible, e.g. by using the squeezing strength. In this context we also presented the reconstruction of density matrices in coherent state basis. That the reconstruction is possible with experimental data was shown for an experimentally generated and measured squeezed state. We used the reconstructed density matrices in order to find a general experimentally accessible approach for the quantification of nonclassicality. We were able to do this in terms of the Euclidean distance, which indicates how close we are to the optimal decomposition of our investigated quantum state. However, by using the distance we have no information, whether or not we used too many superpositions of coherent states to decompose our quantum state. This information can

only be provided by the bound  $b_r$ . Moreover, only this bound is a necessary, sufficient and unique witness for the amount of nonclassicality.

Hence, we need to find a connection between the distance and the bound, in order to find the right decomposition of our quantum state. Moreover, the task of implementing an optimization algorithm that finds the optimal test state for the decomposition is still open. The difficulty here arises from the great number of possible test states, which must be compared with the quantum state of interest. In order to do so efficiently, we need to find more restrictions in the generation of our test states, as with an increasing number of superpositions of coherent states necessary for the decomposition of the quantum state, also the number of parameters that needs the optimization increases.

## Appendix A.

### Relation between transmitted power and measured voltage

Here the relation between the power transmitted through a resonator and the in transmission measured voltage using a PD is shown. The power transmittivity is given by

$$T_f = \frac{I_f}{I_{0,f}}, \quad (\text{A.1})$$

where  $I_f$  is the transmitted intensity and  $I_{0,f}$  is the intensity incident on the resonator. The index  $f$  refers to the high (h) and low (l) finesse respectively. The intensity incident on the resonator is the same for both the low and the high finesse and therefore, the ratio of the power transmittivities is

$$\frac{T_h}{T_l} = \frac{I_h}{I_l}. \quad (\text{A.2})$$

As the intensity is defined as power  $P$  per area  $A$ ,

$$I_f = \frac{P_f}{A}, \quad (\text{A.3})$$

and as the area is equal for both finessees, we can write

$$\frac{T_h}{T_l} = \frac{I_h}{I_l} = \frac{P_h}{P_l}. \quad (\text{A.4})$$

The measured power is

$$P = \frac{E}{t}, \quad (\text{A.5})$$

where  $E$  is the energy of the transmitted light that reaches the PD in the time  $t$ . The corresponding current measured with the PD is

$$I = \eta \frac{n \cdot e}{t} \quad (\text{A.6})$$

with  $\eta$  being the quantum efficiency of the PD,  $n$  is the number of electrons that are emitted by the light sensitive semiconductor due to the photoelectric effect per time  $t$  and  $e$  is the elementary charge. Further, from simple electronics we can write the current  $I = U/R_{\text{TI}}$ , where  $U$  is the voltage we actually measure with the PD and  $R_{\text{TI}}$  is the resistor in the transimpedance amplifier, see Sec. 3.6. The energy of  $n$  photons at the wavelength  $\lambda$  is

$$E = \frac{n \cdot h \cdot c}{\lambda}. \quad (\text{A.7})$$

Combining Eqs. (A.5)-(A.7) and using  $I = U/R_{\text{TI}}$  we receive

$$U = \frac{R_{\text{TI}} \cdot \eta \cdot \lambda \cdot e}{h \cdot c} \cdot P. \quad (\text{A.8})$$

As every value except  $U$  and  $P$  in Eq. (A.8) is constant for a specific wavelength, we end up with  $U \propto P$  and therefore

$$\frac{T_{\text{h}}}{T_{\text{l}}} = \frac{I_{\text{h}}}{I_{\text{l}}} = \frac{P_{\text{h}}}{P_{\text{l}}} \propto \frac{U_{\text{h}}}{U_{\text{l}}}. \quad (\text{A.9})$$

## Appendix B.

### Characteristics of the PDs

Here we display the characteristics of the two of the PDs used as homodyne detectors in the experiments performed during this thesis. As these PDs come in pairs, it is mandatory, that both detectors have the same transfer function and quantum efficiencies. The DC current in dependence of the incoming laser power and transfer functions of this pair is shown in this appendix. The name of each PD, results from the purpose it is going to serve, the month when it was build and its number in the building order of the detectors in that month. For example Homo16/5/4 is a homodyne PD and the fourth one build in May.

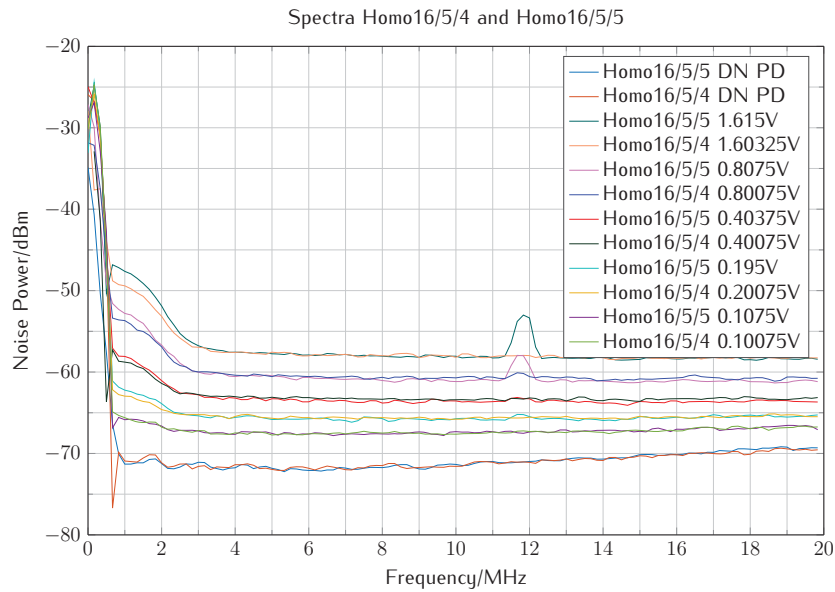


**Figure B.1.:** Spectra of the PDs Homo16/5/4 and Homo16/5/5 taken with the spectrum analyzer for. Between each spectra we bisect the laser power sent onto the PD. The dark noise of the detectors is already subtracted.

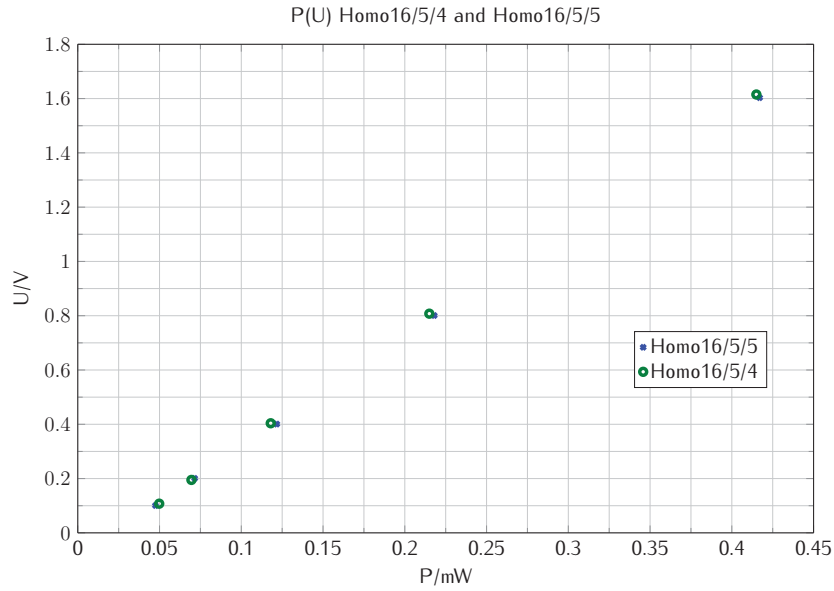


Figure B.2.: DC current ( $U$ ) in dependency of the applied laser power ( $P$ ) for the PDs Homo16/5/4 (green circles) and Homo16/5/5 (blue crosses). Both detectors display the same slope and therefore the same quantum efficiency.

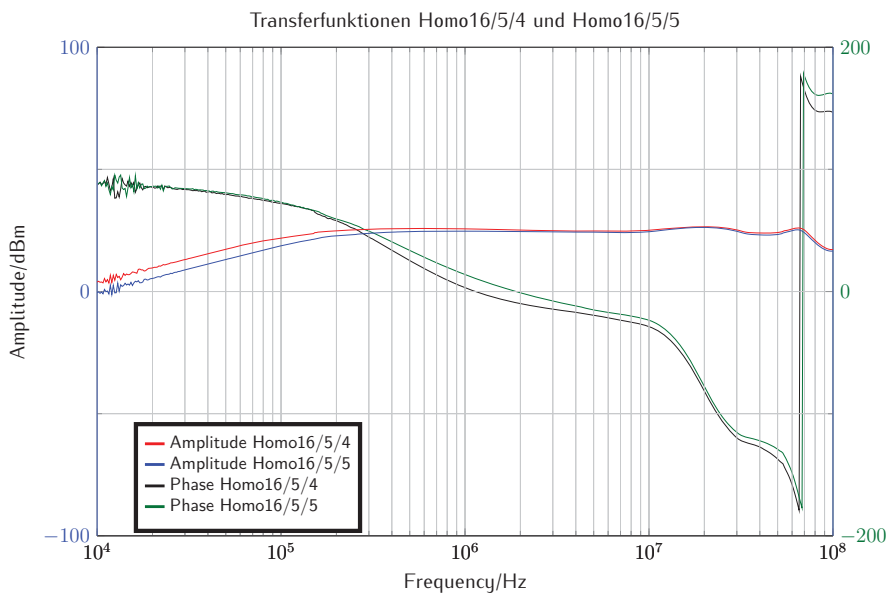
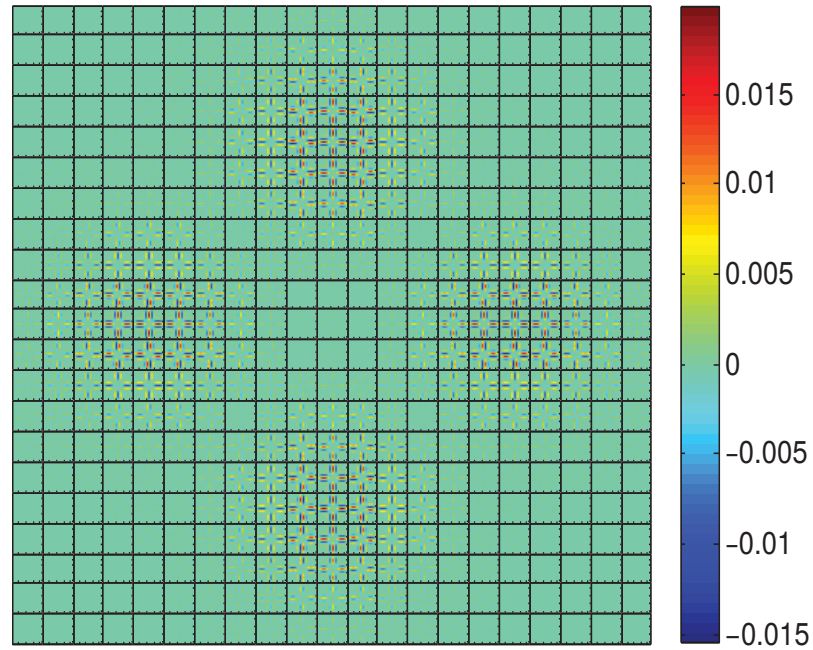


Figure B.3.: Transfer functions in amplitude and phase of the PDs Homo16/5/4 and Homo16/5/5.

## Appendix C.

### More possible visualizations of the density matrices $\rho_{\alpha,\alpha'}$

In this appendix we show the real and imaginary parts of the density matrix elements of  $\rho_{\alpha,\alpha'}$  for the simulated compass state. Here, we superimposed 4 coherent states with a coherent amplitude  $\beta = 3 + i \cdot 0$ , c.f. Sec. 5.4.3.



**Figure C.1.:** Contour plot of the real part of the reconstructed density matrix in coherent state basis  $\rho_{\alpha'\alpha}$  for a compass state with four superpositions of coherent states ( $R = 4$ ) with an coherent amplitude of  $\beta = 4$ .

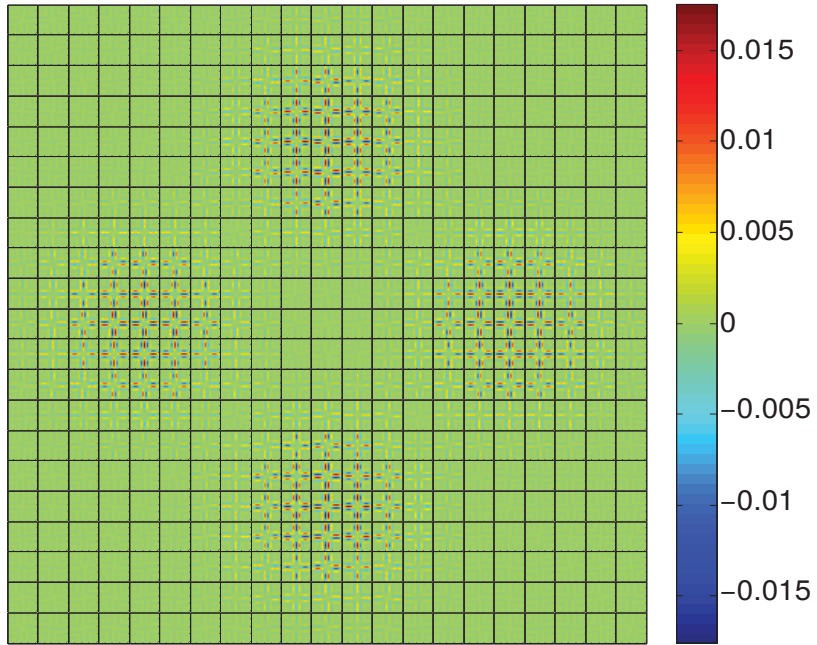


Figure C.2.: Contour plot of the imaginary part of the reconstructed density matrix in coherent state basis  $\rho_{\alpha'\alpha}$  for a compass state with four superpositions of coherent states ( $R = 4$ ) with an coherent amplitude of  $\beta = 3 + i \cdot 0$ .

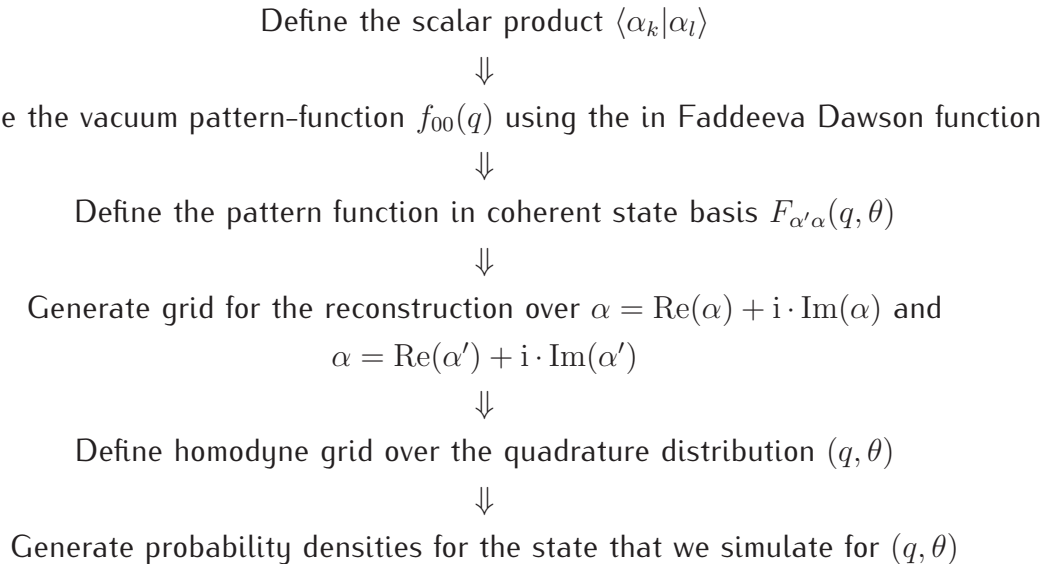
## Appendix D.

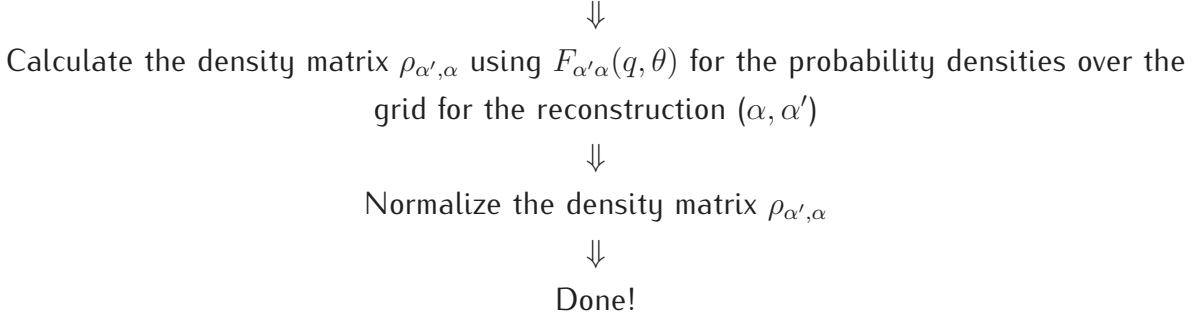
### General simulation approach

In this appendix we give a general walk through how to simulate a quantum state and reconstruct its density matrix in coherent state basis and how to calculate the test states. All the simulation done during the course of this PhD project were performed using Matlab. Hence, some details in the simulation will be given in terms of the Matlab computer language.

#### D.1. Simulation of the quantum state

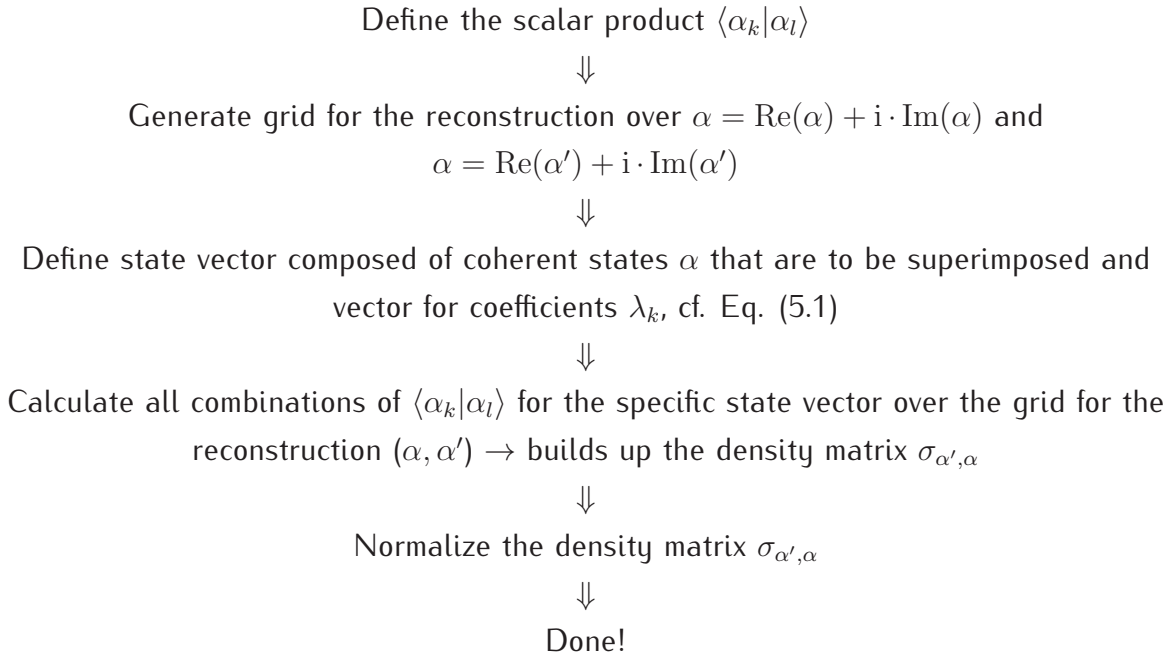
We simulate the quantum state in terms of homodyne data. Hence, the reconstruction is similarly possible for experimentally quantum states measured in BHD. For the simulation and reconstruction we have to execute the following steps:





## D.2. Generation of test states

The test states we use are calculated analytically by executing the following steps:



The state vector that is composed of coherent states can be generated as follows: For example, a compass state with  $R = 4$ , cf. Eq. (2.16), reads

$$|\beta_4\rangle = \lambda_1 |\alpha_1 \exp(2\pi i \cdot 0)/4\rangle + \lambda_2 |\alpha_2 \exp(2\pi i \cdot 1)/4\rangle + \lambda_3 |\alpha_3 \exp(2\pi i \cdot 2)/4\rangle + \lambda_4 |\alpha_4 \exp(2\pi i \cdot 3)/4\rangle \quad (\text{D.1})$$

and is converted to the state vector:

$$calpha = \exp(\phi_{\text{rot}}) \cdot \beta/2 [1i - 1i1 - 1], \quad (\text{D.2})$$

where  $\phi_{\text{rot}}$  is a rotation angle, e.g., used to generate the tilted test states in Sec. 5.4.3 and  $\beta$  is the complex amplitude. The coefficients  $\lambda_1, \dots, \lambda_4$  are encoded in the coefficient vector: `coeffs[ $\lambda_1$   $\lambda_2$   $\lambda_3$   $\lambda_4$ ]`.







# Bibliography

- [ACR05] J. K. Asbóth, J. Calsamiglia and H. Ritsch: *Computable Measure of Non-classicality for Light*. Phys. Rev. Lett. 94, S. 173602, May 2005, URL <https://link.aps.org/doi/10.1103/PhysRevLett.94.173602>.
- [ADR82] A. Aspect, J. Dalibard and G. Roger: *Experimental Test of Bell's Inequalities Using Time-Varying Analyzers*. Phys. Rev. Lett. 49, S. 1804–1807, Dec 1982, URL <https://link.aps.org/doi/10.1103/PhysRevLett.49.1804>.
- [AMJ12] S. Armstrong, J.-F. Morizur, J. Janousek, B. Hage, N. Treps, P. K. Lam and H.-A. Bachor: *Programmable multimode quantum networks* 3, S. 1026, aug 2012.
- [AO16] E. Agudela Ospina: *Private Communication*. 2016.
- [AP04] G. S. Agarwal and P. K. Pathak: *Mesoscopic superposition of states with sub-Planck structures in phase space*. Phys. Rev. A 70, S. 053813, Nov 2004, URL <https://link.aps.org/doi/10.1103/PhysRevA.70.053813>.
- [ASV13] E. Agudelo, J. Sperling and W. Vogel: *Quasiprobabilities for multipartite quantum correlations of light*. Phys. Rev. A 87, S. 033811, Mar 2013, URL <https://link.aps.org/doi/10.1103/PhysRevA.87.033811>.
- [At13] J. Aasi et. al.: *Enhanced sensitivity of the LIGO gravitational wave detector by using squeezed states of light*. Nat Photon 7 (8), S. 613–619, aug 2013, URL <http://www.nature.com/nphoton/journal/v7/n8/abs/nphoton.2013.177.html#supplementary-information>.
- [BBB92] C. H. Bennett, F. Bessette, G. Brassard, L. Salvail and J. Smolin: *Experimental quantum cryptography*. Journal of Cryptology 5 (1), S. 3–28, Jan 1992, URL <https://doi.org/10.1007/BF00191318>.
- [Bel64] J. S. Bell: *On the einstein podolsky rosen paradox* 1964.

- [BHD96] M. Brune, E. Hagley, J. Dreyer, X. Maître, A. Maali, C. Wunderlich, J. M. Raimond and S. Haroche: *Observing the Progressive Decoherence of the "Meter" in a Quantum Measurement*. Phys. Rev. Lett. 77, S. 4887–4890, Dec 1996, URL <https://link.aps.org/doi/10.1103/PhysRevLett.77.4887>.
- [BK68] G. D. Boyd and D. A. Kleinman: *Parametric Interaction of Focused Gaussian Light Beams*. Journal of Applied Physics 39 (8), S. 3597–3639, 1968, URL <http://dx.doi.org/10.1063/1.1656831>.
- [BL05] S. L. Braunstein and P. van Loock: *Quantum information with continuous variables*. Rev. Mod. Phys. 77, S. 513–577, Jun 2005, URL <https://link.aps.org/doi/10.1103/RevModPhys.77.513>.
- [Bla01] E. D. Black: *An introduction to Pound–Drever–Hall laser frequency stabilization*. American Journal of Physics 69 (1), S. 79–87, 2001, URL <http://scitation.aip.org/content/aapt/journal/ajp/69/1/10.1119/1.1286663>.
- [BLB01] B. C. Buchler, P. K. Lam, H.-A. Bachor, U. L. Andersen and T. C. Ralph: *Squeezing more from a quantum nondemolition measurement*. Phys. Rev. A 65, S. 011803, Dec 2001, URL <https://link.aps.org/doi/10.1103/PhysRevA.65.011803>.
- [Bow98] W. P. Bowen: *Experiments towards a Quantum Information Network with Squeezed Light and Entanglement, Dissertation*. 1998.
- [Boy08] R. W. Boyd (Hg.): *Nonlinear Optics*. Academic Press, Burlington, 2008, third edition Aufl.
- [BPM97] Bouwmeester Dik, Pan Jian-Wei, Mattle Klaus, Eibl Manfred, Weinfurter Harald and Zeilinger Anton: *Experimental quantum teleportation*. Nature 390 (6660), S. 575–579, dec 1997, 10.1038/37539.
- [BR08] H.-A. Bachor and T. C. Ralph: *A Guide to Experiments in Quantum Optics*. Wiley-VCH Verlag GmbH, 2008, URL <http://dx.doi.org/10.1002/9783527619238>.
- [BSBL02] W. P. Bowen, R. Schnabel, H.-A. Bachor and P. K. Lam: *Polarization Squeezing of Continuous Variable Stokes Parameters*. Phys. Rev. Lett. 88, S. 093601, Feb 2002, URL <https://link.aps.org/doi/10.1103/PhysRevLett.88.093601>.

- [CR00] J. P. Clemens and P. R. Rice: *Nonclassical effects of a driven atoms-cavity system in the presence of an arbitrary driving field and dephasing*. Phys. Rev. A 61, S. 063810, May 2000, URL <https://link.aps.org/doi/10.1103/PhysRevA.61.063810>.
- [D'A95] G. M. D'Ariano: *Tomographic measurement of the density matrix of the radiation field*. Quantum and Semiclassical Optics: Journal of the European Optical Society Part B 7 (4), S. 693, 1995, URL <http://stacks.iop.org/1355-5111/7/i=4/a=022>.
- [DD09] M. M. Deza and E. Deza: *Encyclopdia of Distances*. Springer Berlin, 2009, URL <http://www.springer.com/us/book/9783642002342>.
- [DFE04] P. D. Drummond and Z. Ficek (Eds.): *Quantum squeezing*. Springer, 2004.
- [DHK83] R. W. P. Drever, J. L. Hall, F. V. Kowalski, J. Hough, G. M. Ford, A. J. Munley and H. Ward: *Laser phase and frequency stabilization using an optical resonator*. Applied Physics B 31 (2), S. 97–105, 1983, URL <http://dx.doi.org/10.1007/BF00702605>.
- [DMMW99] V. V. Dodonov, O. V. Man'ko, V. I. Man'ko and A. Wünsche: *Energy-sensitive and "Classical-like" Distances between Quantum States*. Physica Scripta 59 (2), S. 81, 1999, URL <http://stacks.iop.org/1402-4896/59/i=2/a=001>.
- [DMMW00] V. V. Dodonov, O. V. Man'ko, V. I. Man'ko and A. Wünsche: *Hilbert-Schmidt distance and non-classicality of states in quantum optics*. Journal of Modern Optics 47 (4), S. 633–654, 2000, URL <http://dx.doi.org/10.1080/09500340008233385>.
- [DMN95] V. V. Dodonov, V. I. Man'ko and D. E. Nikonov: *Even and odd coherent states for multimode parametric systems*. Phys. Rev. A 51, S. 3328–3336, Apr 1995, URL <https://link.aps.org/doi/10.1103/PhysRevA.51.3328>.
- [EPR35] A. Einstein, B. Podolsky and N. Rosen: *Can quantum-mechanical description of physical reality be considered complete?* Physical Review 47 (10), S. 777–780, 1935, URL <http://www.bibsonomy.org/bibtex/2ad3fca7ec0267ed78b6d30137460d696/richterek>.
- [ESB10] T. Eberle, S. Steinlechner, J. Bauchrowitz, V. Händchen, H. Vahlbruch, M. Mehmet, H. Müller-Ebhardt and R. Schnabel: *Quantum Enhancement*

- of the Zero-Area Sagnac Interferometer Topology for Gravitational Wave Detection*. Phys. Rev. Lett. 104, S. 251102, Jun 2010, URL <https://link.aps.org/doi/10.1103/PhysRevLett.104.251102>.
- [FC72] S. J. Freedman and J. F. Clauser: *Experimental Test of Local Hidden-Variable Theories*. Phys. Rev. Lett. 28, S. 938–941, Apr 1972, URL <https://link.aps.org/doi/10.1103/PhysRevLett.28.938>.
- [Fil] T. Films: *Data Sheet Mode Cleaning Mirrors*.
- [FSB98] A. Furusawa, J. L. Sørensen, S. L. Braunstein, C. A. Fuchs, H. J. Kimble and E. S. Polzik: *Unconditional Quantum Teleportation*. Science 282 (5389), S. 706–709, 1998, URL <http://science.sciencemag.org/content/282/5389/706>.
- [FT02] Z. Ficek and R. Tanaś: *Entangled states and collective nonclassical effects in two-atom systems*. Physics Reports 372 (5), S. 369 – 443, 2002, URL <http://www.sciencedirect.com/science/article/pii/S037015730200368X>.
- [Gaz09] J.-P. Gazeau: *Coherent States in Quantum Physics*. Wiley-VCH, 2009.
- [GC85] C. W. Gardiner and M. J. Collett: *Input and output in damped quantum systems: Quantum stochastic differential equations and the master equation*. Phys. Rev. A 31, S. 3761–3774, Jun 1985, URL <http://link.aps.org/doi/10.1103/PhysRevA.31.3761>.
- [GDD13] H. Grote, K. Danzmann, K. L. Dooley, R. Schnabel, J. Slutsky and H. Vahlbruch: *First Long-Term Application of Squeezed States of Light in a Gravitational-Wave Observatory*. Phys. Rev. Lett. 110, S. 181101, May 2013, URL <https://link.aps.org/doi/10.1103/PhysRevLett.110.181101>.
- [Gla63] R. J. Glauber: *Coherent and Incoherent States of the Radiation Field*. Phys. Rev. 131, S. 2766–2788, Sep 1963, URL <http://link.aps.org/doi/10.1103/PhysRev.131.2766>.
- [Göd16] M. Gödecke: *Study of resonator enhanced three wave mixing for generating visible quantum states of light, By Melanie Schünemann supervised Bachelor Thesis*. 2016.
- [GSV12] C. Gehrke, J. Sperling and W. Vogel: *Quantification of nonclassicality*. Phys. Rev. A 86, S. 052118, Nov 2012, URL <https://link.aps.org/doi/10.1103/PhysRevA.86.052118>.

- 1103/PhysRevA.86.052118.
- [GT09] O. Gühne and G. Tóth: *Entanglement detection*. Physics Reports 474 (1), S. 1 – 75, 2009, URL <http://www.sciencedirect.com/science/article/pii/S0370157309000623>.
- [GVW15] M. Giustina, M. A. M. Versteegh, S. Wengerowsky, J. Handsteiner, A. Hochrainer, K. Phelan, F. Steinlechner, J. Kofler, J.-A. Larsson, C. Abellán, W. Amaya, V. Pruneri, M. W. Mitchell, J. Beyer, T. Gerrits, A. E. Lita, L. K. Shalm, S. W. Nam, T. Scheidl, R. Ursin, B. Wittmann and A. Zeilinger: *Significant-Loophole-Free Test of Bell's Theorem with Entangled Photons*. Phys. Rev. Lett. 115, S. 250401, Dec 2015, URL <https://link.aps.org/doi/10.1103/PhysRevLett.115.250401>.
- [Hag10] B. Hage: *Purification and Distillation of Continuous Variable Entanglement, Dissertation*. 2010.
- [Hal00] M. J. W. Hall: *Quantum properties of classical Fisher information*. Phys. Rev. A 62, S. 012107, Jun 2000, URL <https://link.aps.org/doi/10.1103/PhysRevA.62.012107>.
- [HBD15] Hensen B., Bernien H., Dreau A. E., Reiserer A., Kalb N., Blok M. S., Ruitenbergh J., Vermeulen R. F. L., Schouten R. N., Abellan C., Amaya W., Pruneri V., Mitchell M. W., Markham M., Twitchen D. J., Elkouss D., Wehner S., Taminiau T. H. and Hanson R.: *Loophole-free Bell inequality violation using electron spins separated by 1.3 kilometres*. Nature 526 (7575), S. 682–686, oct 2015, URL <http://www.nature.com/nature/journal/v526/n7575/abs/nature15759.html#supplementary-information>.
- [HCC03] J. Harms, Y. Chen, S. Chelkowski, A. Franzen, H. Vahlbruch, K. Danzmann and R. Schnabel: *Squeezed-input, optical-spring, signal-recycled gravitational-wave detectors*. Phys. Rev. D68 (2003) 042001 März 2003, URL <http://arxiv.org/abs/gr-qc/0303066v2>; <http://arxiv.org/pdf/gr-qc/0303066v2>.
- [HHH96] M. Horodecki, P. Horodecki and R. Horodecki: *Separability of mixed states: necessary and sufficient conditions*. Physics Letters A 223 (1), S. 1 – 8, 1996, URL <http://www.sciencedirect.com/science/article/pii/S0375960196007062>.

- [HHHH09] R. Horodecki, P. Horodecki, M. Horodecki and K. Horodecki: *Quantum entanglement*. Rev. Mod. Phys. 81, S. 865–942, Jun 2009, URL <https://link.aps.org/doi/10.1103/RevModPhys.81.865>.
- [Hil87] M. Hillery: *Nonclassical distance in quantum optics*. Phys. Rev. A 35, S. 725–732, Jan 1987, URL <https://link.aps.org/doi/10.1103/PhysRevA.35.725>.
- [Hil89] M. Hillery: *Total noise and nonclassical states*. Phys. Rev. A 39, S. 2994–3002, Mar 1989, URL <https://link.aps.org/doi/10.1103/PhysRevA.39.2994>.
- [HUS40] K. HUSIMI: *Some Formal Properties of the Density Matrix*. Proceedings of the Physico-Mathematical Society of Japan. 3rd Series 22 (4), S. 264–314, 1940.
- [Jäg15] S. Jäger: *Konstruktion, Aufbau und Charakterisierung einer Quetschlichtquelle, By Melanie Schünemann supervised Master Thesis*. 2015.
- [Jan07] J. Janousek: *Investigation of non-classical light and its application in ultra-sensitive measurements, Dissertation*. 2007.
- [Kan65] Y. Kano: *A New PhaseSpace Distribution Function in the Statistical Theory of the Electromagnetic Field*. Journal of Mathematical Physics 6 (12), S. 1913–1915, 1965, URL <http://dx.doi.org/10.1063/1.1704739>.
- [KDM77] H. J. Kimble, M. Dagenais and L. Mandel: *Photon Antibunching in Resonance Fluorescence*. Phys. Rev. Lett. 39, S. 691–695, Sep 1977, URL <https://link.aps.org/doi/10.1103/PhysRevLett.39.691>.
- [KM76] H. J. Kimble and L. Mandel: *Theory of resonance fluorescence*. Phys. Rev. A 13, S. 2123–2144, Jun 1976, URL <https://link.aps.org/doi/10.1103/PhysRevA.13.2123>.
- [KM11] Y. A. Korennoy and V. I. Man'ko: *Optical tomography of photon-added coherent states, even and odd coherent states, and thermal states*. Phys. Rev. A 83, S. 053817, May 2011, URL <http://link.aps.org/doi/10.1103/PhysRevA.83.053817>.
- [KV10] T. Kiesel and W. Vogel: *Nonclassicality filters and quasiprobabilities*. Phys.

- Rev. A 82, S. 032107, Sep 2010, URL <https://link.aps.org/doi/10.1103/PhysRevA.82.032107>.
- [KVH09] T. Kiesel, W. Vogel, B. Hage, J. DiGuglielmo, A. Samblowski and R. Schnabel: *Experimental test of nonclassicality criteria for phase-diffused squeezed states*. Phys. Rev. A 79, S. 022122, Feb 2009, URL <https://link.aps.org/doi/10.1103/PhysRevA.79.022122>.
- [KVHS11] T. Kiesel, W. Vogel, B. Hage and R. Schnabel: *Direct Sampling of Negative Quasiprobabilities of a Squeezed State*. Phys. Rev. Lett. 107, S. 113604, Sep 2011, URL <https://link.aps.org/doi/10.1103/PhysRevLett.107.113604>.
- [Lam98] P. K. Lam: *Application of Quantum Electro-Optic Control and Squeezed Light, Dissertation*. 1998.
- [LB95] N. Lütkenhaus and S. M. Barnett: *Nonclassical effects in phase space*. Phys. Rev. A 51, S. 3340–3342, Apr 1995, URL <https://link.aps.org/doi/10.1103/PhysRevA.51.3340>.
- [Lee91] C. T. Lee: *Measure of the nonclassicality of nonclassical states*. Phys. Rev. A 44, S. R2775–R2778, Sep 1991, URL <https://link.aps.org/doi/10.1103/PhysRevA.44.R2775>.
- [Lee95] C. T. Lee: *Theorem on nonclassical states*. Phys. Rev. A 52, S. 3374–3376, Oct 1995, URL <https://link.aps.org/doi/10.1103/PhysRevA.52.3374>.
- [Leo97] U. Leonhardt: *Measuring the Quantum State of Light*. Cambridge Studies in Modern Optics, 1997.
- [LKCH00] M. Lewenstein, B. Kraus, J. I. Cirac and P. Horodecki: *Optimization of entanglement witnesses*. Phys. Rev. A 62, S. 052310, Oct 2000, URL <https://link.aps.org/doi/10.1103/PhysRevA.62.052310>.
- [LMK96] U. Leonhardt, M. Munroe, T. Kiss, T. Richter and M. Raymer: *Sampling of photon statistics and density matrix using homodyne detection*. Optics Communications 127 (1), S. 144 – 160, 1996, URL <http://www.sciencedirect.com/science/article/pii/0030401896000612>.
- [LPD95] U. Leonhardt, H. Paul and G. M. D'Ariano: *Tomographic reconstruction of the density matrix via pattern functions*. Phys. Rev. A 52, S. 4899–4907, Dec

- 1995, URL <https://link.aps.org/doi/10.1103/PhysRevA.52.4899>.
- [LS02] A. I. Lvovsky and J. H. Shapiro: *Nonclassical character of statistical mixtures of the single-photon and vacuum optical states*. Phys. Rev. A 65, S. 033830, Feb 2002, URL <https://link.aps.org/doi/10.1103/PhysRevA.65.033830>.
- [Man79] L. Mandel: *Sub-Poissonian photon statistics in resonance fluorescence*. Opt. Lett. 4 (7), S. 205–207, Jul 1979, URL <http://ol.osa.org/abstract.cfm?URI=ol-4-7-205>.
- [MBW10] A. Miranowicz, M. Bartkowiak, X. Wang, Y.-x. Liu and F. Nori: *Testing non-classicality in multimode fields: A unified derivation of classical inequalities*. Phys. Rev. A 82, S. 013824, Jul 2010, URL <https://link.aps.org/doi/10.1103/PhysRevA.82.013824>.
- [MFP08] N. C. Menicucci, S. T. Flammia and O. Pfister: *One-Way Quantum Computing in the Optical Frequency Comb*. Phys. Rev. Lett. 101, S. 130501, Sep 2008, URL <https://link.aps.org/doi/10.1103/PhysRevLett.101.130501>.
- [MKN11a] A. Mari, K. Kieling, B. M. Nielsen, E. S. Polzik and J. Eisert: *Directly Estimating Nonclassicality*. Phys. Rev. Lett. 106, S. 010403, Jan 2011, URL <https://link.aps.org/doi/10.1103/PhysRevLett.106.010403>.
- [MKN11b] A. Mari, K. Kieling, B. M. Nielsen, E. S. Polzik and J. Eisert: *Directly Estimating Nonclassicality*. Phys. Rev. Lett. 106, S. 010403, Jan 2011, URL <https://link.aps.org/doi/10.1103/PhysRevLett.106.010403>.
- [MMS02] P. Marian, T. A. Marian and H. Scutaru: *Quantifying Nonclassicality of One-Mode Gaussian States of the Radiation Field*. Phys. Rev. Lett. 88, S. 153601, Mar 2002, URL <https://link.aps.org/doi/10.1103/PhysRevLett.88.153601>.
- [NC00] M. A. Nielsen and I. L. Chuang: *Quantum Computation and Quantum Information*. Cambridge University Press, 2000, URL <http://www.bibsonomy.org/bibtex/222bf6f3de23faf420214d738924ac21b/mcclung>.
- [OHM87] Z. Y. Ou, C. K. Hong and L. Mandel: *Detection of squeezed states by cross correlation*. Phys. Rev. A 36, S. 192–196, Jul 1987, URL <https://link.aps.org/doi/10.1103/PhysRevA.36.192>.

- [PCK92] E. S. Polzik, J. Carri and H. J. Kimble: *Spectroscopy with squeezed light*. Phys. Rev. Lett. 68, S. 3020–3023, May 1992, URL <https://link.aps.org/doi/10.1103/PhysRevLett.68.3020>.
- [Per96] A. Peres: *Separability Criterion for Density Matrices*. Phys. Rev. Lett. 77, S. 1413–1415, Aug 1996, URL <https://link.aps.org/doi/10.1103/PhysRevLett.77.1413>.
- [Pou46] R. V. Pound: *Electronic Frequency Stabilization of Microwave Oscillators*. Review of Scientific Instruments 17 (11), S. 490–505, 1946, URL <http://dx.doi.org/10.1063/1.1770414>.
- [PZY07] C.-Z. Peng, J. Zhang, D. Yang, W.-B. Gao, H.-X. Ma, H. Yin, H.-P. Zeng, T. Yang, X.-B. Wang and J.-W. Pan: *Experimental Long-Distance Decoy-State Quantum Key Distribution Based on Polarization Encoding*. Phys. Rev. Lett. 98, S. 010505, Jan 2007, URL <https://link.aps.org/doi/10.1103/PhysRevLett.98.010505>.
- [RBH01] J. M. Raimond, M. Brune and S. Haroche: *Manipulating quantum entanglement with atoms and photons in a cavity*. Rev. Mod. Phys. 73, S. 565–582, Aug 2001, URL <https://link.aps.org/doi/10.1103/RevModPhys.73.565>.
- [RD88] M. D. Reid and P. D. Drummond: *Quantum Correlations of Phase in Nondegenerate Parametric Oscillation*. Phys. Rev. Lett. 60, S. 2731–2733, Jun 1988, URL <https://link.aps.org/doi/10.1103/PhysRevLett.60.2731>.
- [Rei89] M. D. Reid: *Demonstration of the Einstein-Podolsky-Rosen paradox using nondegenerate parametric amplification*. Phys. Rev. A 40, S. 913–923, Jul 1989, URL <https://link.aps.org/doi/10.1103/PhysRevA.40.913>.
- [RV33] T. Richter and W. Vogel: *Monotone funktionen, stieltjessche integrale und harmonische analyse*. Math. Ann. 108, 1933.
- [RV02] T. Richter and W. Vogel: *Nonclassicality of Quantum States: A Hierarchy of Observable Conditions*. Phys. Rev. Lett. 89, S. 283601, Dec 2002, URL <https://link.aps.org/doi/10.1103/PhysRevLett.89.283601>.
- [Sch35] E. Schrödinger: *Die gegenwärtige Situation in der Quantenmechanik*. Naturwissenschaften 23 (48), S. 807–812, 1935, URL <http://dx.doi.org/10.1007/BF01491891>.

- [Sch01] W. P. Schleich: *Quantum Optics in Phase Space*. Wiley-VCH, Berlin, 2001.
- [SHY85] R. E. Slusher, L. W. Hollberg, B. Yurke, J. C. Mertz and J. F. Valley: *Observation of Squeezed States Generated by Four-Wave Mixing in an Optical Cavity*. Phys. Rev. Lett. 55, S. 2409–2412, Nov 1985, URL <https://link.aps.org/doi/10.1103/PhysRevLett.55.2409>.
- [SJJ15] C. H. Schulte, H. Jack, A. Jones, M. Clemens, L. G. Claire and A. Mete: *Quadrature squeezed photons from a two-level system*. Nature 525 (7568), S. 222–225, sep 2015.
- [SLMS98] K. Schneider, M. Lang, J. Mlynek and S. Schiller: *Generation of strongly squeezed continuous-wave light at 1064 nm*. Opt. Express 2 (3), S. 59–64, Feb 1998, URL <http://www.opticsexpress.org/abstract.cfm?URI=oe-2-3-59>.
- [Sob14] H. Sobottka: *Tomographic reconstruction of quantum states via pattern functions*, By Melanie Schünemann supervised Master Thesis. 2014.
- [SRV05] E. Shchukin, T. Richter and W. Vogel: *Nonclassicality criteria in terms of moments*. Phys. Rev. A 71, S. 011802, Jan 2005, URL <https://link.aps.org/doi/10.1103/PhysRevA.71.011802>.
- [ST13] B. E. A. Saleh and M. C. Teich: *Fundamentals of Photonics*. Wiley-Interscience, 2013, URL <http://eu.wiley.com/WileyCDA/WileyTitle/productCd-111858581X.html>.
- [Ste08] S. Steinlechner: *Gequetschtes Licht bei 1550nm*, Diplomarbeit. 2008.
- [Sud63] E. C. G. Sudarshan: *Equivalence of Semiclassical and Quantum Mechanical Descriptions of Statistical Light Beams*. Phys. Rev. Lett. 10, S. 277–279, Apr 1963, URL <http://link.aps.org/doi/10.1103/PhysRevLett.10.277>.
- [SV05a] E. Shchukin and W. Vogel: *Inseparability Criteria for Continuous Bipartite Quantum States*. Phys. Rev. Lett. 95, S. 230502, Nov 2005, URL <https://link.aps.org/doi/10.1103/PhysRevLett.95.230502>.
- [SV05b] E. V. Shchukin and W. Vogel: *Nonclassical moments and their measurement*. Phys. Rev. A 72, S. 043808, Oct 2005, URL <https://link.aps.org/doi/10.1103/PhysRevA.72.043808>.
- [SV11a] J. Sperling and W. Vogel: *Determination of the Schmidt number*. Phys. Rev.

- A 83, S. 042315, Apr 2011, URL <https://link.aps.org/doi/10.1103/PhysRevA.83.042315>.
- [SV11b] J. Sperling and W. Vogel: *Determination of the Schmidt number*. Phys. Rev. A 83, 042315 (2011) März 2011, URL <http://arxiv.org/abs/1103.1287v1>; <http://arxiv.org/pdf/1103.1287v1>.
- [SV11c] J. Sperling and W. Vogel: *The Schmidt number as a universal entanglement measure*. Physica Scripta 83 (4), S. 045002, 2011, URL <http://stacks.iop.org/1402-4896/83/i=4/a=045002>.
- [SVA15] J. Sperling, W. Vogel and G. S. Agarwal: *Balanced homodyne detection with on-off detector systems: Observable nonclassicality criteria*. EPL (Europhysics Letters) 109 (3), S. 34001, 2015, URL <http://stacks.iop.org/0295-5075/109/i=3/a=34001>.
- [TH00] B. M. Terhal and P. Horodecki: *A Schmidt number for density matrices*. Phys. Rev. A Rapid Communications Vol.61,040301 (2000) März 2000, URL <http://arxiv.org/abs/quant-ph/9911117v4>; <http://arxiv.org/pdf/quant-ph/9911117v4>.
- [TJD13] M. A. Taylor, J. Janousek, V. Daria, J. Knittel, B. Hage, H.-A. Bachor and W. P. Bowen: *Biological measurement beyond the quantum limit*. Nat Photon 7 (3), S. 229–233, mar 2013, URL <http://www.nature.com/nphoton/journal/v7/n3/abs/nphoton.2012.346.html#supplementary-information>, 10.1038/nphoton.2012.346.
- [Uhl00] A. Uhlmann: *Fidelity and Concurrence of conjugated states*. Phys. Rev. A, 62, 032307 (2000) Juli 2000, URL <http://arxiv.org/abs/quant-ph/9909060v4>; <http://arxiv.org/pdf/quant-ph/9909060v4>.
- [UWTP16] R. Uppu, T. A. W. Wolterink, T. B. H. Tentrup and P. W. H. Pinkse: *Quantum optics of lossy asymmetric beam splitters*. Opt. Express 24 (15), S. 16440–16449, Jul 2016, URL <http://www.opticsexpress.org/abstract.cfm?URI=oe-24-15-16440>.
- [VF95] W. Vogel and R. L. d. M. Filho: *Nonlinear Jaynes-Cummings dynamics of a trapped ion*. Phys. Rev. A 52, S. 4214–4217, Nov 1995, URL <https://link.aps.org/doi/10.1103/PhysRevA.52.4214>.
- [VMDS16] H. Vahlbruch, M. Mehmet, K. Danzmann and R. Schnabel: *Detection of 15 dB*

- Squeezed States of Light and their Application for the Absolute Calibration of Photoelectric Quantum Efficiency.* Phys. Rev. Lett. 117, S. 110801, Sep 2016, URL <https://link.aps.org/doi/10.1103/PhysRevLett.117.110801>.
- [Vog91] W. Vogel: *Squeezing and anomalous moments in resonance fluorescence.* Phys. Rev. Lett. 67, S. 2450–2452, Oct 1991, URL <https://link.aps.org/doi/10.1103/PhysRevLett.67.2450>.
- [Vog95] W. Vogel: *Homodyne correlation measurements with weak local oscillators.* Phys. Rev. A 51, S. 4160–4171, May 1995, URL <https://link.aps.org/doi/10.1103/PhysRevA.51.4160>.
- [Vog00] W. Vogel: *Nonclassical States: An Observable Criterion.* Phys. Rev. Lett. 84, S. 1849–1852, Feb 2000, URL <https://link.aps.org/doi/10.1103/PhysRevLett.84.1849>.
- [Vog08] W. Vogel: *Nonclassical Correlation Properties of Radiation Fields.* Phys. Rev. Lett. 100, S. 013605, Jan 2008, URL <https://link.aps.org/doi/10.1103/PhysRevLett.100.013605>.
- [VS14] W. Vogel and J. Sperling: *Unified quantification of nonclassicality and entanglement.* Phys. Rev. A 89, S. 052302, May 2014, URL <https://link.aps.org/doi/10.1103/PhysRevA.89.052302>.
- [VW06] W. Vogel and D.-G. Welsch: *Quantum Optics.* Wiley-VCH Verlag GmbH & Co. KGaA, 2006, URL <http://dx.doi.org/10.1002/3527608524>.
- [Wer89] R. F. Werner: *Quantum states with Einstein-Podolsky-Rosen correlations admitting a hidden-variable model.* Phys. Rev. A 40, S. 4277–4281, Oct 1989, URL <https://link.aps.org/doi/10.1103/PhysRevA.40.4277>.
- [Whi97] A. White: *Classical and quantum dynamics of optical frequency conversion, Dissertation.* 1997.
- [Wig32] E. Wigner: *On the Quantum Correction For Thermodynamic Equilibrium.* Phys. Rev. 40, S. 749–759, Jun 1932, URL <https://link.aps.org/doi/10.1103/PhysRev.40.749>.
- [Win98] M. C. I. W. M. L. D. K. B. E. . M. D. M. Wineland, D. J.: *Experimental Issues in Coherent Quantum-State Manipulation of Trapped Atomic Ions.* Journal of Research of the National Institute of Standards and Technology 103(3), S.

- 259–328, 1998, URL <http://www.nist.gov/jres>.
- [WM08] D. F. Walls and G. J. Milburn: *Quantum Optics*. Springer, 2008, URL <http://www.springer.com/us/book/9783540285731>.
- [WUG98] B. Willke, N. Uehara, E. K. Gustafson, R. L. Byer, P. J. King, S. U. Seel and R. L. Savage: *Spatial and temporal filtering of a 10-W Nd:YAG laser with a Fabry–Perot ring-cavity premode cleaner*. Opt. Lett. 23 (21), S. 1704–1706, Nov 1998, URL <http://ol.osa.org/abstract.cfm?URI=ol-23-21-1704>.
- [WXK87] L.-A. Wu, M. Xiao and H. J. Kimble: *Squeezed states of light from an optical parametric oscillator*. J. Opt. Soc. Am. B 4 (10), S. 1465–1475, Oct 1987, URL <http://josab.osa.org/abstract.cfm?URI=josab-4-10-1465>.
- [Yos08] K. Yosida: *Functional Analysis*. Springer Berlin Heidelberg, 2008, URL <http://www.springer.com/de/book/9783540586548>.
- [ZPB07] A. Zavatta, V. Parigi and M. Bellini: *Experimental nonclassicality of single-photon-added thermal light states*. Phys. Rev. A 75, S. 052106, May 2007, URL <https://link.aps.org/doi/10.1103/PhysRevA.75.052106>.



# List of Publications

- [1] E. Agudelo, J. Sperling, W. Vogel, S. Köhnke, M. Mraz, and B. Hage. Continuous sampling of the squeezed state nonclassicality. *Phys. Rev. A* 92, 033837 (2015), June 2015.
- [2] Sergej Ryl, Jan Sperling, Elizabeth Agudelo, Melanie Mraz, Semjon Köhnke, Boris Hage, and Werner Vogel. Unified nonclassicality criteria. *Phys. Rev. A* 92, 011801 (2015), July 2015.
- [3] B. Kühn, W. Vogel, M. Mraz, S. Köhnke, and B. Hage. Anomalous quantum correlations of squeezed light. *Phys. Rev. Lett.*, 118:153601, Apr 2017.
- [4] Melanie Mraz, Jan Sperling, Werner Vogel and Boris Hage. Witnessing the degree of nonclassicality of light. *Phys. Rev. A* 90, 033812 (2014), November 2014.